Bioactive Materials 12 (2022) 214–245

Contents lists available at ScienceDirect

Bioactive Materials

journal homepage: www.keaipublishing.com/en/journals/bioactive-materials

Recent advances in engineering iron oxide nanoparticles for effective magnetic resonance imaging

Zhenghuan Zhao [a,b,*], Muyao Li [a], Jie Zeng [a], Linlin Huo [a], Kun Liu [b], Ruixue Wei [c], Kaiyuan Ni [d], Jinhao Gao [b,**]

[a] College of Basic Medical Sciences, Chongqing Medical University, Chongqing, 400016, China
[b] State Key Laboratory of Physical Chemistry of Solid Surfaces, The Key Laboratory for Chemical Biology of Fujian Province, And Department of Chemical Biology College of Chemistry and Chemical Engineering Xiamen University, Xiamen, Fujian, 361005, China
[c] Department of Cerebrovascular Diseases, The Second Affiliated Hospital of Zhengzhou University, Zhengzhou, Henan, 450052, China
[d] Koch Institute for Integrative Cancer Research, Massachusetts Institute of Technology, Cambridge, MA, 02142, United States

ARTICLE INFO

Keywords:
Iron oxide nanoparticles
Improved relaxation
Dual-modal contrast imaging
Environment responsive imaging
Strcture engineering

ABSTRACT

Iron oxide nanoparticle (IONP) with unique magnetic property and high biocompatibility have been widely used as magnetic resonance imaging (MRI) contrast agent (CA) for long time. However, a review which comprehensively summarizes the recent development of IONP as traditional T_2 CA and its new application for different modality of MRI, such as T_1 imaging, simultaneous T_2/T_1 or MRI/other imaging modality, and as environment responsive CA is rare. This review starts with an investigation of direction on the development of high-performance MRI CA in both T_2 and T_1 modal based on quantum mechanical outer sphere and Solomon–Bloembergen–Morgan (SBM) theory. Recent rational attempts to increase the MRI contrast of IONP by adjusting the key parameters, including magnetization, size, effective radius, inhomogeneity of surrounding generated magnetic field, crystal phase, coordination number of water, electronic relaxation time, and surface modification are summarized. Besides the strategies to improve r_2 or r_1 values, strategies to increase the *in vivo* contrast efficiency of IONP have been reviewed from three different aspects, those are introducing second imaging modality to increase the imaging accuracy, endowing IONP with environment response capacity to elevate the signal difference between lesion and normal tissue, and optimizing the interface structure to improve the accumulation amount of IONP in lesion. This detailed review provides a deep understanding of recent researches on the development of high-performance IONP based MRI CAs. It is hoped to trigger deep thinking for design of next generation MRI CAs for early and accurate diagnosis.

1. Introduction

Various biomedical nanomaterials have been developed to act as agents to fulfill cell labeling [1–5] and separation [6–9], biological sensing [10–14], and disease diagnosis/therapy [15–18]. Among all biomedical nanomaterials, iron oxide nanoparticle (IONP) has been intensively investigated due to their unique magnetic property and high biocompatibility [19–23]. IONP based commercial MRI contrast agent (CA) (e.g. Resovist, Feridex), which shorten the transverse relaxation (T_2) of proton, have been approved by the U.S. Food and Drug Administration (FDA) for clinical diagnosis. However, commercial available IONP based MRI CA show low MRI contrast ability due to low crystallinity or poor surface modification, which lead to reduced sensitivity and accuracy in MRI contrast imaging and limited application in early and accurate diagnosis [24–26]. Over the past years, tremendous efforts have been made to improve the relaxivity of IONP by engineering crystal and surface structure [27–29]. On the basis of relaxivity-structure assessment, IONP with high T_2 relaxivity were discovered to show several critical characteristics, including high saturated magnetization, large effective size, high inhomogeneous magnetic field, and suitable surface modification [30–32]. According to the classical outer-sphere theory, saturated magnetization and large effective size are

Peer review under responsibility of KeAi Communications Co., Ltd.
* Corresponding author. College of Basic Medical Sciences, Chongqing Medical University, Chongqing, 400016, China.
** Corresponding author.
E-mail addresses: roddirck@cqmu.edu.cn (Z. Zhao), jhgao@xmu.edu.cn (J. Gao).

https://doi.org/10.1016/j.bioactmat.2021.10.014
Received 18 June 2021; Received in revised form 27 September 2021; Accepted 10 October 2021
Available online 19 October 2021

responsible for the field perturbation area for the outersphere protons and proportional to the T_2 relaxivity of MRI CA [33–35]. Thus, synthesis of IONP with high saturated magnetization and large size have firstly been investigated to increase the T_2 relaxivity of IONP. Additionally, high inhomogeneous magnetic field was founded to accelerate the dephasing process of protons around IONP, which significantly increased its T_2 relaxivity. With the development of nanoparticle synthesis, IONP with unique morphology has been developed through morphology controllable synthesis [36–38]. These IONP show large effective size and high inhomogeneous of surrounding magnetic field, causing the elevation of T_2 relaxivity. In addition, surface coating layer was discovered to affect the magnetic property of IONP and diffusion of surrounding proton [39–41]. Therefore, optimizing surface ligand of IONP have been conducted to form proper surface coating layer and increase T_2 relaxivity of IONP.

IONP based traditional T_2 CAs exert darken contrast in the region where they reside, which may result in false positive detection caused by the confusion between lesion and bleeding, calcification, or metal deposition. This limitation encourages researchers to develop IONP based longitudinal relaxation (T_1) CA, which exerts bright contrast to distinguish tissue [42–44]. However, traditional IONP exhibits high r_2/r_1 ratio, hindering its application as a T_1 CA. Based on the Solomon-Bloembergen-Morgan (SBM) theory, T_1 contrast ability is highly depend on the chemical exchange efficiency between magnetic ions and protons. Currently, three key parameters have been unearthed to alter the chemical exchange efficiency and determine T_1 contrast capacity of IONP. First, high saturated magnetization causes high r_2/r_1 ratio and impairs T_1 contrast imaging. Decreasing the size and crystallinity have been proven to successfully reduce saturated magnetization and r_2/r_1 ratio of IONP [45–47]. Second, coordination number of water (q) on the surface of IONP is another important parameter to tune. Since coordination number of iron ion is constant, the method to optimize the q is directly increasing the number of iron ions on the surface or introducing other magnetic ions with large amounts of unpaired electrons. Thanks to the controllable synthesis and development of new generation of surface ligands, various IONP with high surface-to-volume ratio, specific composition, and optimal surface coating have been developed to show high T_1 contrast and exhibit potential to achieve accurate tumor contrast imaging [48–50]. Recently, an undesirable structure, that is the presence of undesirable Fe (II) ion on the surface of IONP, have been noticed. Due to its short electron relaxation time (τ_s), Fe (II) ion is unfavorable to achieve efficient relaxation enhancement and severely reduces the T_1 contrast. Strategy to replace the Fe (II) on IONP surface with other magnetic ions with long τ_s have been proved to significantly increase T_1 contrast for high-performance T_1 contrast imaging [51].

Apart from fabricating IONP with high T_2 or T_1 contrast ability, high-performance IONP based MRI CA could also be fulfilled by increasing its contrast efficiency. Compared to the IONP in the form of single T_2 negative or T_1 positive, introducing T_1 moiety or other imaging contrast moiety into IONP could yield complementary diagnostic information to increase the contrast efficiency [52–54]. Recently, integration of IONP and gadolinium species have been developed as dual-modal CA (DMCA). A facile strategy is coating IONP with gadolinium based nanostructure or gadolinium complex [55–57]. However, the spin alignment on T_1 contrast shell is opposite to the local magnetic field generated by IONP core, which reduces its T_1 contrast and limits its application in accurate T_1/T_2 dual modal contrast imaging. Interestingly, this phenomenon is highly dependent on the distance between IONP and T_1 contrast moiety [58,59]. Introducing SiO_2 isolating layer to separate T_1 domain and IONP or forming Janus structure have been applied to increase the distance between IONP and T_1 moiety to develop high-performance IONP based T_1/T_2 DMCA [60]. Lately, doping manganese or gadolinium ions into IONP have been found to be another effective method to increase T_1 contrast of DMCA [61–63]. Apart from development of IONP with dual-modal MRI contrast, direct conjugation of secondary even tertiary imaging moiety with IONP is another effective method to improve its contrast efficiency. The main strategy to fabricate IONP based multi-modal imaging CA is surface conjugating IONP with secondary imaging components, such as single-photon emission computed tomography (SPECT) [64,65], positron emission tomography (PET) [66–68], computed tomography (CT) [69–71], fluorescence (FL) imaging [72–74], ultrasound (US) imaging [75–77], and photoacoustic (PA) imaging [78–81]. Based on the complementary signals, the regions of interest, including tumor, cardiovascular disease, and cell tracking could be rapidly and accurately detected.

For disease diagnosis, the contrast efficiency of MRI CA depends on the signal difference between lesion and adjacent healthy tissue. Therefore, there is a growth of interest on developing internal (lesion microenvironment) and external (specific physical condition) responsive MRI CAs [82–87]. Environment responsive MRI CA could respond to specific characters and exhibit triggered or switchable signals for highly specific and precise MRI images [88–94]. IONP based responsive MRI CA could be divided into three different manners, active, recovery, and switchable. Compared to the traditional MRI CA with fixed contrast capacity, IONP based responsive MRI CA with signal active or recovery capacity could enhance T_1 or T_2 signal in response to a specific stimulus of lesion. Recently, IONP based environment responsive MRI CA with modal switchable capacity have been developed to further increase the signal difference between lesion and normal tissue. Similar to the traditional MRI contrast imaging, there are two modals of switchable tumor microenvironment (TEM)-responsive MRI contrast imaging: T_2 contrast switch to T_1 contrast (mode I) and T_1 contrast switch to T_2 contrast (mode II). The strategy to develop modal switchable MRI CA is based on the fact that formation of magnetic nanocluster or nanoaggregation could improve T_2 relaxivity of ultrasmall IONP. Normally, ultrasmall IONP are considered as typical T_1 CA when it is monodisperse. With the specific surface modification, ultrasmall IONP could achieve the status change between cluster and monodisperse. These structural changes result in the decrease or increase of T_2/T_1 contrast, which endow CA to achieve modal switchable contrast imaging.

The signal difference between normal tissue and lesion is also directly influenced by the amount of IONP in lesion, which is mainly determined by its *in vivo* behavior. When IONP enter the physiological environment, serum proteins rapidly adsorb on its surface and form protein corona, resulting in the decrease of blood circulation time and accumulation in lesion [95–98]. IONP Surface modification of nanoparticles with specific ligands, such as polyethylene glycol (PEG) or zwitterionic small molecules, can effectively reduce the non-specific protein adsorption and elevate the accumulation amount of IONP in lesion [99–106]. In addition, the accumulation amount of IONP in lesion could be further increased by introducing targeting motif,e.g. antibodies, proteins, peptides, and aptamers to achieve targeted MR contrast imaging with enhanced contrast efficiency [27,107–111].

During the past decades, a number of reviews have been published to summarize the development of IONP as MRI CA. Yet a review comprehensively discussing high-performance IONP based MRI CAs with high T_2 relaxivity, high T_1 relaxivity, environment responsive contrast ability, multi-modal contrast capacity, and optimized *in vivo* behavior in recent progress is needed. This review discuss the parameters to affect IONP based MRI CA from contrast ability of IONP and contrast efficiency of IONP *in vivo* (Fig. 1). Detailed mechanism on development of IONP based MRI CA with high T_2 or T_1 relaxivity was firstly discussed according to classical quantum mechanical outer sphere and SBM theory. More importantly, some instances to increase r_2 and r_1 values of IONP through adjusting the theoretical related key parameters, including magnetization, size, effective radius, and inhomogeneity of surrounding generated magnetic field, crystal phase, coordination number of water, electronic relaxation time, and surface modification are presented to point out the direction of development of IONP with high contrast ability. After detailed discussion on contrast improvement, representative rational designs and advances of IONP to improve its contrast efficiency are reviewed. The enhancement of contrast efficiency could be

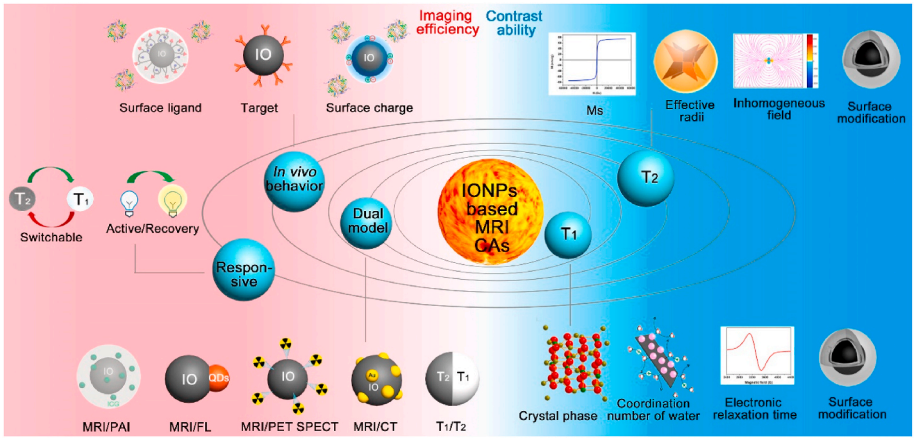

Fig. 1. Schematic diagram of key parameters for the design of high-performance IONP based MRI CA. T_2 and T_1 relaxivity of IONP directly determine the contrast ability of IONP. Theoretically, contrast ability of IONP could be altered by magnetization, size, effective radii, inhomogeneity of surrounding generated magnetic field, crystal phase, coordination number of water, electronic relaxation time, and surface modification. Additionally, improving *in vivo* contrast efficiency of IONP through introducing second imaging modal, endowing IONP with environment response capacity, and optimizing the *in vivo* behavior is another strategy to construct high-performance IONP based MRI CA.

fulfilled by introducing other imaging modals, endowing IONP with environment response capacity, and designing the surface ligand to optimize *in vivo* behavior. We hope this detailed review could build a bridge between the proof–of-concept to translate high-performance MRI CAs, further promoting rational design of magnetic nanoparticles for early and accurate lesion detection.

2. Key parameters enhancing T_2 relaxivities of IONPs

Based on its specific magnetic property, especially high saturated (M_s) value, IONP could accelerate the transverse relaxation of proton in surrounding tissue and decrease signal intensity in T_2-weighted MRI images. Thus, IONP has been used as T_2 CA for the past decades. Several commercial IONP based T_2 CAs have been approved by FDA in clinical application. However, some defects, such as low crystalline and poor surface modification, result in the low contrast and reduce the quality of MRI contrast images. Over the past decades, many attempts and theoretical investigations have been conducted to improve the T_2 contrast of IONP.

2.1. Outer-sphere theory

Theoretically, T_2 relaxation of proton could be interpreted by three mechanisms, dipole-dipole coupling [112], curie spin relaxation [113,114], and scalar or contact relaxation [115,116]. An accelerated relaxation phenomenon is observed in the existence of magnetized particles with weak magnetization [117], while the relaxation enhancement is limited. With the development of nanotechnology, IONP have been discovered to enhance the T_2 relaxation of proton [25,118–121]. With high magnetic moment, IONP could generate a local magnetic field under the external magnetic field which can effectively shorten the relaxation of surrounding proton [122]. According to the outer sphere theory, the proton dephasing process can be divided into three stages, motional average regime (MAR), static dephasing regime (SDR), and echo-limiting regime (ELR) based on the value of τ_D [118,123]. τ_D is the diffusion time and could be calculated by the following equation: $\tau_D = d^2/4D$, where d is efficient radius of particle and D is the water diffusion coefficient. MAR condition is fulfilled when $\tau_D < 1/(\gamma B_{eq})$, where γ is the proton gyromagnetic ratio and B_{eq} is the equatorial magnetic field. On the basis of that protons rapidly diffuse around IONP, protons experience quick magnetic field changing in MAR [124], which is effectively time-averaged. According to the quantum-mechanical outer-sphere theory, T_2 relaxaivity of IONP is given by

$$1/T_2 = r_2 = \left(256\pi^2\gamma^2/405\right)V^* M_s^2 r^2/D(1 + L/a) \quad (1)$$

Where M_s, L, and r are the saturation magnetization, thickness of an impermeable surface coating, and efficient radius of magnetic nanostructure. These key parameters are determined by the crystal and surface structure of IONP. Based on this equation, T_2 contrast of IONP are proportional to M_s and r. Thus, one can develop IONP with high T_2 contrast ability by adjusting these key parameters. T_2 contrast of IONP can not uncontrolled increase with the increase of particles size. When the size of particle or cluster reaches a certain limit, the T_2 contrast IONP reaches the maximum value and fulfill the SDR [118,125]. In SDR, the T_2 relaxivity of IONP are given by

$$r^2 = \frac{8\pi^2\sqrt{3}}{81}\frac{A^3 N_0}{10^6 Z}\gamma M_s \quad (2)$$

where A is the lattice parameter, N_0 is the Avogadro constant, Z is number of formula units per unit cell, γ is the proton gyromagnetic ratio. Based on this equation, the r_2 value of IONP in SDR is highly dependent on its saturated magnetization. Therefore, one can further increase the T_2 contrast ability of IONP in SDR through elevating the saturated magnetization.

Along with the further increase of size, T_2 relaxivity of IONP reach to ELR [126]. In this regime, proton shows limited diffusion in a time interval. This undesired property leads to T_2 contrast reduction with their sizes increase, meaning that construction of high-performance T_2 MRI CAs cannot be achieved by endless increasing the radius of IONP.

2.2. Magnetic behavior

Based on the quantum-mechanical outer-sphere theory, improvement of M_s can significantly elevate the T_2 contrast of IONP. Since magnetic properties of magnetic materials are highly dependent on their crystal structure, such as crystallinity, crystal composition, and crystal size, engineering the structure of IONP is an effective method to ameliorate magnetic behavior and T_2 MRI contrast. In the following sections, we will discuss the strategies to optimize crystal structure of IONP to improve M_s value for enhanced T_2 contrast.

2.2.1. Crystallinity

The simplest attempt to improve magnetic moment of IONP is improving crystallinity. Structure order, determined by the crystallinity, affects the state of magnetic spin in IONP and determines its magnetic property. IONP could be mainly divided into three phases, those are magnetite, Wüstite, and Maghemite phase. Due to the growth kinetics of Wüstite phase, IONP exhibits typical mixed crystal phase and result in low crystallinity [36,127]. The existing undesired mixed phase in IONP would destroy the long-range-order of magnetic spin and reduce magnetic moment. With the development of nanosynthsis, IONP with high crystallinity could be obtained by tunning the synthesis parameter. For example, Hyeon and colleagues reported that synthesis of IONP *via* thermal decomposition of precursors in high boiling points solvent

provided IONP with high crystallinity and magnetic moment [128,129], paving the way to fabricate high-performance T_2 MRI CA. In addition, IONP with high crystallinity could be obtained by other methods, such as polyol and microwave synthesis. Hachani et al. adapted polyol synthesis to get IONP at high temperature and pressure conditions. The as-prepared IONP show high crystallinity and M_s, resulting in high T_2 relaxivity [130].

2.2.2. Crystal composition

As an effective method, doping have been widely used to engineer the crystal composition of nanomaterial, which determines the magnetic property of magnetic material [131–133]. Magnetite phase show spinel or inverse spinel structure, which corresponds to the oxygen-packed face-centered cubic lattices with octahedral (O_h) and tetrahedral (T_d) site, respectively. Typically, Fe^{3+} ions occupies the O_h and T_d site, while Fe^{2+} occupies the O_h site. Under an external magnetic field, the magnetic spin in O_h site is aligned in parallel to the external magnetic field, while the magnetic spin in T_d site alignes antiparallel to the external magnetic field. Therefore, increasing the magnetic spin in O_h site or reducing the magnetic spin in T_d site theoretically increases the magnetization of IONP. Cheon and co-author engineered the structure of Fe_3O_4 nanocrystal by introducing different divalent magnetic ions with different magnetic spin magnitudes, including Mn^{2+} (5 μ_b), Fe^{2+} (4 μ_b), Co^{2+} (3 μ_b), and Ni^{2+} (2 μ_b), to investigate the effect of dopant on its magnetic property and T_2 contrast (Fig. 2a and b) [27]. Interestingly, the magnetization and T_2 contrast gradually decreases with the order of Mn^{2+}, Fe^{2+}, Co^{2+}, and Ni^{2+}, which is highly consistent with the change of magnetic spin magnitude. It should note that Mn^{2+} doped Fe_3O_4 ($Mn_xFe_{3-x}O_4$) exhibits the highest saturation magnetization (110 emu/g = 110 A·m^2/kg) and T_2 relaxivity (358 mM^{-1}s^{-1} at 1.5 T). $Mn_xFe_{3-x}O_4$ NP shows mixed spinel structure with Mn^{2+} occupied either T_d or O_h site. The rise of Mn^{2+} doping level may lead to two opposite effects: one is increasing magnetic spin in Fe_3O_4 nanocrystal and elevating the magnetic moment, the other one is disturbing the long-range order of magnetic spins and resulting in the decrease of magnetic moment. Recent research indicates that the saturation magnetization and T_2 contrast of $Mn_xFe_{3-x}O_4$ nanocrystal gradually increases with the Mn^{2+} doping level rising from x = 0 to 0.43, while decreases with the doping level further rise to x = 1.06 [134]. When x = 0.43, $Mn_xFe_{3-x}O_4$ nanocrystal shows highest saturation magnetization (89.5 emu/g = 89.5 A·m^2/kg) and T_2 relaxivity (904.4 ± 11.1 mM^{-1}s^{-1} at 7 T). Apart from the magnetic ions, dopant non-magnetic ions into Fe_3O_4 nanocrystal have been proved to be an effective method to increase its magnetization and MRI contrast ability. Jang et al., constructed Zn^{2+} doped Fe_3O_4 nanocrystal [$(Zn_xFe_{1-x})Fe_2O_4$] with spinel structure (Fig. 2c–e) [135]. Extended X-ray absorption fine structure analysis indicates that Zn^{2+} mainly occupies the T_d sites, which could effectively reduce the antiferromagnetic coupling interactions between T_d and O_h sites and increase the magnetic moment. The magnetic property investigation reveals that the saturation magnetization could be enhanced to 161 emu/g (161 A·m^2/kg) when x = 0.4. This high saturation magnetization generate superior T_2 contrast with the r_2 value of 687 mM^{-1}s^{-1} at 4.5 T, which is approximately 2.5 and 1.6 times higher than that of Fe_3O_4 (276 mM^{-1}s^{-1}) and $MnFe_2O_4$ (422 mM^{-1}s^{-1}) nanocrystal.

2.2.3. Core-shell structure

Compared to the IONP, metallic iron nanoparticle exhibit significantly higher saturation magnetization at room temperature. Introducing metallic iron moiety into IONP could effectively increase its saturated magnetization and T_2 contrast [136–138]. To improve magnetic moment of IONP, Tilley and co-authors synthesized high crystalline iron/iron oxide core/shell nanocrystal by naturally oxidation iron

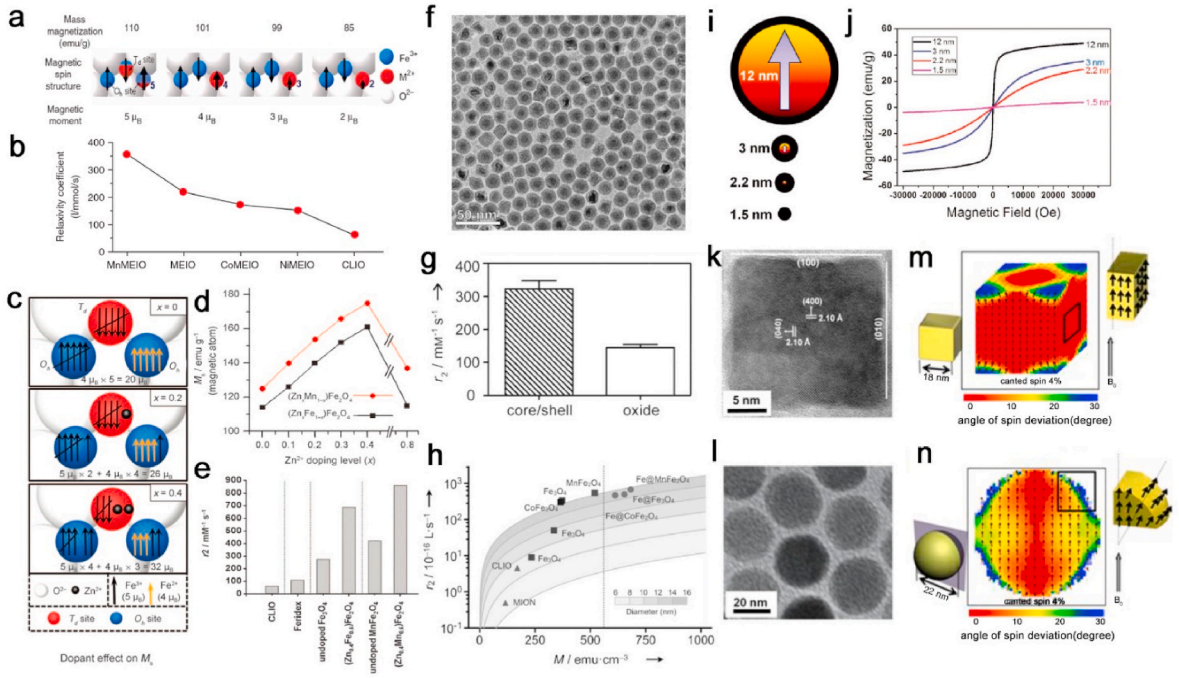

Fig. 2. Magnetic behavior effect on T_2 relaxivity of IONP. (a) Mass magnetization values and schematics of spin alignments and (b) T_2 relaxivities of $MnFe_2O_4$ (MnMEIO), Fe_3O_4 (MEIO), $CoFe_2O_4$ (CoMEIO) and $NiFe_2O_4$ (NiMEIO). Reproduced with permission [27]. Copyright 2007, Nature Publishing Group. (c) Magnetic spin alignment diagram of $(Zn_xFe_{1-x})Fe_2O_4$ nanoparticles with x = 0, 0.2, and 0.4 under applied magnetic field. (d) M_s and (e) r_2 values of $(Zn_xMn_{1-x})Fe_2O_4$ and $(Zn_xFe_{1-x})Fe_2O_4$ nanoparticles with different Zn doping level. Reproduced with permission [135]. Copyright 2009, John Wiley & Sons, Inc. (f) TEM image and (g) r_2 value of iron/iron oxide core/shell nanoparticle. Reproduced with permission [139]. Copyright 2011, John Wiley & Sons, Inc. (h) r_2 values of iron nanoparticle coated by various magnetic shell at the fixed larmor frequency. Reproduced with permission [141]. Copyright 2011, John Wiley & Sons, Inc. (i) Diagram of spin canting effect in various sized IONPs. (j) M − H curve of IONPs with sizes of 1.5, 2.2, and 3 nm at 300 K. Reproduced with permission [46]. Copyright 2011, American Chemical Society. (k–l) TEM images of cube and sphere nanoparticles. (m–n) Simulated magnetic spin state of cube and sphere, indicating the degree of spin canting against external magnetic field. Reproduced with permission [149]. Copyright 2012, American Chemical Society.

nanoparticle (Fig. 2f and g) [139]. Introducing iron core endows this core/shell nanostructure with high magnetization with the value of 150 emu/g (150 A·m^2/kg) (Fe), which is significantly higher than that of normal Fe_3O_4 nanocrystal. This far elevation of magnetization results in the obviously rising of T_2 relaxivity from 145 mM^{-1}s^{-1} to 324 mM^{-1}s^{-1} at 9.4 T. It should note that the crystallinity of core/shell nanostructure is an important parameter to its T_2 relaxivity [140]. The amor-Fe/Fe_3O_4 exhibits remarkably lower T_2 relaxivity (67 mM^{-1}s^{-1}) than bcc-Fe/-Fe_3O_4 (220 mM^{-1}s^{-1}) with high crystallinity, even much lower than Ferridex (110 mM^{-1}s^{-1}). The crystal structure of iron oxide shell is another parameter to affect its magnetization and T_2 relaxivity. Yoon et al. coated monometallic iron with $MnFe_2O_4$, Fe_3O_4, $CoFe_2O_4$, and FeO (Fig. 2h) [141]. These iron/iron oxide core/shell nanostructures exhibite increased magnetization and T_2 relaxivity with shell structures altered from FeO to $CoFe_2O_4$, Fe_3O_4, and $MnFe_2O_4$, consistent with the magnetization change of the shell structure. These results mean that coating monometallic iron with a magnetic shell with high magnetization could further improve its magnetization and T_2 relaxivity.

2.2.4. Disordered spin

Previous researches indicate that IONP could be considered as a core/shell structure with the magnetic core and magnetically dead layer, where the magnetic spin is lack of full alignment. In the magnetically dead layer, the spin canting and other effects destroy the long-range-order of magnetic spins and result in the disorder of magnetic dipoles, which lead to the decrease of magnetic moment [142–147]. The thickness of spin-canting layer has been determined as about 0.9 nm. Thus, along with the increase of size, the ratio of spin-canting layer to whole magnetic nanoparticle decreases (Fig. 2i and j). It has been reported that the magnetization moment and r_2 value of IONP increases with the decrease of magnetically dead layer ratio. This phenomenon has been found in $Mn_xFe_{3-x}O_4$ nanoparticle as well, which implies that one can develop IONP with high T_2 relaxivity through decreasing the magnetic dead layer ratio [132]. However, recent researches indicate that this elevation effect is connected to the size of IONP. Rinaldi and co-author synthesized IONP at the present of molecular oxygen to increase the magnetic diameter [148]. Interestingly, increasing the magnetic diameter for the IONP with physical diameter of 21 nm leads to slight improvement in the T_2 relaxivity. This result could be attributed to relatively low ratio of magnetically dead layer in IONP with large physical size, limiting the improvement on T_2 relaxivity by further decreasing the magnetically dead layer.

Morphology as a key factor to determine the surface structure of nanomaterials, has been proven to affect the canting spins on the surface of IONP as well. Cheon and co-authors compared the saturated magnetization of cubic and spherical $(Zn_xFe_{1-x})Fe_2O_4$ nanoparticle with the same magnetic volume (Fig. 2k-n) [149]. The orientations of the overall magnetic spin structure shows that the disordered spins are homogeneously distributed on the surface of spherical IONP with certain thickness. While, the disordered spins are mainly distributed at the corner of the cubic IONP. Compared to the spherical IONP without a certain exposed facet, cubic IONP shows the single crystal facet. This unique feature results in the similar spin state in the core and surface, which reduce surface anisotropy. The calculated disordered spins of cube are about 4%, which is significantly lower than that of sphere with the value of 8%. Therefore, the saturated magnetization of cube (165 emu/g = 165 A·m^2/kg) is remarkably higher than that of sphere (145 emu/g = 145 A·m^2/kg).

2.3. Effective radius

Apart from M_s, size also determines the region, in which proton relaxation could be accelerated by IONP. Normally, the region could be simulated to a sphere covering the full IONP. The diameter of this region could be defined as the effective radius. Effective radii determined by the size is responsible for the field perturbation area for the outersphere protons and proportional to the T_2 relaxivity in MAR, which means improvement of T_2 relaxivity of IONP could be achieved by increasing the effective radius with maintained saturated magnetization. However, T_2 contrast of IONP are not uncontrolled increase with the increase of efficient radius. When the efficient radius of particle or cluster reach to a certain limit, the T_2 contrast of IONP reach to its maximum value and fulfill the SDR. In this section, we will focus on the strategy to develop high-performance T_2 CA by increasing effective radius of IONP through controllable synthesis.

2.3.1. Individual IONP

In MAR T_2 relaxivity of IONP is proportional to the square of effective radius according to outer sphere theory [124]. For spherical IONP, its effective radius is directly determined by its diameter, thus, increasing its diameter have been proven to be the simplest method to improve its T_2 relaxivity. Cheon and co-authors find that IONP shows a typical diameter-dependent T_2 relaxivity, that is, r_2 value increase with the rising of diameter [150]. This diameter-dependent T_2 relaxivity has been observed in other researches, which is highly consistent with the theoretical analysis [33,151–153]. Besides, sophisticated morphology of magnetic nanostructure can increase the effective radii of particle cores and improve intensity, direction, and gradient of the magnetic stray field, accelerating surrounding proton diffusion and dephasing. Zhao et al. developed a novel IONP with octapod morphology with the assistance of chloride ion (Fig. 3a–e) [154]. Due to its unique morphology, the calculated effective radius of IONP with octapod morphology is about 2.4 times higher than that of spherical IONP with the same solid volume and similar magnetization. Further MRI investigation indicates that the octapod IONP with edge length of 30 nm show an ultrahigh T_2 relaxivity with the value of 679.3 ± 30 mM^{-1} s^{-1} at 7 T, which is about 5.4 times larger than that of spherical IONP with the same geometric volume. Inspired by this research, a large number of IONPs with anisotropic morphologies and improved effective radii, such as plate [155,156], cube [157,158], and tripod [159], have been reported to show enhanced T_2 relaxivity. Recently, Yang et al., systematically investigate the morphology effect on the effective radius and T_2 relaxivity of IONP (Fig. 3f) [160]. They synthesized $Mn_xFe_{3-x}O_4$ nanoparticles with the morphology of sphere, cube, plate, tetrahedron, rhombohedra, and octapod with the same solid volume and similar magnetization. The calculated effective radius shows a gradually decrease with the order of octapod, rhombohedra, tetrahedron, plate, cube, and sphere. The MRI analyses indicate that the T_2 relaxivities of all samples show descending tendency from octapod to sphere, which is the same to the tendency change of effective radius. The increased T_2 relaxivity along with the rising of effective radius demonstrate that effective radius can eventually determine T_2 relaxivity in MAR.

In contrast to the MAR, the large magnetic nanoparticles generate strong dipolar field around it in SDR, which significantly reduce the influence of proton diffusion on signal decay. Thus, the T_2 relaxivity of IONP can not increase with the rise of particle size and reach to a plateau [123,124]. Recently, Hyeon and co-workers investigate the T_2 relaxivity of cubic IONP with the size of 22, 28, 32, 42, and 49 nm (Fig. 3g and h) [158]. Due to the proper hydrodynamic diameter, cubic IONP with the size of 22 and 28 nm are in the SDR and show extremely high T_2 contrast with the similar r_2 values of approximately 800 mM^{-1}s^{-1}. While, cubic IONP show reduced r_2 value when the size exceed 30 nm. These observations could be attributed to the large size of cubic IONP lead to them out of SDR and reach ELR. These results are highly consistent to the theoretical studies and point out that accurately controlling the particle size of IONP in SDR could obtain high-performance T_2 MRI CA.

2.3.2. Assembled IONP

Clustering of IONP is another effective method to increase their effective radius with increased T_2 relaxivity [126,161–163]. To generate assembled IONP, polymers have been chosen as candidates due to the finely controlled size and colloidal stability. Ai et al. encapsulate

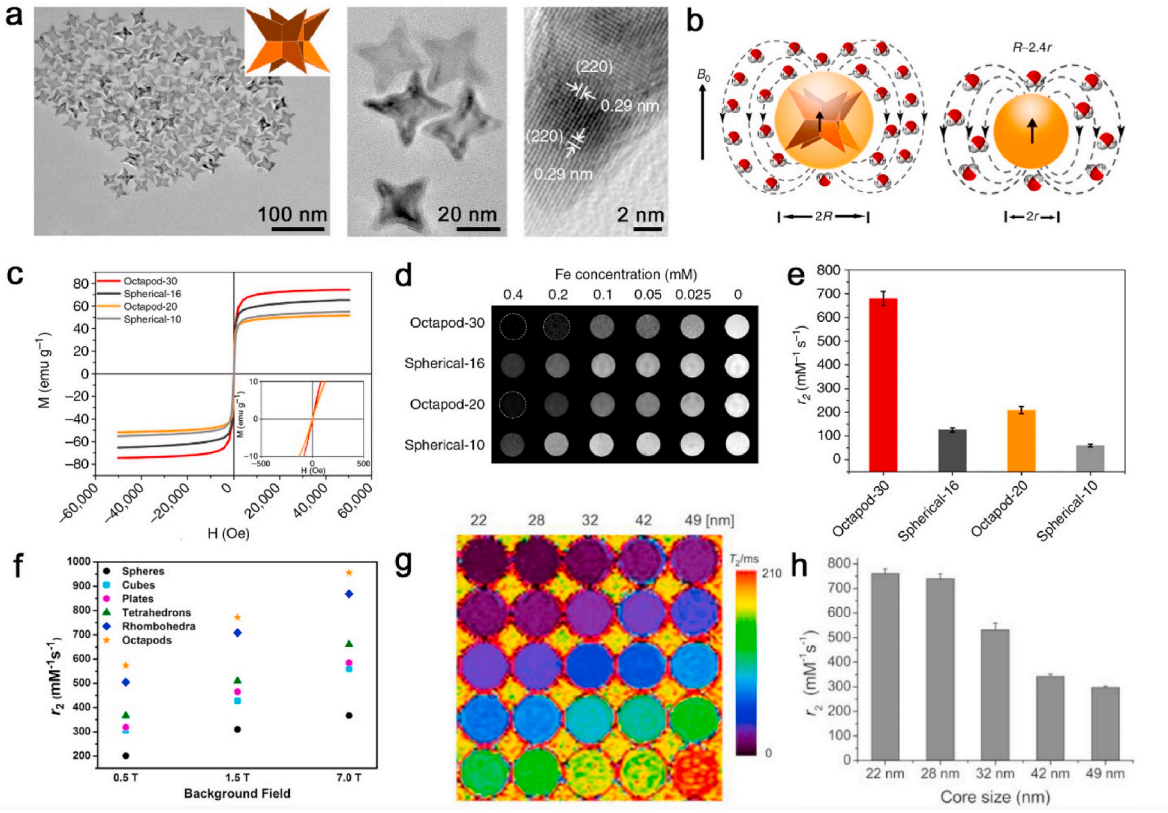

Fig. 3. Effective radius effect of single IONP on its T_2 relaxivity. (a) TEM and HRTEM images of octapod IONP with four-armed star-like particles. (b) Schematic cartoon shows the ball models of octapod and spherical IONP with the same geometric volume. With the same geometric core volume, octapod IONP shows larger effective volume than spherical IONP. (c) M − H curves of Octapod-30, Octapod-20, Spherical-16, and Spherical-10 measured at 300 K. (d) T_2-weighted MRI images and (e) r_2 values of Octapod-30, Octapod-20, Spherical-16, and Spherical-10, respectively. Reproduced with permission [154]. Copyright 2013, Nature Publishing Group. (f) r_2 values of IONPs with different morphologies, including sphere, cubes, plates, tetrahedrons, rhombohedra, and octapod. Reproduced with permission [160]. Copyright 2018, American Chemical Society. (g) Color-coded T_2-weighted MRI images and (h) comparison of r_2 values of ferrimagnetic cubic IONPs. Reproduced with permission [158]. Copyright 2012, American Chemical Society. (For interpretation of the references to color in this figure legend, the reader is referred to the Web version of this article.)

hydrophobic IONP inside the core of polymeric micelle to form IO nanocluster (Fig. 4a–d) [164]. The T_2 relaxivity of IO nanocluster is approximately 6 times higher than individual IONP coated by PEG. Additionally, they observed that T_2 relaxivity increased with the increasing of the size and loading density of IONP. Compared to polymer, silica with high surface area and high-biocompatibility has been used as the matrix to construct IO nanocluster. For example, modifying dye doped silica with multiple IONP to improve the T_2 relaxivity of IONP has been reported (Fig. 4e–g) [165]. MRI contrast ability investigation indicates that r_2 value of silica based IO nanocluster is about 2.8 times higher than that of dispersed IONP. This clustering effect based T_2 relaxivity enhancement has also been observed in other researches, indicating its universality [21,166–168]. Besides, encapsulated IONP within silica matrix have been proved to develop high-performance IO nanocluster [162]. Weissleder and co-authors develop a strategy to encapsulate multicore IO nanocluster within the thin silica shell. With the increasing of size, IO nanocluster locates in MAR, SDR, and ELR, respectively. The IO nanocluster shows the highest T_2 relaxivity in SDR with the value of 695 $mM^{-1}s^{-1}$. These size-dependent T_2 relaxivity changing tendency of IONP has also been observed by Weller and co-authors. Moreover, Weller and co-authors further investigate the effect of size of clustered single IONP on the T_2 relaxivity of IO nanocluster [163]. They found that the T_2 relaxivity is regardless of the size of clustered single IONP in MAR. In contrast, T_2 relaxivity of IO nanocluster in the SDR seems to increase with size rising of the clustered single IONP. Since the size of IONP is proportional to its magnetic moment, these results may indicate that the T_2 relaxivity in SDR could be further increased by optimizing the magnetic property.

2.4. Synergistic effect of magnetic behavior and effective radius

Since individually increase the M_s and effective radii of IONP could improve its T_2 relaxivity, one can hypothesize that simultaneous increase M_s and effective radius of IONP could further increase its T_2 relaxivity. Unfortunately, the traditional synthetic method limits the simultaneous controlling the crystal structure and morphology. With the development of synthetic method, more and more researches on simultaneous improving M_s and effective radius of IONP have been reported. Zhao et al. developed a novel strategy to improve M_s and effective radii of IONP through cation exchange reaction (Fig. 5a–e) [169]. They successfully synthesized cubic and octapod IONPs with high effective radii and magnetization moment. These engineered IONPs exhibit outstanding capacity to achieve T_2 contrast enhancement, especially zinc engineered octapod IONP (r_2 = 754.2 $mM^{-1}s^{-1}$ at 7 T). More recently, Gao and co-workers further elevate the dopant level of zinc in octapod IONP to further increase M_s of IONP with high effective radius (Fig. 5f–h) [170]. The saturated magnetizations show the anti-V shape trend with the rising of zinc doping level. With the doping level of x = 0.44, the M_s value reaches to the peak with the value of 88.9 emu/g (88.9 $A{\cdot}m^2/kg$). On the basis of the high effective radius and M_s value, octapod $Zn_xFe_{3-x}O_4$ nanoparticle (x = 0.4) exhibit the notably high T_2 relaxivity with the value of 989.1 $mM^{-1}s^{-1}$ at 7 T, which endow it as a sensitive T_2 CA to fulfill the sensitive detection on orthotopic and metastatic tumor on mice model.

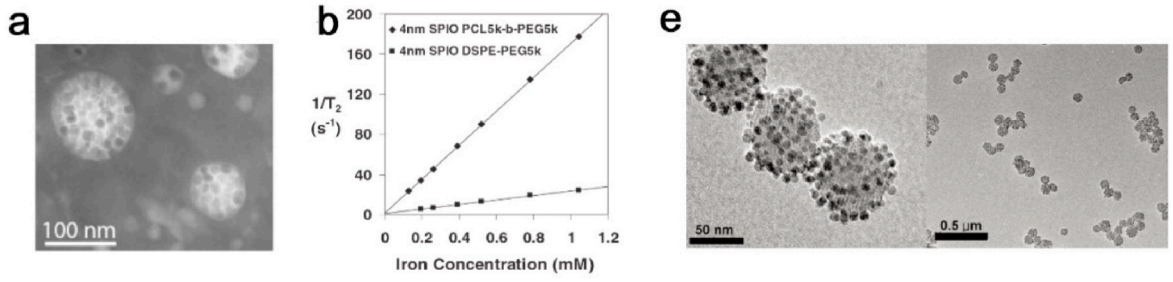

d

Micelle formulation	Micelle size [nm]	SPIO loading [wt.-%]	r_1	r_2	MRI sensitivity [μg mL^{-1}]
4 nm SPIO DSPE-PEG5k	17±1	12.4	1.3	25.1	450
4 nm SPIO PCL5k-b-PEG5k	75±4	19.5	2.9	169	20.5
8 nm SPIO PCL5k-b-PEG5k	97±6	38.1	1.6	318	6.9
16 nm SPIO PCL5k-b-PEG5k	110±9	54.2	2.0	471	5.2

Fig. 4. Assembled effect on T_2 relaxivity of IONP. (a) TEM images of IONP-loaded micelles after negative staining. (b) T_2 relaxivity and (c) T_2-weighted MRI images of 4 nm IONP-loaded PCL5k-b-PEG5k micelles and DSPE-PEG5k micelles at 1.5 T. (d) Table of T_1 relaxivities, T_2 relaxivites, and MRI sensitivity of different IONP-loaded micelles. Reproduced with permission [164]. Copyright 2005, John Wiley & Sons, Inc. (e) TEM images of IONP-MSN. (f) Plot of T_2 relaxation and (g) T_2-weighted MRI images of IONP-MSN and free IONP with the same Fe concentration. Reproduced with permission [165]. Copyright 2009, American Chemical Society.

2.5. Inhomogeneous magnetic field

Theoretically, the diffusion of protons in the inhomogeneous magnetic field will lead to the dephasing of proton, which is the basis of the T_2 relaxation generation. The existence of T_2 MRI CA could generate an inhomogeneous magnetic field around it and accelerate the dephasing process of around protons, which is the basic goal of T_2 CA [119,121,171,172]. The improvement of magnetic moment and size of IONP can enhance the local gradients of magnetic field around it and shorten the spin-spin relaxation time. Besides, IONP with anisotropic morphology, especially with sharp corner, could enhance the inhomogeneity of surrounding magnetic field. For instance, Gao and co-authors investigate the effect of the stray field gradient generated by $Mn_xFe_{3-x}O_4$ nanoparticles with different anisotropic morphologies on their T_2 relaxivities (Fig. 6a–f) [160]. The Landau-Lifshitz-Gilbert (LLG) equation simulations indicate that different morphologies could effectively affect the shape, intensity, and gradient of the stray field. Moreover, the stray field generated by octapod morphology with eight sharp corners shows the highest inhomogeneity, resulting in the highest T_2 contrast among all samples. Recently, Zhou et al. investigate the inhomogeneity of stray magnetic field generated by IO based nano-cluster (Fig. 6g–s) [173]. They prepared a series of IO nano-clusters, including C1 (5 nm IONP only), C2 (15 nm IONP only), C3 (mixed 5 and 15 nm IONP), C6 (cubic IONP), C7 (plate IONP). The LLG simulation results indicate that magnetic field generated by C3 shows stronger inhomogeneity compared to C1 and C2. Therefore, C3 present significantly higher T_2 relaxivity (533.4 mM^{-1}s^{-1}) than C1 (231.6 mM^{-1}s^{-1}) and C2 (358.3 mM^{-1}s^{-1}). This magnetic field inhomogeneity based T_2 relaxivity enhancement is also observed in C6 and C7. These IO nano-clusters constructed by IONPs with anisotropic morphologies show enhanced magnetic field inhomogeneities and improved T_2 relaxivities compared to the traditional IO nano-clusters. Since electrons of atom surrounding the magnetic nanoparticles undergo circulation under external magnetic field, which could generate a small opposite magnetic field to the external magnetic field and further increase the inhomogeneity of local magnetic field, local magnetic field inhomogeneity could also be increased by the surface ligand of IONP as well. Gao and co-author investigated the influence of anchoring group on the local magnetic field [174]. They found that IONP modified by catechol and hydroxamate group generated stronger inhomogeneity than that modified by diphosphate group, due to the greatly contribution of π electron circulation on increasing the inhomogeneity of local magnetic field.

2.6. Surface coating structure

To act as a MRI CA for diagnosis, IONP need to be coated with hydrophilic layer, including small molecule, polymer, and protein, to disperse in aqueous solution [5,175–178]. There are two main effects of surface coating on the T_2 relaxivity of IONP. Firstly, the coating layer require an anchoring moiety to chelate with Fe^{2+} or Fe^{3+} ions on surface, which may affect its magnetic property. Secondly, the coating layer can limit the diffusion of proton and hinder the interaction between proton and magnetic field induced by IONP.

2.6.1. Effect on magnetization moment

Due to the chelating with Fe^{2+} and Fe^{3+} ions, the coating layer may affect the arrangement of surface atoms and magnetization moment. Serna and co-authors report that the coordination of oleic acid to the

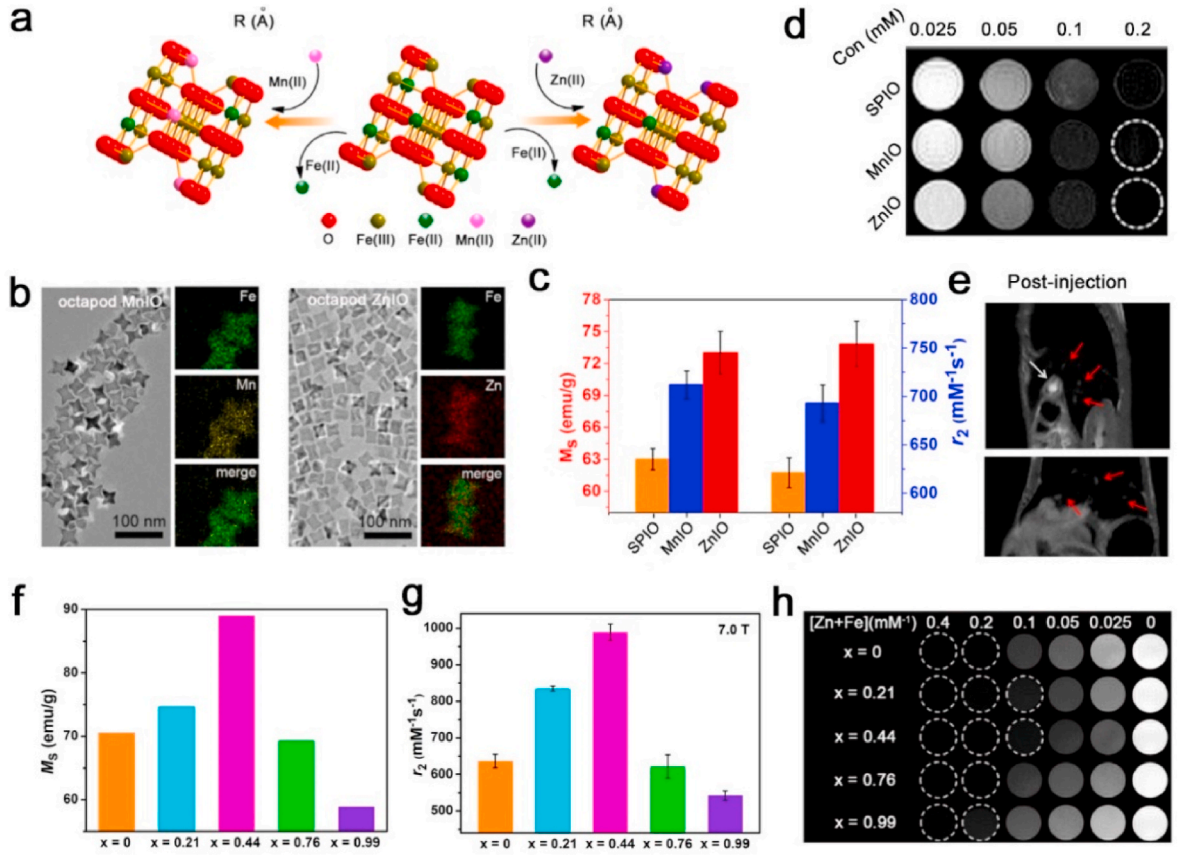

Fig. 5. Simultaneous optimization of magnetic behavior and effective radii to improving T_2 relaxivity. (a) Scheme of cation exchange in IONP. (b) TEM images of octapod IONP treated by Mn and Zn cations. (c) Comparison of M_s and (d) r_2 values and T_2-weighted MR images of octapod IONP treated by Mn and Zn cations. (e) *In vivo* MRI images of metastatic hepatic carcinomas before and 1 h after intravenous injection of octapod IONP treated by Zn cations. Reproduced with permission [169]. Copyright 2016, American Chemical Society. (f) Comparison of M_s and (g) r_2 values of Zn doped IONP with different ratio. (h) T_2-weighted MR images of Zn doped IONP with different ratio at 7 T. Reproduced with permission [170]. Copyright 2019, American Chemical Society.

surface of IONP can effectively reduce the spin canting effect and increase the magnetic moment [179]. They observed that saturated magnetization of IONP coated with oleic acid (about 78 emu/g = 78 A·m^2/kg) was higher than that without oleic acid. However, recent study indicate that chelating IONP with high affinity group may introduce structure defect and disturb the long-range-order of magnetic spin. Zeng et al. investigate the different surface coating ligand on the saturated magnetization of IONP (Fig. 7a–c) [174]. They found M_s value and T_2 relaxivity of IONP decreased with the order of surface agent as hydroxamate > catechol > diphosphate, which was inversely correlated to their binding affinity to Fe^{3+} ions. This study suggests that coating IONP with moderate affinity group could optimize its magnetic property and improve its T_2 contrast.

2.6.2. *Proton diffusion*

T_2 relaxation of proton is highly determined by its diffusion behavior in the magnetic field gradients. The coating layer could affect the diffusion of proton by reducing the diffusion magnetic field strength, limiting proton diffusion, and forming hydrogen bond to proton. Previous research reported that the magnetic field generated by IONP decreased with the increase of the distance between IONP surface and proton. When the coating thickness increases to 10.8 nm, the magnetic field strength reduces to 2.3% of that on the surface [183]. This undesirable decrease may lead to the drop of T_2 relaxivity of IONP. Dravid and co-authors found that with the increasing of silica shell thickness from 1 to 14 nm, the T_2 relaxivity of IONP decreased from 94 to 32 mM^{-1}s^{-1} (Fig. 7d and e) [180]. Meanwhile, the coating layer reduces the proton diffusion efficiency within the layer, which benefits to its T_2 relaxivity. Thus, one can optimize the coating layer structure to enhance the T_2 relaxivity of IONP. Tong et al. investigated the effect of molecular weight of PEG on the T_2 relaxivity of IONP (Fig. 7f–i) [181]. They modified 5 and 14 nm IONP by PEG chain with molecular weight of 550, 750, 1000, 2000, and 5000 Da, respectively. Regardless of the core size, T_2 relaxivity of PEG modified IONP is highly related to the molecular weight of PEG and show specific plateau with a certain value. Additionally, bio-macromolecule, especially protein, have been proved to be a new candidate to optimize the coating layer. Mao and co-authors developed a high-performance T_2 CA by coating IONP with casein (Fig. 7j-m) [182]. The T_2 relaxivity of casein coated IONP is about 2.5 times higher than that coated by amphiphilic polymer. The high T_2 relaxivity could be mainly attributed to the high permeability, high affinity to proton, and abundant hydrate group of casein. Based on these unique features, the casein coating layer benefits the diffuse of surrounding proton and increases the exchange efficiency between hydrate water and bulky one. This T_2 relaxivity enhancement effect could be expanded to other proteins, such as human serum albumin. The detailed theoretical and experimental discussion on T_2 contrast of IONP clearly indicate the limitation parameters, such as M_s, effective radius, dephasing process and proton diffusion, on the r_2 value of IONP (see Table 1). We highlight those strategies to optimize these parameters to improve T_2 contrast of IONP, which encourage further investigations on improving T_2 contrast of IONP.

3. IONP as T_1 CA

IONP shows high biocompatibility, which is highly desirable for

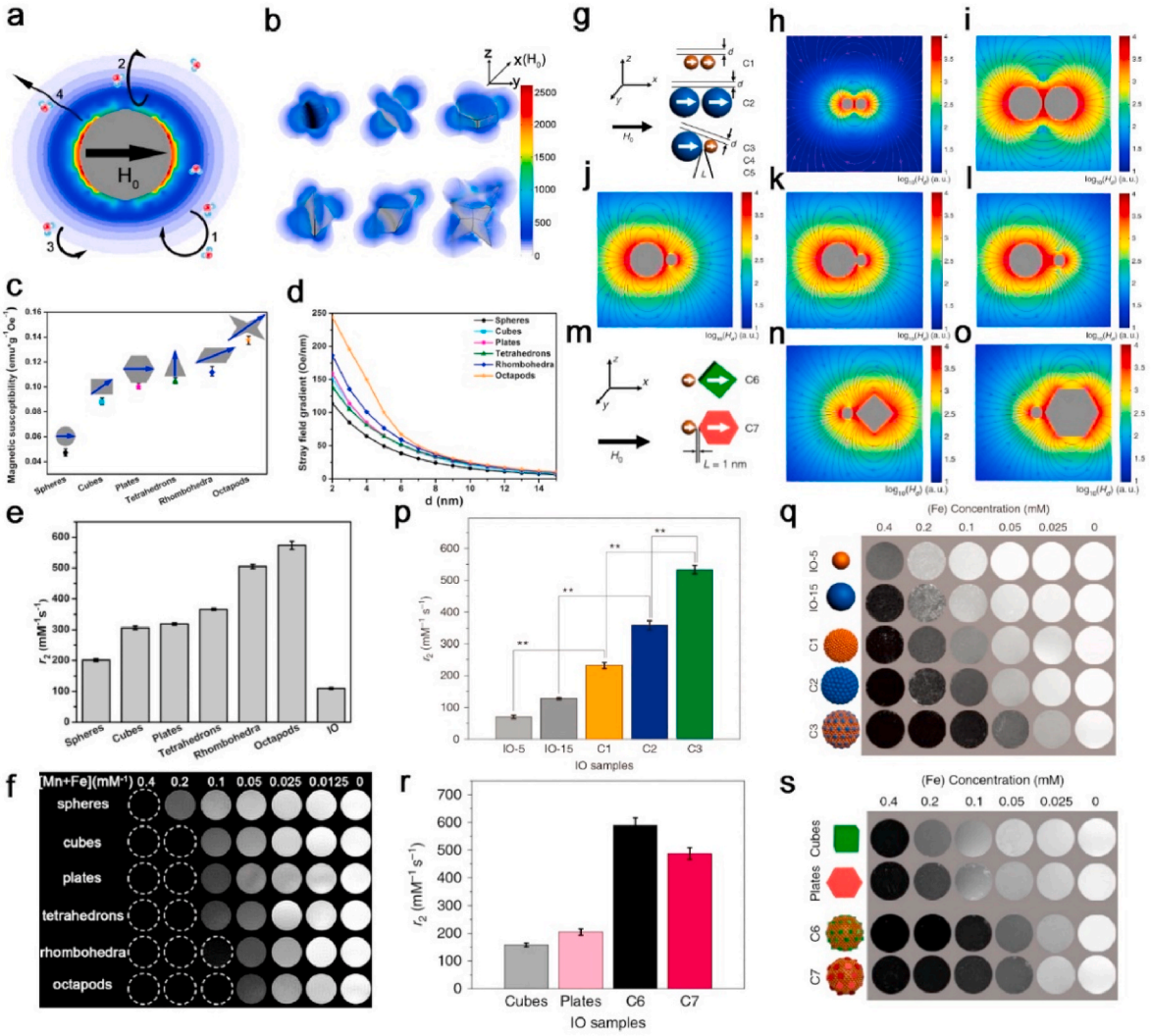

Fig. 6. Inhomogeneous magnetic field effect on T_2 relaxivity of IONP. (a) Scheme of water molecular diffusion and relaxation process around spherical IONP. The color indicates the intensity of local field induced by IONP under an external magnetic field. (b) The spatial distribution of stray fields caused by IONP with different morphologies. (c) Values of magnetic susceptibility and (d) stray field gradient *vs* distance from the surface of IONP with different morphologies. (e) r_2 values and (f) T_2-weighted MR images of IONP with different morphologies at 7 T. Reproduced with permission [160]. Copyright 2018, American Chemical Society. (g) Schematic cartoon illustrates the simulation of two adjacent IONP of different size. (h–l) Landau-Lifshitz-Gilbert simulation results of the stray field for model C1–C5, respectively. (m–o) Simulation models and the calculated stray fields for the models C6 and C7, respectively. (p) Comparison of r_2 values and (q) T_2-weighted MR images of IO-5, IO-15, C1, C2, and C3, respectively. (r) Comparison of r_2 values and (s) T_2-weighted MR images of cubic IONP, C6, and C7, respectively. Reproduced with permission [173]. Copyright 2017, Nature Publishing Group. (For interpretation of the references to color in this figure legend, the reader is referred to the Web version of this article.)

biomedicine application. However, traditional IONP exhibits relatively low T_1 relaxivity and high r_2/r_1 ratio, hindering its application as the T_1 CA [46,155]. Theoretically, T_1 relaxivity of IONP is determined by the chemical exchange efficiency between magnetic ions and proton, which is highly dependent on its crystal structure. Recently, a growing attention have focused on engineering crystal structure of IONP to improve its T_1 relaxivity and construction of IONP based T_1 CA.

3.1. SBM theory

T_1 CAs lead to the energy loss of spin through dipole-dipole interactions between water protons and magnetic ions, which causes the T_1 relaxation occur [184,185]. There are three regions for interactions between water proton and magnetic ions, inner-sphere, secondary intermediate sphere, and outer sphere [117]. The inner-sphere describes direct interaction between water protons and magnetic ions and dominates the T_1 relaxation enhancement for the T_1 CAs. In secondary intermediate sphere and outer sphere, magnetic ions interact with the diffusing protons and exchangeable protons, which are not directly bind to the magnetic ions and accompany the exchange through hydrogen bond [186,187]. However, the secondary intermediate sphere and outer sphere mediated T_1 relaxation enhancement are negligible compared to that caused by the inner sphere. Therefore, secondary intermediate sphere and outer sphere are often ignored due to the present of water proton in inner sphere in a real system. The r_1 value in inner sphere is given by [188,189].

$$R_1 = qP_m[1/(T_{1m} + \tau_m)] \tag{3}$$

$$\frac{1}{T_{1m}} = \frac{2}{15}\frac{\gamma^2 g^2 S(S+1)\mu_B^2}{r^6}\left[\frac{3\tau_{c1}}{1+\omega_H^2\tau_{c1}^2} + \frac{7\tau_{c2}}{1+\omega_s^2\tau_{c2}^2}\right] \tag{4}$$

$$1/\tau_{ci} = 1/\tau_r + 1/\tau_{is} + 1/\tau_m \tag{5}$$

Where P_m is the mole fraction of water coordinating to the metal center,

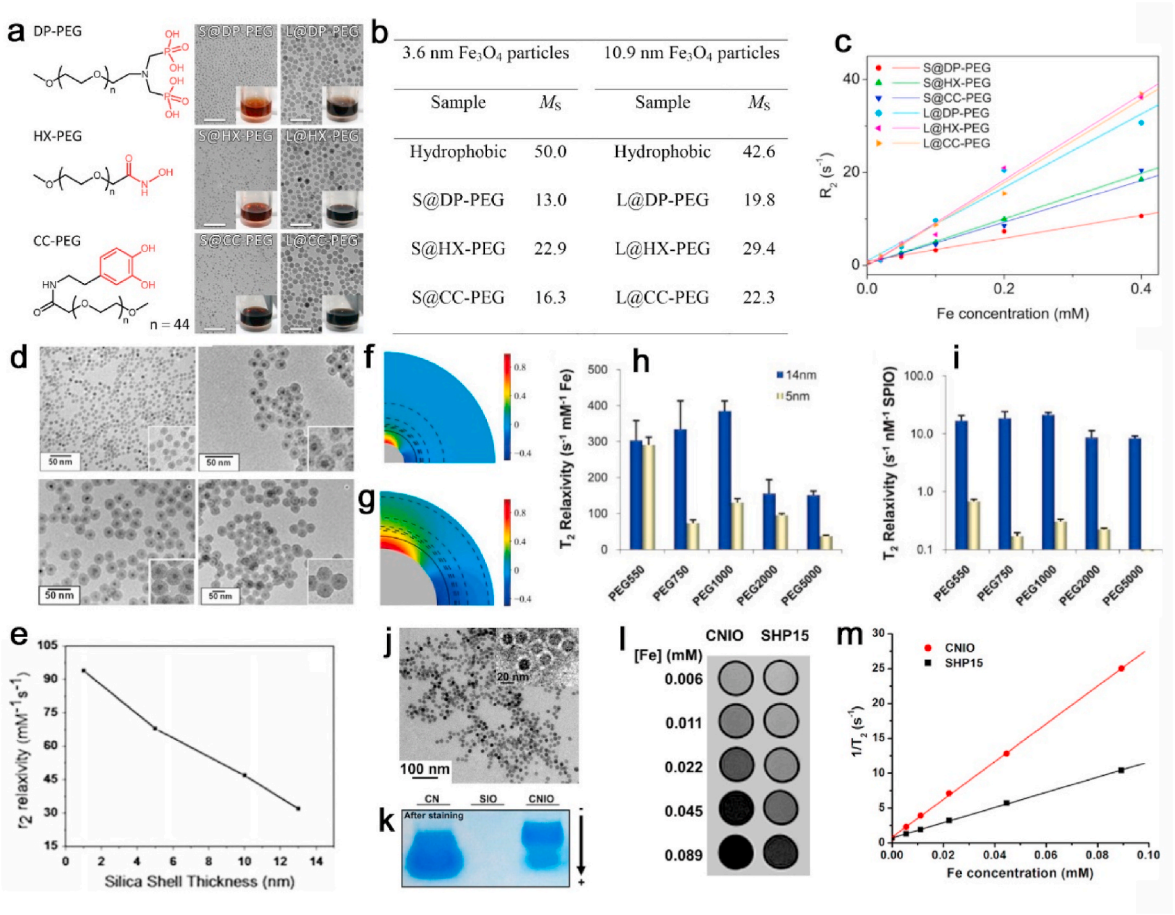

Fig. 7. Effect of surface coating structure on T_2 relaxivity of IONP. (a) Chemical structure of PEG used for exchanging and TEM images of PEGylated IONP with the sizes of 3.6 and 10.9 nm, respectively. (b) M_s values and (c) plot of T_2 relaxation rates of PEGylated IONPs with the sizes of 3.6 and 10.9 nm. Reproduced with permission [174]. Copyright 2014, John Wiley & Sons, Inc. (d) TEM images and (e) r_2 values of silica coated IONPs with different silica shell thickness. Reproduced with permission [180]. Copyright 2013, Springer Nature. Normalized magnetic field of IONP with the sizes of (f) 5 and (g) 14 nm. The color bar represent the magnitude of the magnetic field strength. Starting from center, the dash lines indicate PEG550, PEG750, PEG1000, PEG2000, and PEG5000. T_2 relaxivities of different PEG coated IONPs with constant (h) iron concentration or (i) particle concentrations. Reproduced with permission [181]. Copyright 2010, American Chemical Society. (j) TEM images of casein coated IONP. (k) Pictures of gel analyses of casein and oligosaccharide or casein coated IONP. (l) T_2-weighted MR images and (m) T_2 relaxation rates of casein and polymer coated IONP. Reproduced with permission [182]. Copyright 2013, American Chemical Society. (For interpretation of the references to color in this figure legend, the reader is referred to the Web version of this article.)

T_{1m} is the applicable dipole-dipole relaxation, q is the coordination number of water, τ_m is proton residence lifetime, τ_{ci} [i = 1,2] is the correlation time, τ_r is the molecular tumbling time, r is the distance between magnetic ions and proton, and τ_{is} is the electronic relaxation time. Ideally, a given T_1 CA with large q, short τ_m, long τ_r, and long τ_s exhibits high T_1 relaxivity. Since IONP with large size show long τ_r compared to metal complex, improvement on q, τ_m, and τ_s is the main method to increase its T_1 relaxivity. However, IONP with high T_1 relaxivity does not mean that it is suitable to be used as the T_1 CA. The key parameter to determine whether a specific IONP could be considered as T_1 CA is its r_2/r_1 ratio. For example, 12 nm $Mn_xFe_{3-x}O_4$ nanoparticle show high T_1 relaxivity with the value of 38.2 $mM^{-1}s^{-1}$ while high r_2/r_1 ratio with the value of 7.4. The relative high r_2/r_1 ratio suggests that 12 nm $Mn_xFe_{3-x}O_4$ nanoparticles should be considered as the T_2 CA [153]. In this section, we will discuss the effective strategies to construct IONP based T_1 CA with the low r_2/r_1 ratio.

3.2. Reduction of magnetic moment

IONP exhibits high magnetization, meaning high T_2 contrast ability and high r_2/r_1 ratio. This defect highly hinders its application as a T_1 CA and should be overcome to develop IONP based T_1 CA. The magnetic property of IONP is highly determined by its crystal structure. One can optimize some key parameters, including size, crystallinity, and surface modification, to adjust the magnetic moment of IONP and develop T_1 CA. Recently, many strategies have been reported to reduce the magnetic moments of IONPs and optimize their r_2/r_1 ratio, which have been proved to be effective method to develop IONP based T_1 CA.

3.2.1. Spin disorder surface

Magnetic moment of IONP is highly dependent on its size. Normally, the magnetic moment decreases with the drop of its size, which could be ascribed to the increase of the spin disorders on the surface of IONP. This spin disorder surface of IONP are lack of full alignment and may destroy the long-range-order of magnetic spins, which could trigger the decrease of magnetic moment [144,146,190,191]. Since the thickness of this spin disorder surface is almost constant, the ratio of spin disorder surface to whole particles increase with the size decrease. For example, the proportion of spin disorder surface to entire particle is about 35% for 12 nm IONP, while increases to 48% when the size decreases to 5 nm [192]. Therefore, reducing the core size of IONP is the most straightforward method to reduce the magnetic moment of IONP and develop T_1 CA. Hyeon and co-authors synthesized IONP with size of 3 nm and investigated its T_1 contrast (Fig. 8a–e) [46]. Due to the remarkable spin canting

Table 1
The limitation parameters on the r_2 value of IONP and current strategies to optimize these parameters in different regions.

regime	Optimized Parameter	Strategy	r_2 value ($mM^{-1}s^{-1}$)
MAR	M_s	Dopant with Mn ions	358 (1.5 T) [27]
		Dopant with Mn ions	687 (4.5 T) [135]
		IONP coated iron	324 (9.4 T) [139]
		Coated monometallic iron with Mn doped IONP	430 (0.47 T) [141]
		Reducing magnetically dead layer	175 (1.7 T) [148]
	Effective radii	IONP with octapod morphology	679 (7 T) [154]
		Clustering of IONP through polymer	471 (1.5 T) [164]
	Effective radii/ Ms	Zn doped octapod IONP	989 (7 T) [170]
	Dephasing process	IO cluster with muti-single core	533 (7 T) [173]
		IONP modified by hydroxamate group	92 (3 T) [174]
	Proton diffusion	Adjusting thickness of shell	385 (7 T) [181]
		Coating IONP with casein	273 (3 T) [182]
SDR	M_s	Cubic IONP	800 (3 T) [158]
		Increasing the size of clustered single IONP	~330 (1.41 T) [163]

effect, IONP with the size of 3 nm shows lower magnetic moment, higher T_1 relaxivity, and lower r_2/r_1 ratio compare to 12 nm IONP. However, the T_1 relaxivity of IONP does not always increase with the decrease of their sizes. Shen et al., reported that with the size increase, the r_1 value of IONP shows an anti-V shape curve and reach the plateau with the size of 3.6 nm (Fig. 8f and g) [193]. Interestingly, the r_2/r_1 change exhibits a contrary tendency to r_1 change and reach the minimum at the size of 3.6 nm.

3.2.2. *Crystal phase*

Magnetite phase of IONP show the highest magnetic moment and is considered as the best candidate for T_2 contrast imaging among all phases. However, the high magnetic moment result in the high r_2/r_1 ratio and hinder its application as T_1 CA. Wüstite and Maghemite phase have been reported to show relative lower magnetic moment than magnetite phase, endowing them with the suitable magnetic property to reveal low r_2/r_1 ratio and be used as the T_1 CA [194,195]. Compared to Wüstite phase composed with Fe^{2+} cations (4 unpaired electrons), maghemite phase composed with Fe^{3+} cations (5 unpaired electrons) presented higher q values and T_1 relaxivity. Bawendi and co-authors fully oxidized the synthesized IONP from magnetite phase to maghemite by trimethylamine N-oxide [196]. The resultant product shows high T_1 relaxivity with the value of 5.2 $mM^{-1}s^{-1}$ and relatively low r_2/r_1 ratio with the value of 2.0 at 1.5 T, ensuring it to fulfill MRA and conventional T_1 MRI contrast *in vivo*.

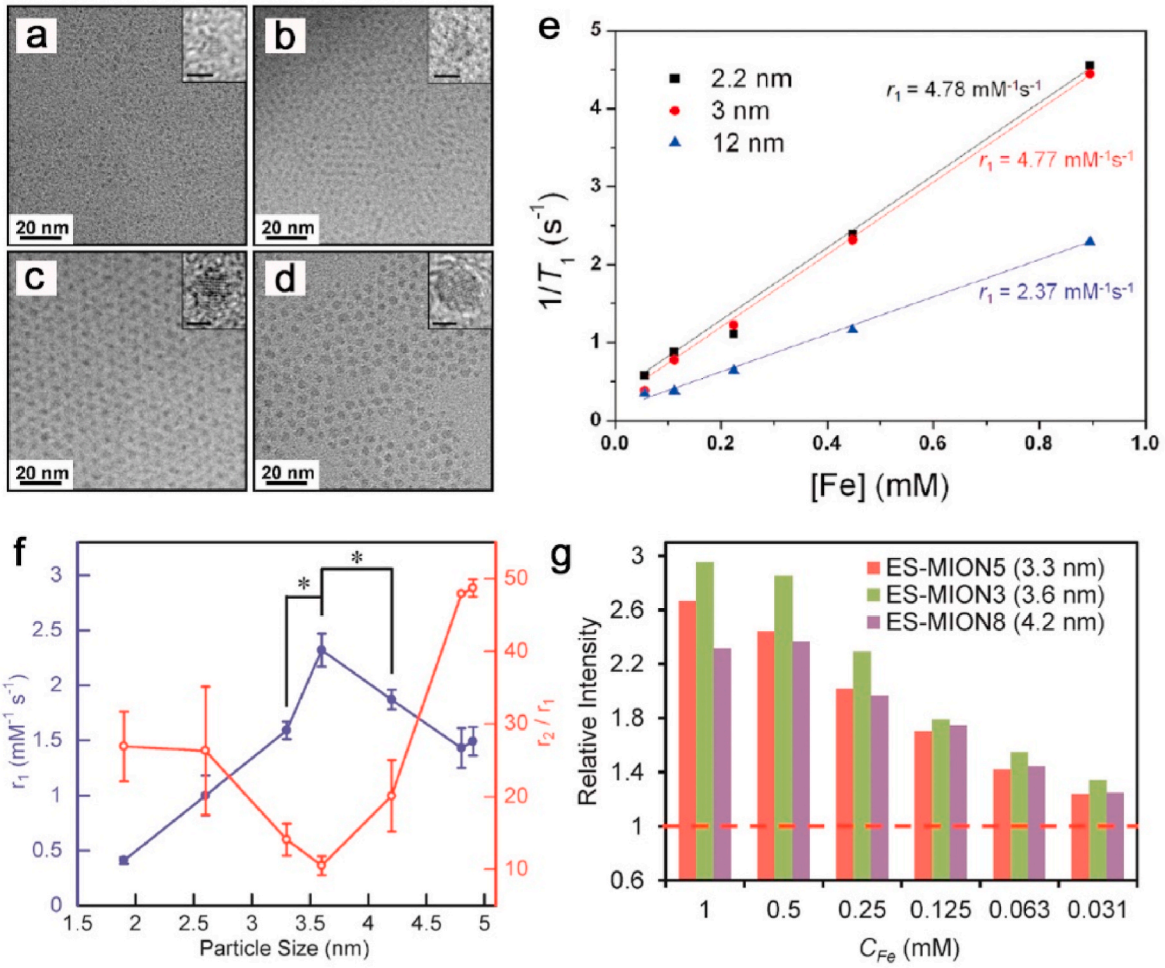

Fig. 8. Effect of spin disordered surface and crystal phase on T_1 relaxivity of IONP. TEM images of IONP with the sizes of (a) 1.5, (b) 2.2, (c) 3, and (d) 3.7 nm, respectively. (e) Plot of T_1 relaxation rate of IONP with different sizes. Reproduced with permission [46]. Copyright 2010, American Chemical Society. (f) r_1 value and r_2/r_1 ratio of exceedingly small IONP as a function of sizes. (g) Relative intensity of MR images for exceedingly small IONP with the sizes of 3.3, 3.6, and 4.2 nm, respectively. Reproduced with permission [193]. Copyright 2017, American Chemical Society.

3.3. Coordination number of water (q)

Theoretically, q is proportional to the T_1 relaxivity of T_1 CA. For IONP, its T_1 shorten effect could be attributed to existed iron ions on its surface. Since q of iron ion is constant, the straightforward method to optimize the q of IONP is increase the number of iron ions on surface [155,197,198]. The number of iron ions exposed on the surface of IONP is determined by two key factors: One is the surface to volume ratio, the other is the exposed crystal facet. Ordinarily, high surface to volume ratio and iron rich facet exposure are desirable to increase the number of iron ions on the surface of IONP. Thanks to the development of synthetic method, more and more IONPs with high surface to volume ratio and iron rich exposed surface have been reported to pursue IONP based high-performance T_1 CA [44,199–202]. In addition, q of T_1 CA is highly dependent on the number of unpaired electrons. Recently, introducing other magnetic ions with large amounts of unpaired electrons into crystal structure of IONP have been discovered to increase the q of IONP and elevate its T_1 relaxivity [53,61,203–207]. Here, strategies to increase q of IONP to raise its T_1 relaxivity have been reviewed in the following section.

3.3.1. Hollow structure

Surface iron ions of IONP, conducting chemical exchange with protons and accelerate their longitudinal relaxations, could be considered as the effective iron ions. Unfortunately, the chemical exchange between inner iron ions and protons have been blocked by the outershell, resulting in a reduction of the number of effective iron ions in IONP. Hollow structures with two interfaces between nanocrystal and surrounding environment can exceedingly rise the number of exposed magnetic ions, which is beneficial to elevate T_1 contrast of IONP [208–211]. Additionally, the hollow structure may disturb the long-range-order of magnetic spin and reduce magnetic moment, lowering the r_2/r_1 ratio. Inspired by these results, IONP with hollow structure have been synthesized to develop IONP based T_1 CA. Wei et al. synthesized hollow porous IO nanobox via the template-based method (Fig. 9a–e) [210]. The r_1 value of hollow IONP with the size of 14 nm is about 27.2 $mM^{-1}s^{-1}$, which is about 2.5 times higher than that of solid spherical IONP with similar size. More importantly, hollow IONP exhibits lower r_2/r_1 ratio than corresponding solid IONP with the value of 2.0 *vs* 10.4 due to its low magnetic moment. These results clearly demonstrate the promising potential of hollow IONP as a new T_1 CA with improved T_1 contrast. However, there are two key factors that should be paid attention to fabricating hollow IONP based T_1 CA, those are density and thickness of the shell. Since the elevation of T_1 relaxivity is mainly attributed to the addition of a new interface between IONP and proton environment, the efficiency of chemical exchange between iron ions in inner interface and proton determine the T_1 relaxivity of hollow IONP. The density and thickness determine the efficiency of water proton enter the cavity and achieve the chemical exchange. Thus, the desired hollow IONP based T_1 CAs should exhibit porous and thin shell.

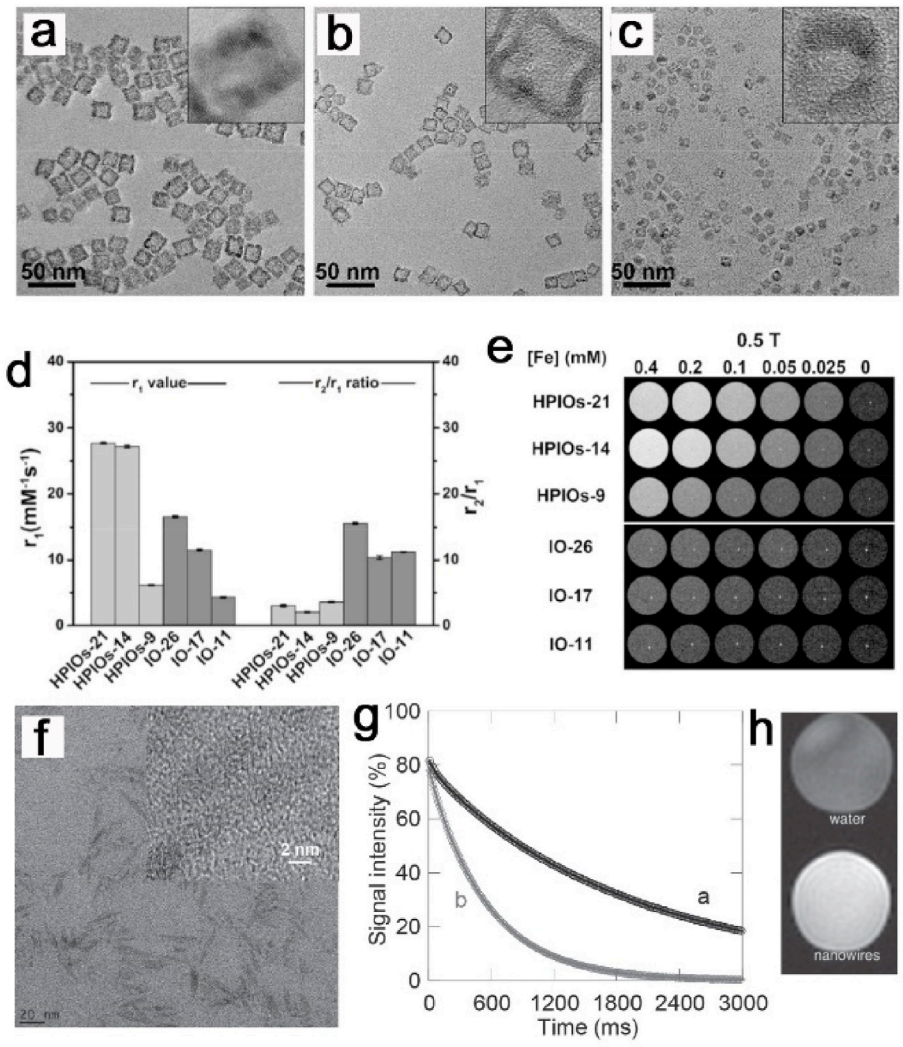

Fig. 9. Effect of surface-to-volume ration on T_1 relaxivity of IONP. TEM images of hollow porous IONP with the sizes of (a) 21, (b) 14, and (c) 9 nm, respectively. (d) Relaxation measurements and (e) T_1-weighted phantom images of hollow porous IONPs with different sizes at 0.5 T. Reproduced with permission [210]. Copyright 2018, American Chemical Society. (f) TEM images of ultrathin IO nanowhisker. (g) T_1 relaxation curve and (h) T_1-weighted images of water and IO nanowhisker. Reproduced with permission [201]. Copyright 2015, John Wiley & Sons, Inc.

3.3.2. Morphology

The T_1 relaxivity of spherical IONP have been comprehensively investigated. Changing the morphology of IONP from spherical to some specific shape can increase its surface-to-volume ratio and elevate the number of exposing magnetic ions. Consequently, the efficiency of chemical exchange reaction to surrounding proton and T_1 relaxivity of IONP improved. For example, the surface-to-volume ratio of cubic morphology is remarkably higher than that of spherical morphology. Demir and co-authors synthesized IO nanocubes with the size of ~9.7 nm [212]. The T_1 relaxivity assessment indicates that the r_1 value of this cubic IONP is about 8.3 $mM^{-1}s^{-1}$, which is higher than that of 3 nm spherical IONP. Author contribute this elevation effect on T_1 relaxivity to the increased surface-to-volume ratio from spherical to cube. Besides, T_1 contrast ability of IO nanowhisker with small diameter have been evaluated by Macher et al. (Fig. 9f–h) [201]. IO nanowhisker shows large aspect ratio with the length of 20 nm and diameter of 2 nm, which endows it with large surface-to-volume ratio to achieve efficient chemical exchange reaction to water. With high surface-to-volume ratio, this IO nanowhisker show high T_1 relaxivity with the r_1 value of 6.13 $mM^{-1}s^{-1}$, which is significantly higher than that of Magnevist with the r_1 value of 3.3 $mM^{-1}s^{-1}$. It should note that this IO nanowhisker shows paramagnetic behavior due to the high surface-to-volume ratio, which result in forming iron-ligand complexes layer and reducing T_2 relaxivity. This effect ensure this IO nanowhisker with low r_2/r_1 ratio (1.83) to achieve sensitive T_1 contrast imaging.

Additionally, nanoparticles with anisotropic morphology can exhibit unique atomic package and show distinct interface to surrounding environment, which can affect the occupancy rate of magnetic ions on the surface and T_1 relaxivity of IONP. Zhou et al. obtained IO nanoplate with different thickness by controllable synthesis (Fig. 10a–h) [155]. This IO nanoplate exposes two Fe_3O_4 (111) facets, which are $Fe_{oct2\text{-}ter1}$ terminated. The exposed crystal facet could increase the interaction between surface iron ions and surrounding water proton. The r_1 value of IO nanoplate with the thickness of 2.8, 4.8, and 8.8 nm are 14.36 ± 1.24, 43.18 ± 3.33, and 38.11 ± 1.04 $mM^{-1}s^{-1}$, respectively, which are significantly higher than that of spherical IONP. It seems that T_1 relaxivities of IO nanoplates are highly determined by the ratio of (111) area to volume except for the 2.8 nm nanoplate, which could be attributed to the existence of spin-disorder at its corner. Further investigation on the effect of different exposed facet on T_1 relaxivity of IONP have been performed by Gao and co-authors (Fig. 10i–k) [160]. They studied T_1 relaxivity of $Mn_xFe_{3-x}O_4$ nanoparticles with the morphologies of sphere, cube, plate, tetrahedron, and octapod with the exposed facet of (100), (111), (110), and (311), respectively. They found that different exposed facets of $Mn_xFe_{3-x}O_4$ nanoparticles could provide different amounts of effective magnetic ions and result in the different increase degree on their T_1 relaxivities. The order of effective metals per a^2 on each facet is (110) > (111) ≈ (311) > (100). Unfortunately, the r_1 values of plate, tetrahedron, and octapod are almost the same. These results could be ascribed to the order of surface-to-volume ratios of these morphologiesare octapod, plate, and tetrahedron, which partly offset the effect caused by the facet.

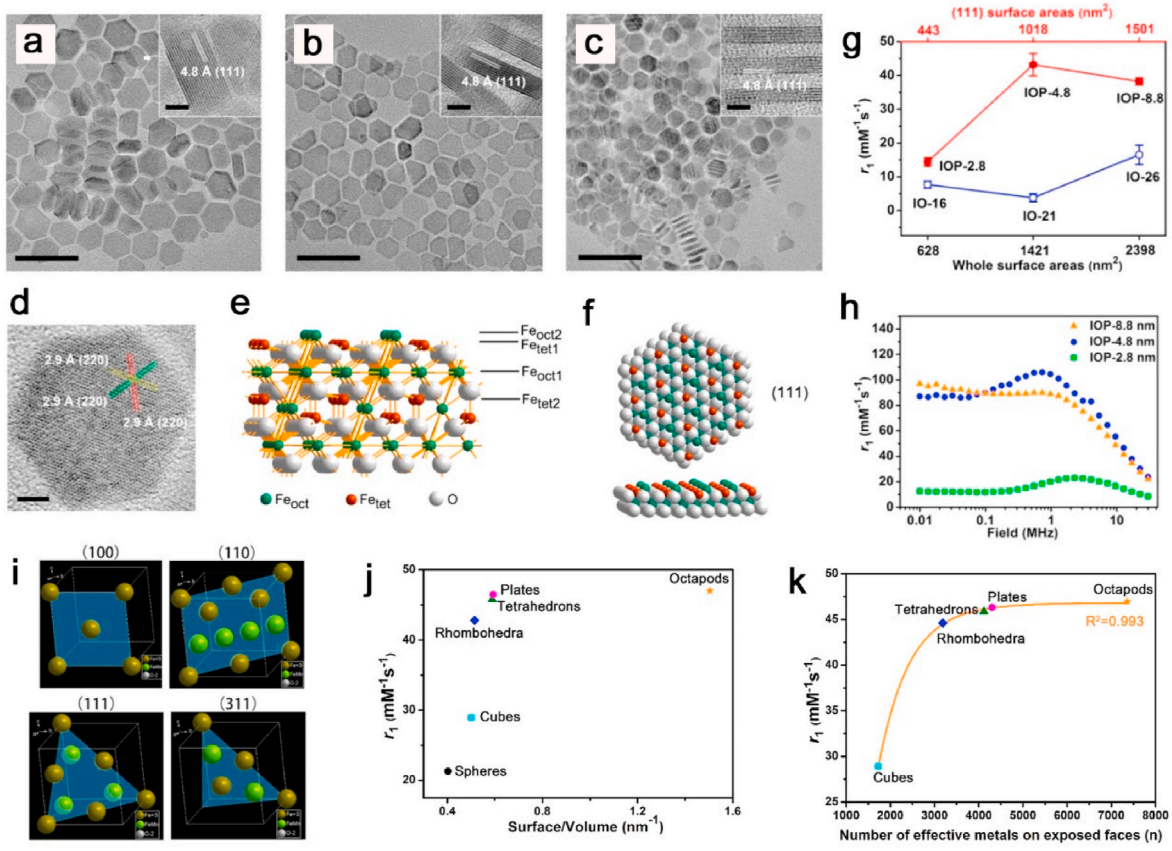

Fig. 10. Effect of anisotropic morphology on T_1 relaxivity of IONP. TEM images of IO nanoplate with the thickness of (a) 8.8, (b) 4.8, and (c) 2.8 nm, respectively. (d) HRTEM image of IO nanoplate, indicating the (220) planes. (e) Perspective and (f) top views of $Fe_{oct2\text{-}ter1}$-terminated (111) planes of Fe_3O_4 structure, showing the iron iron-rich characteristics. (g) Relationships of T_1 relaxivity with the (111) surface of IO nanoplate compare to spherical IONP with equivalent whole surface areas. (h) T_1 NMRD profiles of IO nanoplate with different thickness as the function of applied magnetic field. Reproduced with permission [155]. Copyright 2014, American Chemical Society. (i) The exposed faces of (100), (110), (111), and (311) of Mn doped IONP. (j) The relationship of surface-to-volume ratio and T_1 relaxivity. (k) The relationship of r_1 value and the number of effective magnetic metal ions on exposed facets. Reproduced with permission [160]. Copyright 2018, American Chemical Society.

3.3.3. Unpaired electron

Some magnetic ions, such as manganese and lanthanide ions own large amounts of unpaired electrons, great potential to increase q of IONP and regulate its T_1 relaxivity. Theoretically, the more unpaired electrons, the higher q could be achieved. Compared to iron ions, those ions could be divided into two types, one exhibits longer τ_s and more electrons (including Mn, Gd, and Cu), the other only shows more electrons (such as Eu). In this section, we will discuss effect of single improvement of unpaired electrons on the T_1 relaxivity of IONP. Europium (III) ions with 6 unpaired electrons and τ_s with the value of $\sim 10^{-14}$ s have been to be reported to improve the T_1 relaxivity of IONP. Yang et al. synthesized Eu doped iron oxide (EuIO) nanocube with the size of 14 nm [213]. T_1 relaxivity investigation indicates that r_1 value and r_2/r_1 ratio of this EuIO nanocube are 36.79 ± 1.16 $mM^{-1}s^{-1}$ and 2.65, which is more suitable to act as a T_1 CA compare to IONP. The elevation effect could be ascribed to higher chemical exchange of surface Eu (III) ions with nearby protons compare to iron ions.

3.4. Electronic relaxation time (τ_s)

According to SBM theory, magnetic nanoparticle with long τ_s exhibits high T_1 relaxivity. Since Fe (II) ion exhibits fewer unpaired electrons and significantly shorter τ_s than Fe (III) ion (10^{-9}–10^{-11} s and 10^{-12}–10^{-13} s for Fe (III) and Fe (II) ion) [214–216], this structure deficiency limits efficiency of relaxation enhancement of IONP in form of magnetite and limits its application as T_1 CA. Therefore, replacement of Fe (II) ions in magnetite by other magnetic ions with relative long τ_s may overcome the structure deficiency and increase the T_1 relaxivity of magnetite. In the following section, we will introduce some recent attempts to replace Fe (II) ions in magnetite and discuss the effect of different replaced magnetic ions on the T_1 relaxivity of magnetite.

3.4.1. Manganese

Manganese ions exhibit diverse valence state, such as +2, +3, +4, and +7. Among them, Mn (II) ion based probe has widely be used as a T_1 CA in MRI contrast imaging due to its paramagnetic behavior. Compared to Fe (II) ion, Mn (II) ion owns higher unpaired electron (5 unpaired electrons for Mn (II) ion and 4 unpaired electrons for Fe (II) ion) and exhibit longer τ_s (10^{-8} s for Mn (II) ion and 10^{-12}–10^{-13} s for Fe (II) ion) [217,218]. Therefore replacement of Fe (II) ion in magnetite by Mn (II) ion may efficient improve the coordination number and τ_s, optimizing its T_1 relaxivity. Huang et al. synthesized manganese engineered IONP (MnIONP) to investigate the effect of introducing Mn (II) ion on its T_1 contrast [153]. The T_1 relaxivity assessment indicates that engineered IONP with Mn (II) ion could efficiently improve its T_1 relaxivity. Gao and co-authors further engineered IONP with anisotropic morphologies by Mn (II) ion and investigated the influence of Mn (II) ion on their τ_s and T_1 relaxivity (Fig. 11a–g) [51]. The electron paramagnetic resonance spectrum analyses indicate that introducing of Mn (II) ion can remarkably increase the τ_s of pure IONP regardless of the morphologies. τ_s of MnIONP with the shape of cube, octapod, and plate are about 0.26, 0.19, and 0.23 ns, which are approximately 2.17, 2.38, and 1.44 times higher

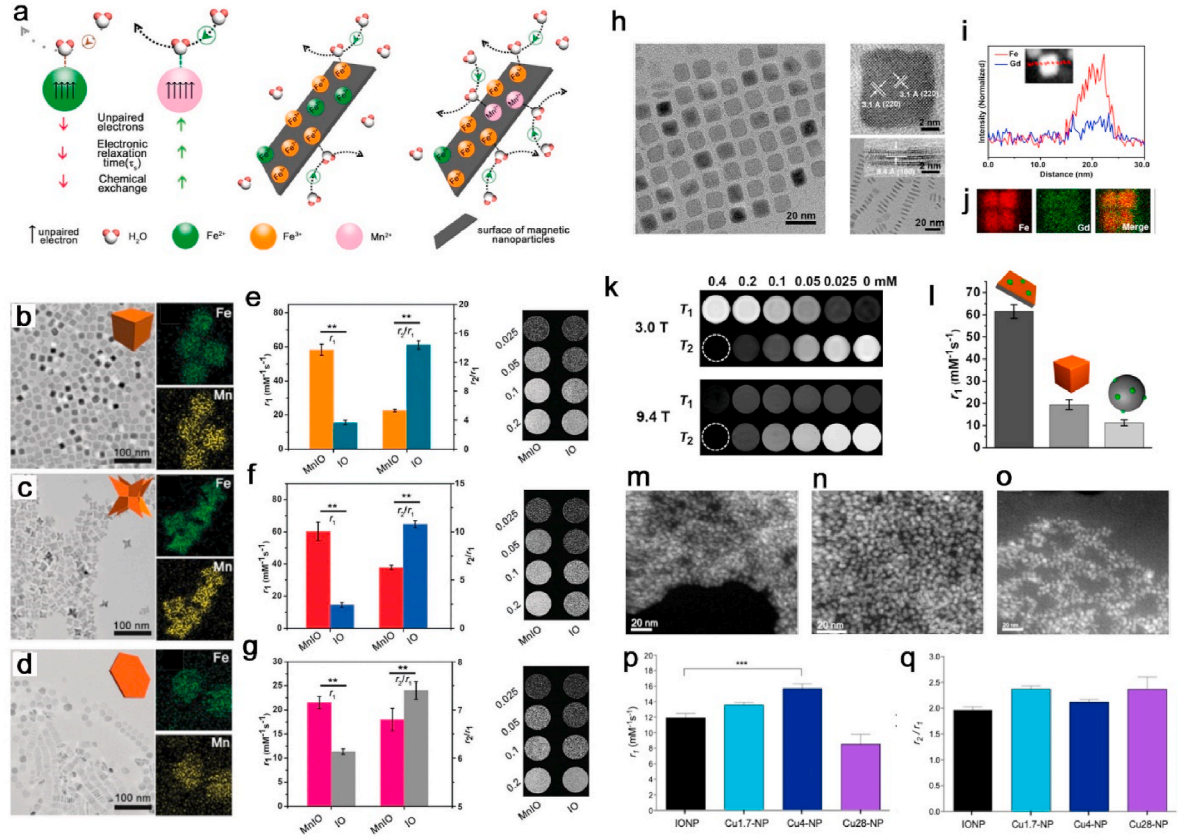

Fig. 11. Effect of τ_s on T_1 relaxivity of IONP. (a) Schematic illustration of water chemical exchange and proton relaxation enhancement phenomena in magnetic systems with surface magnetic ions in IONP and MnIONP. TEM and EDX mapping images of MnIONP with the morphologies of (b) cubes, (c) octapods, and (d) plates, respectively. r_1 values, r_2/r_1 analyses, and T_1-weighted images of MnIONP with morphologies of (e) cubes, (f) octapods, and (g) plates, respectively. Reproduced with permission [51]. Copyright 2018, The Royal Society of Chemistry. (h) TEM and HRTEM images of Gd engineered IO nanoplate. (i) EDX line-scanning and (j) mapping of Gd engineered IO nanoplate. (k) T_1-and T_2-weighted phantom images of Gd engineered IO nanoplate at 3.0 and 9.4 T. (l) Comparison of r_1 values of Gd engineered IO nanoplate, IO cubes, and Gd engineered IONP. Reproduced with permission [221]. Copyright 2015, American Chemical Society. Selected STEM-HAADF images of CuIONP with the Cu dopant ratio of (m) 1.7%, (n) 4%, and (o) 28%, respectively. (p) r_1 values and (q) r_2/r_1 ratio analyses of CuIONP with different dopant ratio. Reproduced with permission [222]. Copyright 2019, American Chemical Society.

than those of corresponding pure IONP, respectively. Coupled with the abundantly exposed magnetic ions, this τ_s elevation effect remarkably increase the T_1 relaxivities of IO nanocube, octapod, and plate to 57.8, 62.1, and 22.4 $mM^{-1}s^{-1}$ at 0.5 T.

3.4.2. Gadolinium

Due to its large amounts of unpaired electrons and long τ_s, paramagnetic gadolinium ions (Gd^{3+}) are widely used to construct T_1 CAs and exhibit high T_1 contrast through effective interacting with adjacent water protons. Compared to IONP, ultrasmall Gd_2O_3 nanoparticles and Gd_2O_3 nanoplate have been proved to exhibit more effectively T_1 contrast with lower r_2/r_1 ratio due to the low magnetic susceptibility. These results inspire researchers to embed Gd_2O_3 nanocluster into IONP and investigate their T_1 contrast [219]. Small sized gadolinium-embedded IONP (GdIONP) have been reported to show high T_1 relaxivity, due to the spin-canting effects and introduction of Gd species [220]. GdIONP with the size of 4.8 nm showes T_1 relaxivity with the value of 7.85 $mM^{-1}s^{-1}$ and r_2/r_1 ratio of 5.24 at 7 T. Gao and co-authors further engineered IO nanoplate with metal-rich exposed crystal surface by Gd ions to optimize its T_1 relaxivity (Fig. 11h-l) [221]. Based on the synergistic effects of exposed metal-rich Fe_3O_4 (100) facet and embedded Gd_2O_3 clusters, this engineered IO nanoplate show an ultrahigh T_1 relaxivity with the value of 61.5 $mM^{-1}s^{-1}$ and r_2/r_1 ratio of 2.4 at 0.5 T. The enhanced T_1 relaxivity could be ascribed to two main reasons, those are exposed Fe and Gd ions and terminated Fe_3O_4 (100) basal plane. The exposed Fe and Gd ions could provide sufficient paramagnetic island and result in synergistic enhancement. In addition, the flatten surface is beneficial to the hoping of water proton on the surface of Gd engineered IO nanoplate and further improve the chemical exchange efficiency. It should be noted that its T_1 relaxivity is highly dependent on the amount of Gd ions. r_1 values increased from 46.7 ± 2.0 to 66.3 ± 3.1 $mM^{-1}s^{-1}$ with the rising of Gd percentage from 11% to 26%. We speculate that this result may be a consequence of increased τ_s caused by the increase amount of Gd ions.

3.4.3. Copper

Copper ions with the τ_s value of $\sim 10^{-9}$ have been reported to be a candidate T_1 MRI CA in the form of CuO and CuS nanoparticles [223–226]. In addition, the magnetization moment of copper based nanoparticles are significantly lower than that of IONP. Thus, engineering IONP by copper ions may improve its τ_s and reduce its magnetization moment, which may improve the T_1 relaxivity of IONP. One attempt have been carried out to improve the T_1 relaxivity of IONP by copper dopant (Fig. 11m-q) [222]. Herranz and co-author developed a copper doped extremely small IONP (CuIONP). When the dopant percentage of copper is 4%, CuIONP exhibits high T_1 relaxivity with the r_1 value and r_2/r_1 ratio of 15.7 $mM^{-1}s^{-1}$ and 2.1. The relative high r_1 value and low r_2/r_1 ratio endow these engineered IONP with good T_1 contrast to achieve MRI based angiography and tumor imaging.

3.5. Chemical exchange

T_1 relaxivity of MRI CA is dependent on the chemical exchange efficiency between CAs and water protons at the interface. Surface ligand of CA could affect water diffusion, retention, and interaction with the magnetic centers, which determine τ_e, τ_R, τ_m, and the chemical exchange efficiency between IONP and water proton. A deep investigation of the effect of surface ligand on the T_1 relaxivity of IONP can provide guidance in improving its T_1 contrast.

3.5.1. Molecular weight

r_1 value of IONP is mainly determined by the exchange rate of water proton in its inner sphere. Theoretically, IONP stabilized by low molecular weight (M_w) ligand would reduce the hydrodynamic volume, resulting in the accessibility reduction of water proton to the surface of IONP. Therefore, altering the M_w or chain length of the surface coating ligand seem to be the simplest way to adjust T_1 relaxivity of IONP. In previous study, the relationship between M_w of polyethylene glycol (PEG) and T_1 relaxivity have been investigated (Fig. 12a) [41]. It seems that r_1 value increases with the rising of M_w of PEG. IONP coated by PEG with the M_w of 1000, 2000, 5000 Da show higher r_1 values than that with M_w of 550 and 750 Da. This M_w related T_1 relaxivity also been reported in other research. Tromsdorf et al. found that r_1 value of PEG coated IONP gradually increases with rising of M_w from 350 to 1100 Da, but decreases when M_w increases to 2000 Da [199]. The r_1 value decreasing at 2000 Da may be attributed to the aggregation of IONP.

3.5.2. Hydrophilicity

Hydrophilicity increasing of surface area benefits the water access to the surface of IONP and elevates the chemical exchange efficiency. Bao et al. crosslinked tannic-acid coated IONP onto bovine serum albumin to form nanocluster [227]. The relaxivity measurement indicates that r_1 value of nanocluster is about 2 times higher than that of free nanoparticles. This r_1 value elevation could be ascribed to the high hydrophilicity around IONP and reduced mobility within the nanoclusters. In another research, Seo and co-authors modified Eu doped IONP (EuIONP) with citrate (Cit), alendronate (Ale), and PMAO/PEG (PP), which showed different hydrophilic (Fig. 12b–f) [228]. The hydrophobicity of all samples were measured by the contact angle. The contact angles of Cit, Ale, and PP are immeasurable, 9.8°, and 112.4°, which means the hydrophobicity order is Cit < Ale « PP. This result is highly consistent with the changing of T_1 relaxivity with the order of EuIONP-Cit > EuIONP-Ale » EuIONP-PP.

3.5.3. Electronic and magnetic interactions

It is well known that graphene oxide (GO) could interact with semiconducting oxide nanoparticles through excited-state electron transfer. The charge-transfer between electronic and magnetic interactions have been reported to existence between IONP and GO [229–231]. This unique phenomenon may affect the chemical exchange interaction between GO coated IONP and surrounding water proton. Recently, the effect of GO on the T_1 relaxivity of IONP have been investigated (Fig. 12g–i) [232]. T_1 relaxivity assessment indicate that GO coated IONP show T_1 relaxivity with the value of 2.82 $mM^{-1}s^{-1}$, which is about 6 times higher than that of free IONP with the r_1 value of 0.46 $mM^{-1}s^{-1}$. The enhancement on T_1 relaxivity of IONP is believed to contribute to two mainly reasons. One is the energy exchange and charge transfer between GO and IONP, the other is the homogeneous dispersion of IONP. Notably, this research indicates that T_2 relaxivity of IONP could be suppressed by coating of GO, which could be ascribed to the limitation effect of GO on the spin of proton and local magnetic field. The decreasing effect on T_2 relaxivity could reduce r_2/r_1 ratio, further improving the availability of GO coated IONP as T_1 CA.

4. IONP based dual-modal imaging

Traditional strategies to achieve sensitive MRI contrast imaging by IONP is increasing its T_1 or T_2 relaxivity, which could improve the signal difference between normal tissue and lesion. Although T_1 image shows high tissue resolution and T_2 image exhibits high feasibility of detection under the assistant of single modal CA, such single mode CA are not yet perfect and facing huge challenges in accurate imaging of tiny lesion. To improve the sensitivity and accuracy, simultaneous acquisitions of T_1 and T_2 CA have attract considerable interest. Combination of T_1 and T_2 modal can provide complementary information for doctor to differentiate lesion from normal tissue with improved sensitivity and accuracy. In recent ten years, a number of IONP based T_1/T_2 dual-modal MRI CAs have been developed [52,57,233–238]. Besides to develop IONP with MRI based dual-modal contrast, direct conjugation secondary even tertiary imaging moiety with IONP is another effective method to improve its contrast efficiency. Currently, there are several representative imaging modalities have been used in clinical or preclinical research,

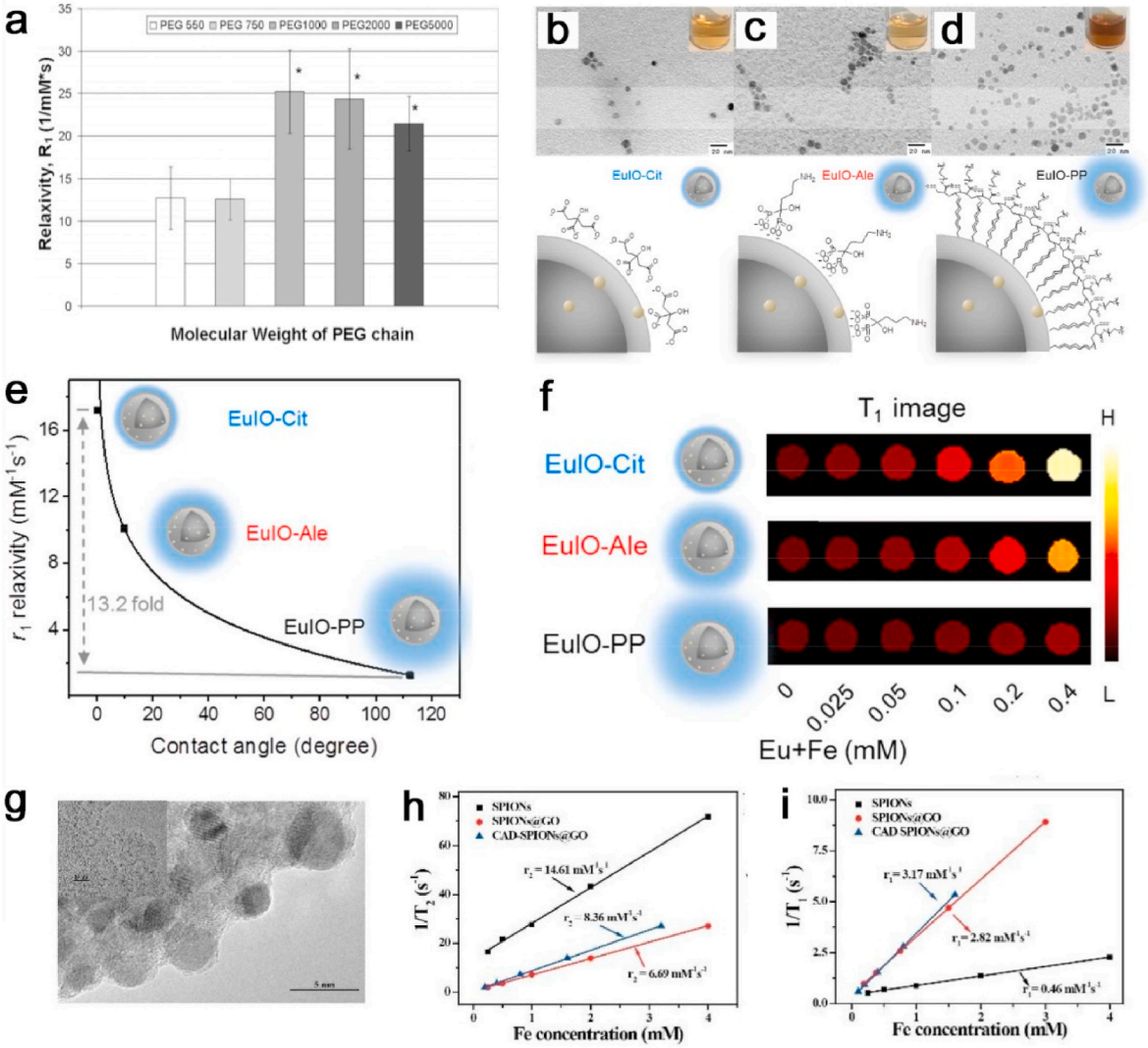

Fig. 12. Effect of chemical exchange efficiency on T_1 relaxivity of IONP. (a) r_1 values of IONP coated by DSPE-PEG with different molecular weights. Reproduced with permission [41]. Copyright 2007, John Wiley & Sons, Inc. TEM images and schematic cartoon of EuIONP with surface ligand of (b) citrate (Cit), (c) alendronate (Ale), and (d) PMAO-PEG (PP). (e) r_1 relaxivities of EuIONPs coated with different surface ligands as a function of contact angle. (f) T_1-weighted images of EuIONPs coated with Cit, Ale, and PP with different magnetic ions concentration. Reproduced with permission [228]. Copyright 2018, American Chemical Society. (g) TEM images of IONP coated by GO. (h) Linear fitting of $1/T_2$ and (i) $1/T_1$ of the reference IONP, IOPNs coated by GO, and IONP coated by NH_2-cis-aconitic acid-DOX and GO. Reproduced with permission [232]. Copyright 2019, The Royal Society of Chemistry.

including MRI, SPECT, PET, CT, FL imaging, US imaging, and PA imaging. Introducing of these imaging modality to IONP can effectively overcome the instrumental limitation of MRI and increase its sensitivity to satisfy the requirement of accurate imaging. In the following section, we will focus on introducing recent method to fabricate IONP with dual-modality contrast to improve its diagnosis efficiency.

4.1. T_1-T_2 dual-modality

For the purpose of dual-modal enhancement, the straightforward method to construct IONP based T_1/T_2 dual-modal CA is introducing T_1 contrast domain into IONP. Since the direct chemical exchange to water proton is the basis of T_1 contrast imaging, this strategy often adopts as the T_1 contrast domain exposed on the outer shell [56,239–241]. Im et al. synthesized MnO coated IONP with core-shell, dumbbell-like, and flower structure and assessed their capacity on simultaneous enhancement on both T_1 and T_2 modal (Fig. 13a–d) [242]. The r_1 values and r_2/r_1 ratios of Fe_3O_4@MnO, Fe_3O_4/MnO dumbbell, and Fe_3O_4/MnO flower are 1.3, 1.4, and 0.6 $mM^{-1}s^{-1}$ and 28, 56, and 235, which are not suit o applied as the T_1/T_2 dual-modal CAs to early and accurate diagnosis. The relatively high r_2/r_1 ratio of this kind of core-shell structure have been found in IONP coated by Gd_2O_3 shell as well (Fig. 13e–h) [243]. Sun et al. constructed a yolk-like nanostructure using IONP as core and mesoporous Gd_2O_3 layer as shell. The r_2/r_1 ratio of this nanostructure is about 48.9, which is significantly higher than that of typical T_1/T_2 dual-modal CA. These results could be ascribed to the fact that IONP could slow the T_1 spin fluctuation, which is ineffective for water proton relaxation and leads to a low T_1 MRI signal. Cheon and co-worker discovered that the speed of electron spin fluctuation of T_1 contrast domain is determined by the distance between T_1 and T_2 contrast domains (Fig. 13i-n) [58]. When the distance of the T_1 and T_2 domains is above a certain value, the electron spin fluctuation of T_1 domain accelerate water proton relaxation and result in a stronger T_1 MRI signal. Thus, tuning the distance between T_1 domain and IONP have been adopted to construct effective T_1/T_2 dual-modal CAs [244]. Cheon and co-workers utilized SiO_2 as the isolation layer to separate T_2 domain ($MnFe_2O_4$ nanoparticles) and T_1 domain ($Gd_2O(CO_3)_2$ shell) (Fig. 14a–c) [245]. Along with the thickness increase of SiO_2 layer in the

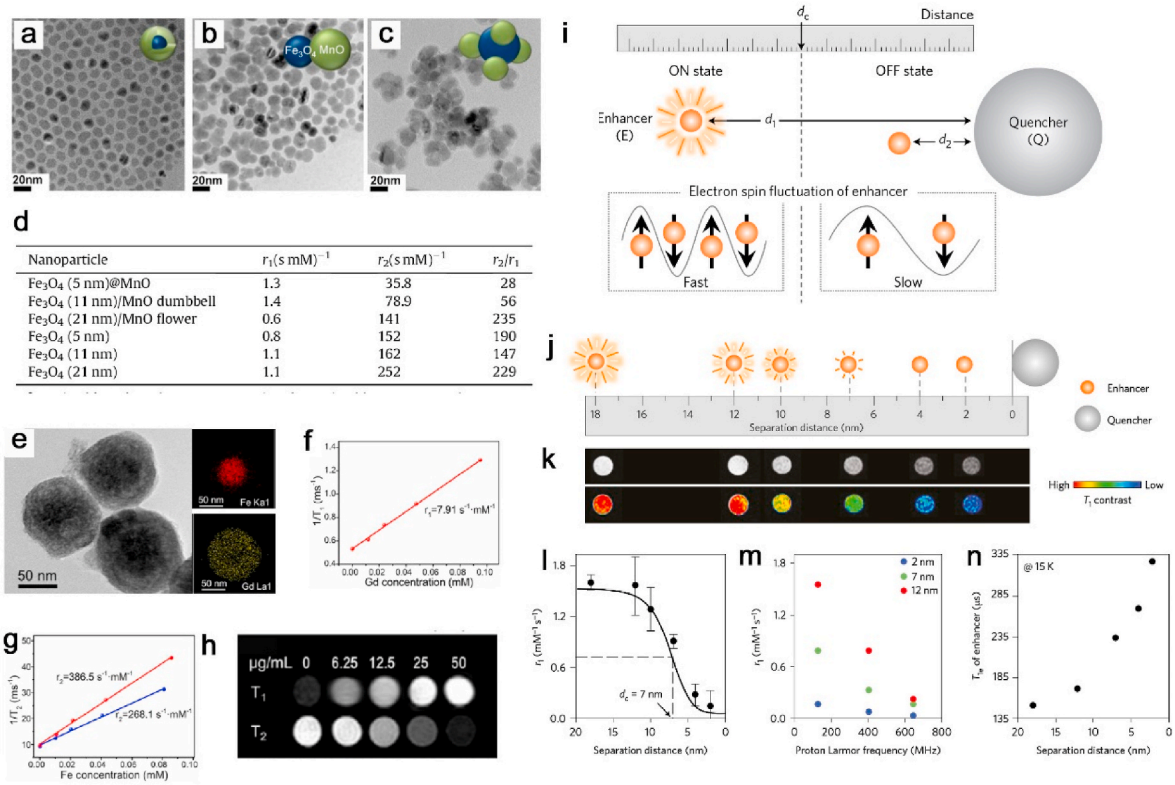

Fig. 13. Effect of direct coating IONP with T_1 contrast moiety on its T_2/T_1 dual-modality contrast capacity. TEM images of (a) Fe_3O_4, (b) Fe_3O_4@MnO, (c) Fe_3O_4/MnO dumbbell nanoparticles, respectively. (d) Comparison of r_1 values, r_2 values, and r_2/r_1 ratios of different nanoparticles. Reproduced with permission [242]. Copyright 2013, Elsevier Ltd. (e) TEM and EDX mapping images of Gd_2O_3 coated IONP. (f) r_1 and (g) r_2 value of Gd_2O_3 coated IONP. (h) T_1-and T_2-weighted MR images obtained from Gd_2O_3 coated IONP at varied concentrations. Reproduced with permission [243]. Copyright 2017, American Chemical Society. (i) Schematic cartoon illustrates the distance dependent magnetic resonance tuning. (j) A schematic representation of the nanoscale ruler based on the MRET effect. (k) T_1-weighted and color mapped MR images of solution containing enhancer and quencher with varied distances. (l) A plot of r_1 values versus separation distance. (m) The r_1 values of the enhancer with a separation distance of 2, 7, and 12 nm at various larmor frequencies. (n) A plot of T_{1e} versus the separation distance at 15 K. Reproduced with permission [58]. Copyright 2017, Nature Publishing Group. (For interpretation of the references to color in this figure legend, the reader is referred to the Web version of this article.)

order 4, 8, 12, 16, and 20 nm, the r_1 value changes in the order 2.0, 4.0, 25.1, 33.1, and 32.5 mM^{-1}s^{-1}. On contrary, T_2 relaxivity decreases with the increasing of separating layer due to reduction effect on local magnetic field caused by SiO_2 layer. These results endow this core-shell nanostructure as a potential T_1/T_2 dual-modal CA. The generality of introduction of SiO_2 isolating layer to separate T_1 domain and T_2 domain have been demonstrated by the same group [60]. Various T_2 domains, such as Fe_3O_4 and $CoFe_2O_4$, and T_1 domains, including $Eu_2O(CO_3)_2$, $Dy_2O(CO_3)_2$, and [ImH][Mn(BTC)(H_2O)] have been combined to construct artifact filtering imaging agent (AFIA). All of the AFIAs exhibit simultaneous remarkable T_1 and T_2 signal enhancement. Except to SiO_2, polydopamine have been discovered to be another isolation shell to construct IONP based T_1/T_2 dual-modal CAs [233]. Another structure to regulate the distance between T_1 domain and IONP is Janus structure. Cheng et al. synthesized dumbbell hybrid nanotrimers and utilized Pt nanocube to isolate Gd chelators attached Au nanoparticles and IONP (Fig. 14d–f) [236]. The linking distance between Au and IONP have been accurately regulated with the value of 5.4, 9.6, 10.7, and 12.9 nm. Consistent with the previous study, the dumbbell nanotrimer shows increased T_1 relaxivity with the rising of distance between Au and IONP due to the reduced magnetic coupling between Gd and IONP. Based on their proper distance, dumbbell nanotrimers with the linking distance of 10.7 and 12.9 show obvious simultaneous T_1 and T_2 signal enhancement effect. Altering the structure of IONP have been proved to be effective strategy to adjust the contrast of IONP in T_1 and T_2 modal. The critical parameter, which determine a given IONP is T_1 or T_2 dominated MRI CA, is its r_2/r_1 ratio. Previous study indicate that engineering the structure of IONP, especially morphology, could increase its T_1 relaxivity and reduce its T_2 relaxivity, which endow it with favorable r_2/r_1 ratio to exhibit T_1/T_2 dual-modal contrast.

Recently, The T_1 and T_2 contrast ability of IO nanoplate with the thickness of 4.8 nm have been investigated [155]. Its exposed Fe_3O_4(111) facet provided sufficient iron ions to achieve chemical exchange to water proton, which increased its T_1 contrast ability. Besides, the thin thickness improved the spin canting effect and reduce its magnetization and T_2 contrast ability. Due to the lowering T_2 contribution and enhancing T_1 contribution, IO nanoplate with the thickness of 4.8 nm show significant signal enhancement in both T_1 and T_2 contrast imaging. This morphology dependent typical T_1 and T_2 dual-modal contrast have also been found in IONP with other morphology, such as nanocube [212].

In addition, dopant of paramagnetic ions, especially gadolinium ions into the crystal structure of IONP have been proved to be another effective method to construct IONP based T_1/T_2 dual-modal CA. Gao and co-authors embedded gadolinium cluster into IONP, which lead to a synergistic enhancement on T_1 and T_2 relaxivity of IONP (Fig. 15) [246]. The r_1 value of gadolinium doped IONP (GdIONP) is ~69.5 mM^{-1}s^{-1} in terms of Gd; and the r_2 value of GdIONP is about 146.5 mM^{-1}s^{-1} in terms of Fe. Due to the dopant of gadolinium ions, the r_1 and r_2 values of GdIONP are both higher than Gd_2O_3 and IONP and show obvious signal enhancement in both T_1 and T_2 modal. Dopant other paramagnetic ions into IONP, such as manganese and europium, have been proved to achieve enhancement of T_1 and T_2 signal as well [213,234]. Xiao et al., have synthesized DSPE-PEG coated MnIONP as T_1/T_2 dual-modal CA

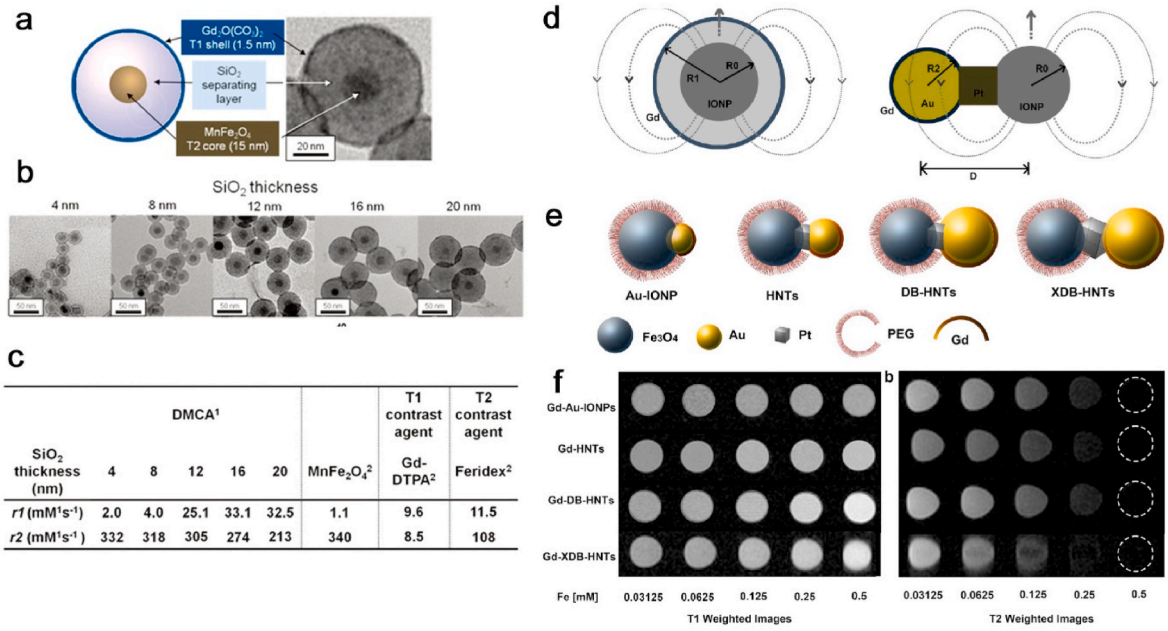

c

SiO_2 thickness (nm)	DMCA[1] 4	8	12	16	20	$MnFe_2O_4$[2]	T1 contrast agent Gd-DTPA[2]	T2 contrast agent Feridex[2]
r1 ($mM^{-1}s^{-1}$)	2.0	4.0	25.1	33.1	32.5	1.1	9.6	11.5
r2 ($mM^{-1}s^{-1}$)	332	318	305	274	213	340	8.5	108

Fig. 14. IONP based core-shell T_1/T_2 dual-modal CA. (a) Schematic and TEM image of core-shell type dual-modal CA. (b) TEM images of dual-modal CAs with different separating layer thickness. (c) r_1 and r_2 values of dual-modal CAs, $MnFe_2O_4$, Gd-DTPA, and Feridex. Reproduced with permission [245]. Copyright 2010, American Chemical Society. (d) Schematic illustrate the magnetic coupling of T_1 and T_2 CAs in core-shell and dumbbell structures. (e) Illustration of constructions of four different types of dumbbell-like or dumbbell heterostructures. (f) T_1-and T_2-weighted MRI images of dumbbell hybrid heterostructures. Reproduced with permission [236]. Copyright 2014, American Chemical Society.

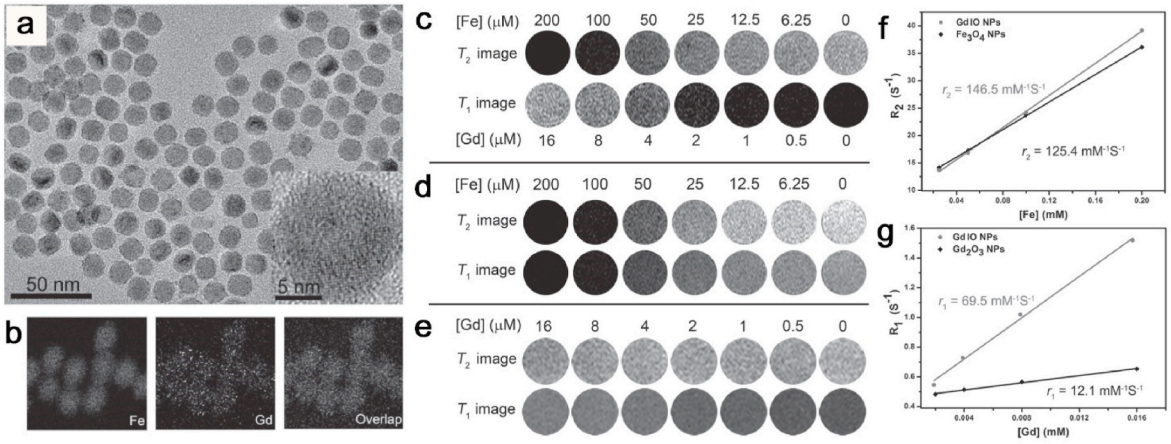

Fig. 15. IONP based T_1/T_2 dual-modal CA. (a) TEM and (b) EDX mapping images of GdIONP. T_1-and T_2-weighted MR images of (c) GdIONP, (d) IONP, and (e) Gd_2O_3 nanoparticles, respectively. The analyses of (f) T_2 and (g) T_1 relaxation rate of GdIONP, IONP, and Gd_2O_3 nanoparticles. Reproduced with permission [246]. Copyright 2012, John Wiley & Sons, Inc.

[247]. They found that MnIONP coated with DSPE-PEG with the mass ratio of 1:20 showed harmonious T_1 and T_2 relaxivity and could be considered as an excellent candidate as T_1/T_2 dual-modal CA.

4.2. MRI-FL modality

Fluorescence imaging with high sensitivity is the earliest modality to be introduced into IONP to ameliorate its contrast sensitivity. Initially, the fluorescence dye or quantum dots were directly conjugated with IONP to form the MRI-fluorescence dual-modality CAs [74,248–250]. Xu and co-authors used IONP as seeds to grow CdSe QDs on its surface and obtained hybrid IONP with magnetic and fluorescence property [251]. This hybrid IONP could successfully achieve fluorescence imaging on cellular level, while the existed energy transfer between the fluorescent domain and IONP result in a fluorescence quenching and limit its application as a MRI-fluorescence dual-modality CA *in vivo*. Since this quench effect is highly dependent on the distance between the fluorescent domain and IONP, one can improve its fluorescent property by increasing this distance. Lee et al. attached IONP on dye-doped silica nanoparticles to form "core-satellite" nanostructure with MRI and fluorescence imaging capacity (Fig. 16a–f) [73]. The fluorescence signal of this core-satellite nanostructure is enhanced by 1.7 times compare to the directly dye conjugated IONP with the assistance of separating effect of silica, which reduces quenching effect between IONP and fluorescent dye. Moreover, the core-satellite nanostructure with assembled IONP show increased T_2 relaxivity with the r_2 value of 397 $mM^{-1}s^{-1}$. The perfect MRI and fluorescent contrast ability endow this nanostructure to conduct sensitive imaging of sub-millimeter cellular clusters.

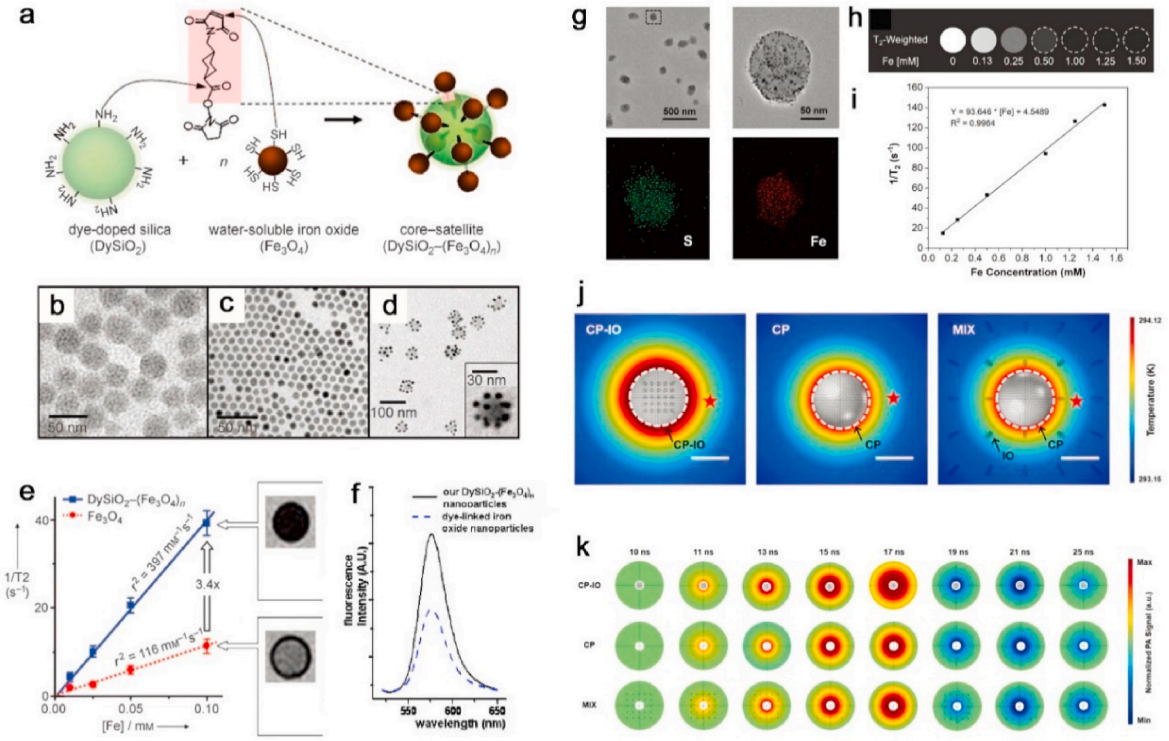

Fig. 16. IONP based MRI-FL and MRI-PA dual-modal CA. (a) Schematic diagram for the synthesis of $DySiO_2$-$(Fe_3O_4)_n$ nanoparticles. TEM images of (b) $DySiO_2$, (c) IONP, and (d) $DySiO_2$-$(Fe_3O_4)_n$ nanoparticles. (e) Analyses of T_2 relaxation rates and T_2-weighted MRI images of $DySiO_2$-$(Fe_3O_4)_n$ nanoparticles and free IONP. (f) Photoluminescence spectra of $DySiO_2$-$(Fe_3O_4)_n$ nanoparticles and dye linked IONP. Reproduced with permission [73]. Copyright 2006, John Wiley & Sons, Inc. (g) TEM and EDX mapping images of CP-IO nanocomposites. (h) T_2-weighted MR images and (i) T_2 relaxation rate analyses of CP-IO nanocomposites. (j) Plots of the simulated temperature distribution in CP-IO, CP, and MIX nanoparticles at 100 ns. (k) Plots of the simulated PA signal transmission from surface of nanoparticles to surrounding water environment. Reproduced with permission [79]. Copyright 2018, John Wiley & Sons, Inc.

4.3. MRI-PA modality

As a relatively new imaging technique, PA imaging exhibits high spatial resolution and fast real-time scan. Over the past decades, there are numerous materials, including gold [69,252–254], indocyanine green (ICG) [78,255], polypyrrole (PPy) [80], and diketopyrrolopyrrole (DPP) [79], have been applied to incorporating the advantages of PA and MRI into a single nanostructures. Thawani et al. combined ICG and IONP to develop a stable nano-cluster [78]. The as-prepared nanostructure exhibited obvious enhancement effect on both MRI-PA imaging and realized effective MRI-PA assistant tumor detection on mice model. Interestingly, IONP was discovered to increase the signal of traditional PA imaging CA. Recently, Liu and co-workers integrated DPP-based conjugated polymer (CP) and IONP into close proximity by amphiphilic polymer to fabricate MRI-PA dual-modal CA (Fig. 16g–k) [79]. With the maintained T_2 relaxivity of IONP, the obtained product can produce remarkable enhanced PA signal. A 45% PA signal intensity amplification is observed in the obtained nanocomposites compare to the bare CP due to the addition of IONP, which boosts the heat generation and heat dissipation pathways in the production of PA signal.

4.4. MRI-PET/SPECT dual-modality

PET or SPECT, those signal is generated by gamma-rays emitted from decaying radioisotopes (e.g. ^{64}Cu and ^{124}I for PET and ^{99m}Tc and ^{131}I for SPECT), show high sensitivity but relatively poor spatial resolution. Combination of PET or SPECT with MRI have been proved to improve the contrast imaging efficiency of IONP [256–258]. ^{124}I have been successfully linked on MnIONP through chemical conjugation (Fig. 17a–c) [259]. The resultant hybrid CA maintain equivalent contrast effect corresponding to the CA of single MRI and PET modality. This unique feature endow this dual-modality CA with high spatial resolution and high sensitivity to perform lymph node imaging. On the assistant of a fused MRI-PET image, researchers can easily differentiate the tiny brachial lymph from axillary lymph node with the diameter of a few millimeters. Meanwhile, many attempts have been conducted to fabricate IONP based MRI-SPECT dual-modality CAs. IONP radiolabeled with ^{99m}Tc is reported as a MRI-SPECT CA (Fig. 17d–h) [66]. The ^{99m}Tc labeled IONP with retained *in vivo* MRI contrast property shows SPECT contrast imaging. Coupled with excellent stability, this CA provides sufficient signal to successfully achieve liver and spleen imaging on mice model. On the basis of long half-life, ^{125}I have been investigated as the SPECT imaging moiety to construct IONP based MRI/SPECT dual-modal CAs.

4.5. MRI-CT modality

Considering CT is advantageous in regard to its high resolution and ease of forming 3D visual reconstruction of tissue of interest, introducing CT contrast moiety onto IONP have been used to improve its imaging efficiency [260–263]. The common strategy is synthesis of Au nanomaterials hybrided IONP. Zhao et al. successfully synthesized strawberry-like Fe_3O_4–Au hybrid nanoparticle with enhanced X-ray attenuation and magnetic properties as an accurate MRI-CT dual-modal CA to distinguish the grade of live disease (Fig. 18a–e) [264]. Except to Au, the possibility of fabrication IONP based MRI-CT dual-modal CAs with other CT contrast moiety have been investigated as well. Multifunctional Fe_3O_4/TaO_x core/shell nanoparticle have been synthesized by Hyeon and co-workers (Fig. 18f–i) [265]. On the basis of its low cost and high biocompatibility, TaO_x is more promising as the CT contrast moiety to construct MRI-CT dual-modal CA compared to Au nanostructure. Fe_3O_4/TaO_x core/shell nanostructure exhibites remarkable

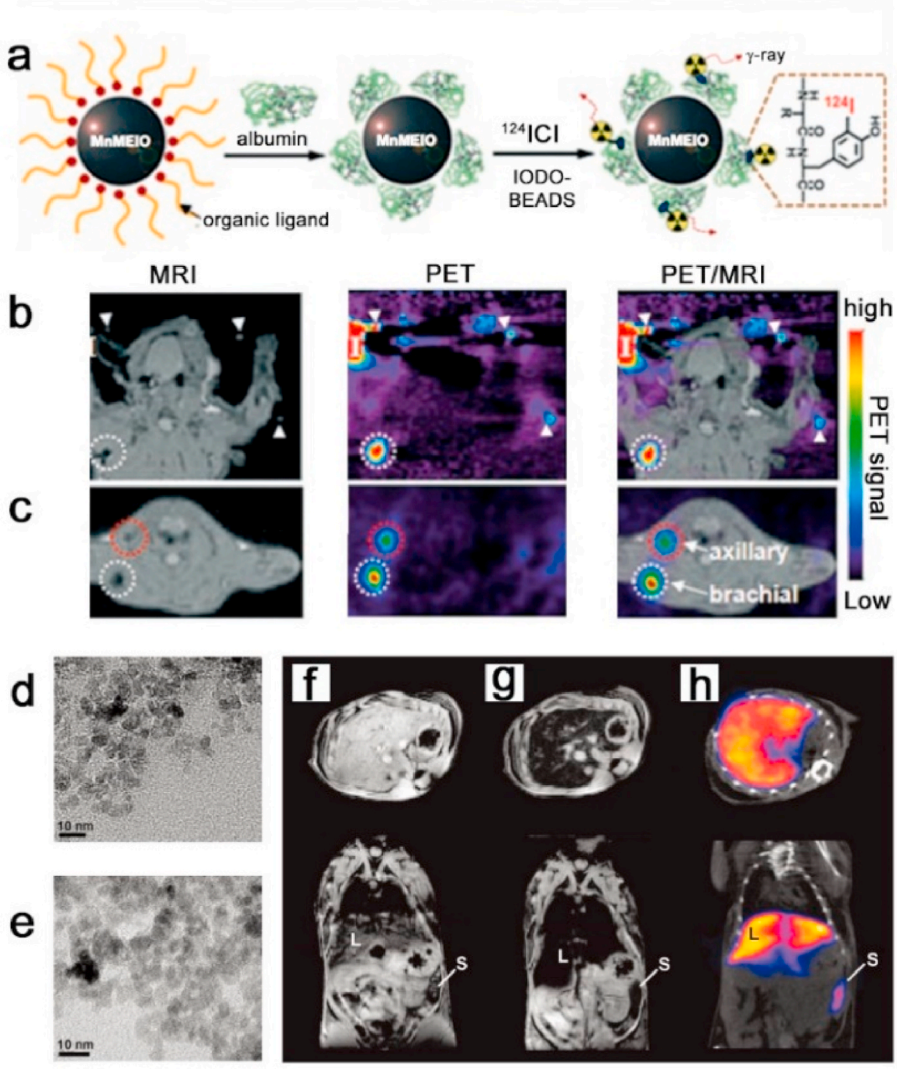

Fig. 17. IONP based MRI-PET/SPECT dual-modal CAs. (a) Illustration of preparation of ^{124}I linked MnIONP. PET/MRI images of SLNs in a rat at 1 h post injection of ^{124}I linked MnIONP into the right forepaw in (b) coronal and (c) transverse view. Reproduced with permission [259]. Copyright 2008, John Wiley & Sons, Inc. TEM images of (d) IONP and (e) ^{99m}Tc radiolabeled IONP. T_2-weighted MRI images (f) before and (g) 15 min postinjection of ^{99m}Tc radiolabeled IONP. (h) SPECT-CT image of the same mice in a similar view 45 min postinjection. Reproduced with permission [66]. Copyright 2011, American Chemical Society.

enhancement effect in both X-ray CT and MRI phantom images, which make it as an effective MRI-CT dual-modal CA in the detection of newly formed blood vessels of and microenvironment of tumor.

5. IONP based responsive MRI CAs

The basis of MRI CA based disease diagnosis is the signal difference caused by the different accumulation amount of CA in lesion and surrounding tissue. Although surface modification could optimize the *in vivo* behavior of CA and improve their accumulation in lesion, the misaccumulation in normal tissue could not be avoided Besides, the traditional CAs are "always on" systems that generate MR signal enhancement regardless of their location, which may result in poor target to background signal difference. Recently, responsive MRI CA have been designed to respond to specific changes in the surrounding physiological microenvironments and specific physical conditions [94,266–270]. Compared to the traditional MRI CA with fixed contrast capacity in both normal and lesion tissue, responsive MRI CAs are designed to switch "on" and "off" T_1 or T_2 signal change in response to a specific stimulus of lesion. Generally, responsive MRI CA could be divided into three types, those are active, recovery, and switchable. Discussion on the recent development of strategy to construct IONP based responsive MRI CA to assist doctors to achieve accurate and early lesion diagnosis is urgent and meaningful.

5.1. Active

Compared to single IONP, assembled architecture shows remarkably increased T_2 contrast ability. Modifying nanoparticles with specific molecular have been proved to be an effective strategy to implement their self-assembly under stimuli [271]. This unique phenomenon provided opportunity for IONP to complete the conversion from single state to assembled state and achieve T_2 active MRI imaging. Jasanoff and Co-worker engineered IONP with fused C2 domains of synaptotagmin 1 (C2AB), which could naturally respond to the concentration change of Ca^{2+} (Fig. 19a–e) [272]. Based on the two binding sites for Ca^{2+} in C2AB, this IONP could aggregate in the presence of Ca^{2+} and promote its T_2 contrast. Along with the increasing of Ca^{2+} concentration from 0 to 1.2 mM, the r_2 value elevates from 151 to 261 $mM^{-1}s^{-1}$. Base on the calcium-dependent r_2 change, this nanomaterial could be considered as a potential CA to monitor the dynamic change of Ca^{2+} concentration in brain. Additionally, IONP based nanostructure have been reported to respond to matrix metalloproteinase (MMP) enzymes. In this work, IONP bearing complementary azide and alkyne click moieties are individually prepared [273]. To achieve MMP response, a MMP responded peptide was conjugated on the surface of IONP to block the activity click reaction. *In vitro* study indicates that the two individual IONP successfully forms nanocluster at the present of MMP and result in a 160% increase in T_2 activity. Recently, a cancer biomarker, glutathione (GSH), responsive IONP based active probe was developed (Fig. 19f–h) [274].

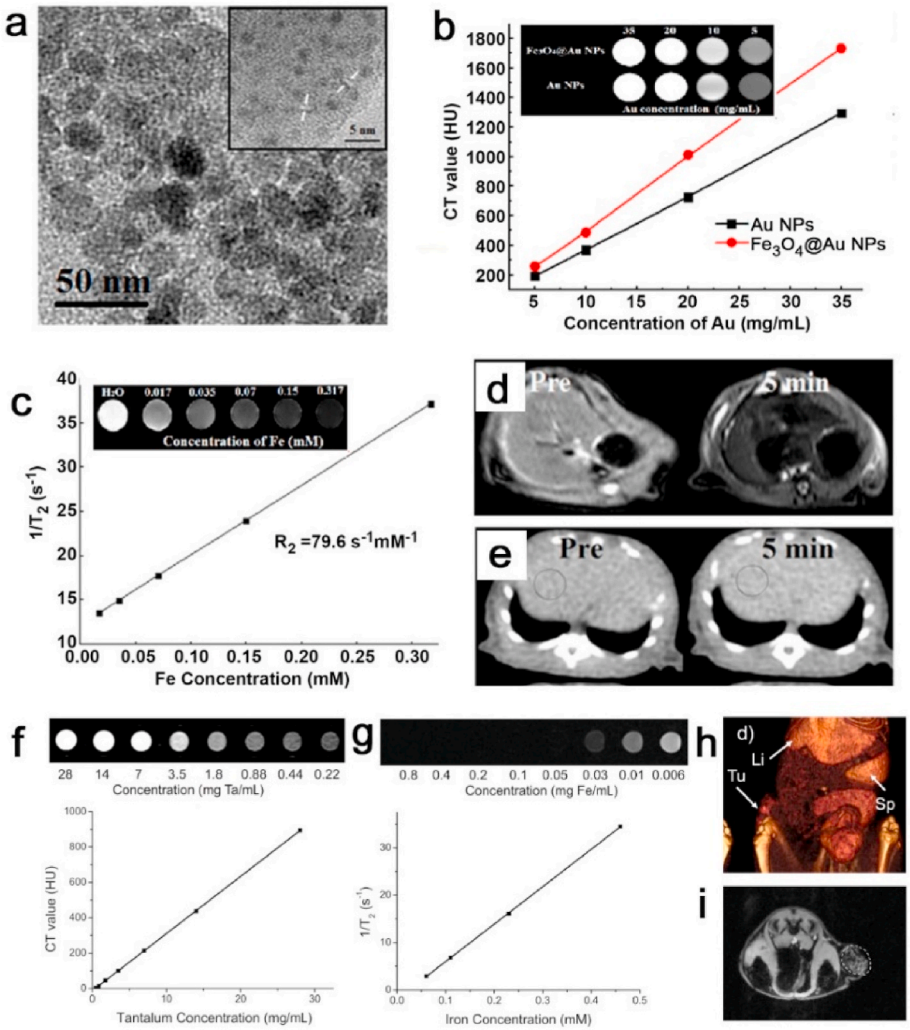

Fig. 18. IONP based MRI-CT dual-modal CAs. (a) TEM images of Fe_3O_4–Au hybrid nanoparticles. (b) X-ray attenuation assay and (c) T_2 ralaxation rate analysis of Fe_3O_4–Au hybrid nanoparticles. (d) T_2-weighted MRI and (e) CT images of rat pre and post injection in transversal view. Reproduced with permission [264]. Copyright 2015, Elsevier Ltd. (f) CT phantom images and HU values of Fe_3O_4/TaO_x nanoparticles. (g) T_2-weighted MRI images and r_2 values of Fe_3O_4/TaO_x nanoparticles. *In vivo* (h) CT image and (i) T_2-weighted image of rat 24 h after injection of Fe_3O_4/TaO_x nanoparticles. Reproduced with permission [265]. Copyright 2012, American Chemical Society.

With the existence of GSH, the disulfide bond on the surface of IONP is reduced, inducing the aggregate of IONP. The status conversion from single state to aggregation state results in the interlocked responses of both T_1 and T_2 signals and is utilized to quantitatively map the GSH within brain gliomas.

5.2. Recovery

As a typical T_2 CA, IONP have been proved to quench the T_1 relaxivity of Gd chelate [275]. It has been reported that conjugating Gd chelates on IONP with bio-response linker could achieve T_1 relaxivity recovery (Fig. 20a and b) [276]. In this study, the Gd chelate was conjugated on the silica coated IONP by MMP-2 responded peptides. To amplify the signal, dendrimers are introduced to increase the number of conjugated Gd chelate. MMP-2 successfully cleaves the peptide, resulting in release of Gd chelate from the local magnetic field generated by IONP and T_1 signal recovery. Based on the bio-response procedure, the detection limit of these systems to MMP-2 could be reduced to 0.5 nM achieving MMP sensing both at cellular level and xenograft tumors. T_2 relaxivity of IONP could be limited by a dense T_1 CAs shell as well. Introducing an environment responsive shell with T_1 contrast on the surface of IONP can initially shield its T_1 and T_2 relaxivity and achieve signal recovery under stimuli. Kim et al., developed a T_1/T_2 dual mode recovery imaging probe by coating IONP with redox-responsive paramagnetic Mn_3O_4 nano shell (Fig. 20c–g) [277]. Due to the strong silencing effect between Fe_3O_4 core and Mn_3O_4 shell, T_1 and T_2 contrast of this nanostructure are remarkably limited. Upon introduction to a tumor intracellular reducing environment, the Mn_3O_4 shell decomposed to release free Mn^{2+} ions. This structure alteration resulted in exposure of the interior Fe_3O_4 core to aqueous environment and recovery of T_1 and T_2 relaxivity.

5.3. Switchable

Recently, IONP based environment responsive MRI CA with modal switchable capacity have been developed to further increase the signal difference between lesion and normal tissue. There are two modal of switchable responsive MRI contrast imaging: T_2 contrast switch to T_1 contrast (mode I) and T_1 contrast switch to T_2 contrast (mode II). The strategy to develop mode I MRI CAs is construction IONP based nanocluster or nanoaggregation by responsive ligand. This kind of CA exist as nanocluster in blood circulation and normal tissue while collapse to dispersive nanoparticle, resulting in the T_2 contrast ability decrease and T_1 contrast capacity increase. On contrary, mode II CA is designed by in situ assemble of specific modified dispersive nanoparticles. Generally, ultrasmall IONP, typical with the size below 5 nm, have been considered as T_1 CAs. With specific surface modification, these nanoparticles form the nanoaggregation when it reach to the tumor tissue and can be readily enhance T_2 signal [88–90].

5.3.1. T_2/T_1 switchable

Lu et al. fabricated a pH-sensitive IO nanocluster through linking

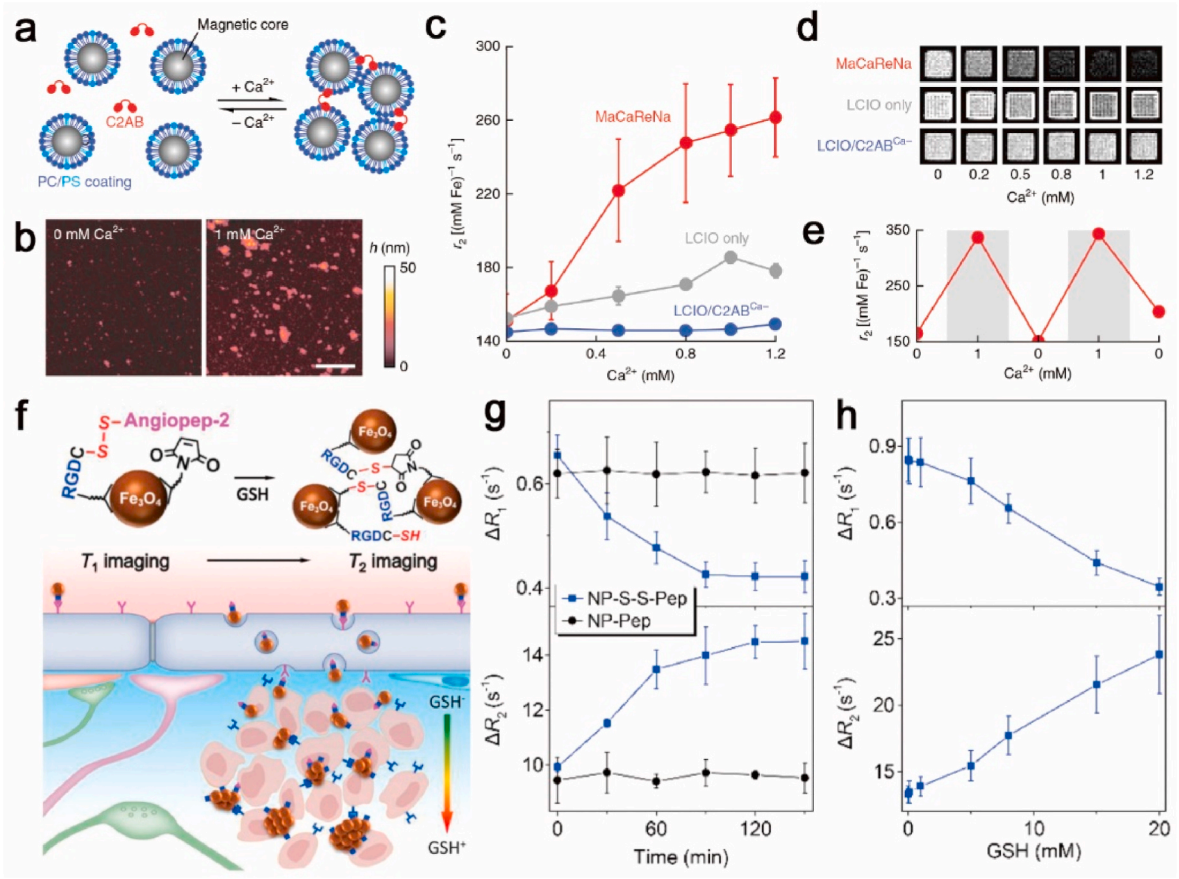

Fig. 19. IONP based intelligent CA with responsive signal active capacity. (a) Schematic cartoon illustrate the sensor design based on lipid coated IONP and C2AB. (b) AFM images of IONP based calcium-responsive nanostructure after exposure to 0 or 1 mM Ca^{2+}. (c) r_2 values and (d) T_2-weighted MRI images of IONP based calcium-responsive nanostructure after exposure to different Ca^{2+} concentrations. (e) r_2 changes observed in HEPES buffer over multiple cycles of calcium or EDTA addition. Reproduced with permission [272]. Copyright 2018, Nature Publishing Group. (f) Schematic drawings to show molecular mechanism of GSH-induced agglomeration of intelligent probe. (g) Temporal evolution of ΔR_1 and ΔR_2 for intelligent probe and peptide modified IONP during the incubation with GSH. (h) GSH concentration dependent ΔR_1 and ΔR_2 for intelligent probe and peptide modified IONP. Reproduced with permission [274]. Copyright 2021, John Wiley & Sons, Inc.

IONP with i-motif DNA-derived pH-responsive linkers (Fig. 21a–g) [278]. Along with the decrease of pH value from 7.4 to 5.5, the state of this nanocluster converts from assembly to disassembly, resulting in drastic decrease in T_2 relaxivity while increase in T_1 relaxivity. This pH dependent MRI contrast enable this nanocluster to successfully achieve T_2/T_1 switchable contrast imaging and detected tiny hepatocellular carcinoma. Besides to the pH-response T_2/T_1 switchable CAs, redox environment have been applied as another trigger to accomplish sensitive T_2/T_1 switchable MRI imaging [88]. Ultrasmall IONP were cross-linked into nanocluster through the S–S bond of Cys. On the basis of the fact that the reductive environment of tumor can rupture the S–S bond, this nanocluster would dissociated into single IONP at tumor site. The state conversion lead to this nanocluster change from T_2 dominate to T_1 dominate and undergo T_2/T_1 switchable MR imaging of tumor.

5.3.2. T_1/T_2 switchable

Compared to the nanocluster, ultrasmall IONP can easily extravasate from the tumor vasculature and diffuse into tumor tissue. Thus, IONP based switchable MRI CA show single state in delivery process and aggregation state at tumor have been investigated. Mao and co-authors discover that IONP with the size of 3.5 nm can effectively extravasate through tumor vessel and penetrates into tumor [90]. Based on the tight interstitial space, interstitial pressure, and acidic intratumoral environment, this ultrafine IONP could form cluster. The MRI investigation reveals that ultrafine IONP shows T_1 dominate contrast in the tumor vasculature and followed by emerging as T_2 CAs in tumor after injection.

To further increase the controllability of this clustering process and MRI contrast modal conversion, light sensitive T_1/T_2 switchable CA has been developed recently (Fig. 21h-l) [279]. Li et al. modified ultrasmall IONP with light-addressable unit DA via PEG spacer. The generated Fe_3O_4--PEG-DA shows high T_1 relaxivity with the value of 3.83 $mM^{-1}s^{-1}$ and could be used as a sensitive T_1 CA. Once laser irradiation with different duration time is applied, IO nanocluster with different aggregation degree can be formed. After 12 min irradiation, the size of IO cluster could reach 798.4 nm and result in the obviously increase of T_2 relaxivity (from 9.04 to 31.60 $mM^{-1}s^{-1}$) while reduction of T_1 relaxivity (from 3.83 to 1.61 $mM^{-1}s^{-1}$), showing a typical T_1/T_2 switchable process.

6. Optimization *in vivo* behavior of IONP

Apart from r_1 or r_2 value of MRI CA, the sensitivity and accuracy of MRI contrast imaging are also determined by the contrast efficiency of CA *in vivo*. Simply, the contrast efficiency of CA is dependent on the signal difference between normal tissue and lesion, which is most straightforward determined by the amount of CA in lesion. The surface ligand of IONP could affect its circulation behavior, accumulation amount in lesion, and uptake of tumor cells [96], thus IONP with optimized surface structure show perfect *in vivo* behavior and achieve high efficient contrast imaging.

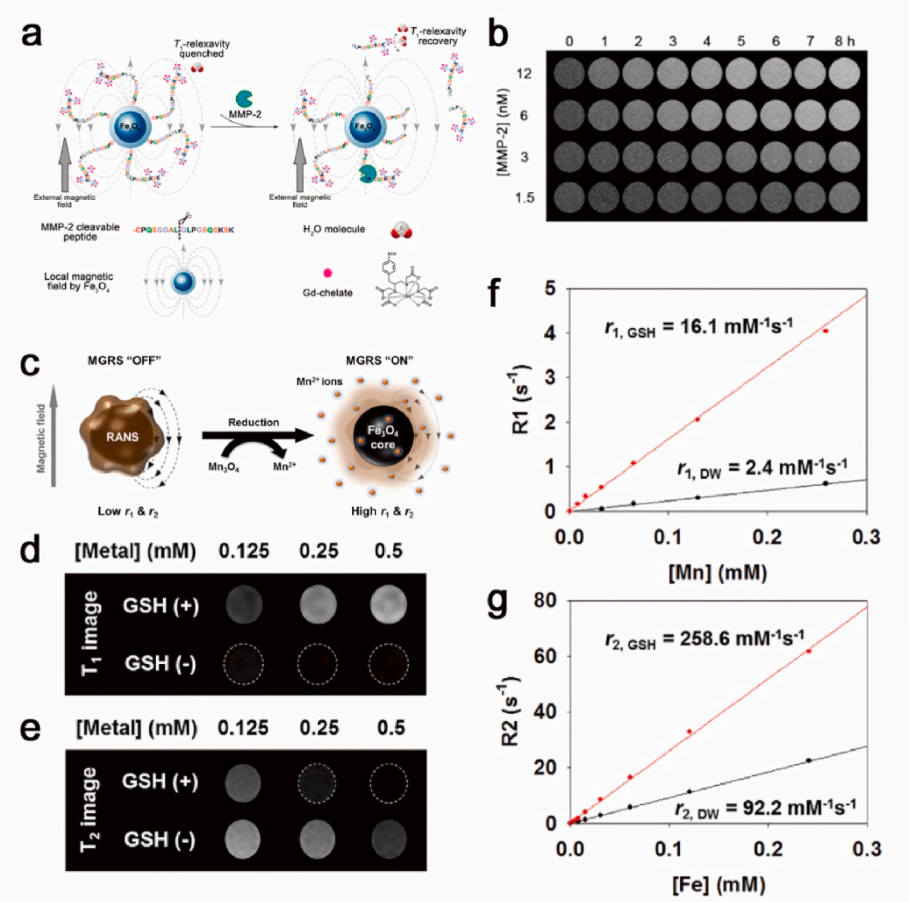

Fig. 20. IONP based intelligent CA with responsive signal recovery capacity. (a) Schematic illustration of MMP-2 detection using IONP based on T_1 relaxivity recovery. (b) T_1-weighted MRI images of IONP based T_1 recovery system incubated with MMP-2. Reproduced with permission [276]. Copyright 2017, American Chemical Society. (c) Schematic illustration of the redox-responsive activatable nanoshell. (d) T_1-and (e) T_2-weighted MRI images of responsive system after treatment of GSH and non-treatment. Relaxivity plot of (f) T_1 and (g) T_2 relaxation rate analyses. Reproduced with permission [277]. Copyright 2016, Elsevier Ltd.

6.1. Polymers

Polymers, including natural and synthetic polymer, functionalized IONP have drawn much attention due to the improvement on the structural stability, pharmacokinetics, and biodistribution of IONP.

6.1.1. Natural polymer

Natural polymeric ligands, such as polysaccharides and protein, commonly containing multiple active groups strongly binding with IONP for stability improvement in harsh biological environments. Dextran, a typical polysaccharide, has been extensively used for coating IONP with enhanced stability and functionality. The Dextran cross-linked IONP show negligible changes in size and morphology in the blood circulation [280]. Notably, the saccharides are natural signal molecular on the cell surface, modification IONP with polysaccharides exhibits targeting ability to some specific issue. Kamruzzaman et al. observed that lactobionic acid (LA) modified IONP showed the capacity to target hepatocytes [281]. The uptake amount of LA modified IONP is significantly higher than unmodified and maltotrionic acid modified IONP. Further *in vivo* targeting capacity analyses indicate LA modified IONP only result in the signal changes in liver cells, revealing its capacity to achieve specific imaging of liver. Recently, a great effort has been devoted to functionalization of IONP with proteins with improved stability, prolong circulation time, and targeted imaging. Protein coating have been proved to improve physical stability and reduce aggregation of IONP. Casein coated IONP remained stable for months without any aggregation or size change after incubation in medium containing serum [182]. Besides, Quan and co-worker discovered that coating IONP with HSA could reduce the efficiency of IONP removed by reticulo endothelial system (RES) and prolong its circulation time in blood [282]. The circulation half-life of IONP with HSA coating is about 87 min, which is significantly longer than that without HSA modification (3 min). Since antibody is a natural protein, coating IONP with protein can further achieve targeted imaging and improve diagnosis sensitivity. Chekhonin et al., synthesized monoclonal antibodies against VEGF (mAbVEGF) conjugated BSA-modified IONP and assessed its ability to achieve targeted tumor diagnosis [283]. It appears that this antibody modified IONP successfully enable visualization of glioma microvessels with sensitive detection of neoangiogenic areas after administration.

6.1.2. Synthetic polymer

To improve the stability of IONP, coating IONP with synthetic polymer, such as polyethylene glycol (PEG), poly(lactic-co-glycolic acid) (PLGA) and Polyvinylpyrrolidone (PVP) have got more and more attention. Among all synthetic polymers, PEG as a US FDA approved ligand is extensively used to modify IONP due to its advantage on decrease the adsorption of protein in serum and prolonging its circulation time in the body [99,284]. Weller and co-author investigated phagocytosis of PEG modified (PEGylated) IONP by J774 macrophages (Fig. 22a–d) [199]. They found that the uptake amount of PEGylated IONP was significantly lower than that of clinically used Resovist (commercial IONP based MRI CAs), revealing a obvious decrease of unspecific uptake into cells of RES and endowing IONP with long circulation time. In another study, PEG coated 3 nm IONP displayed lower toxicity but longer circulation time than clinically used GBCAs [46]. Additionally, these unique features endow PEGylated IONP with the ability to achieve dynamic time resolved MR angiography in rats. Because of its high stability, biodegradability, and biocompatibility, another synthetic polymer, PLGA, have been widely applied in construction IONP based MRI CA. Wang et al., developed IO loaded PLGA-mPEG nanoparticles as MRI CAs [285]. Due to their optimized

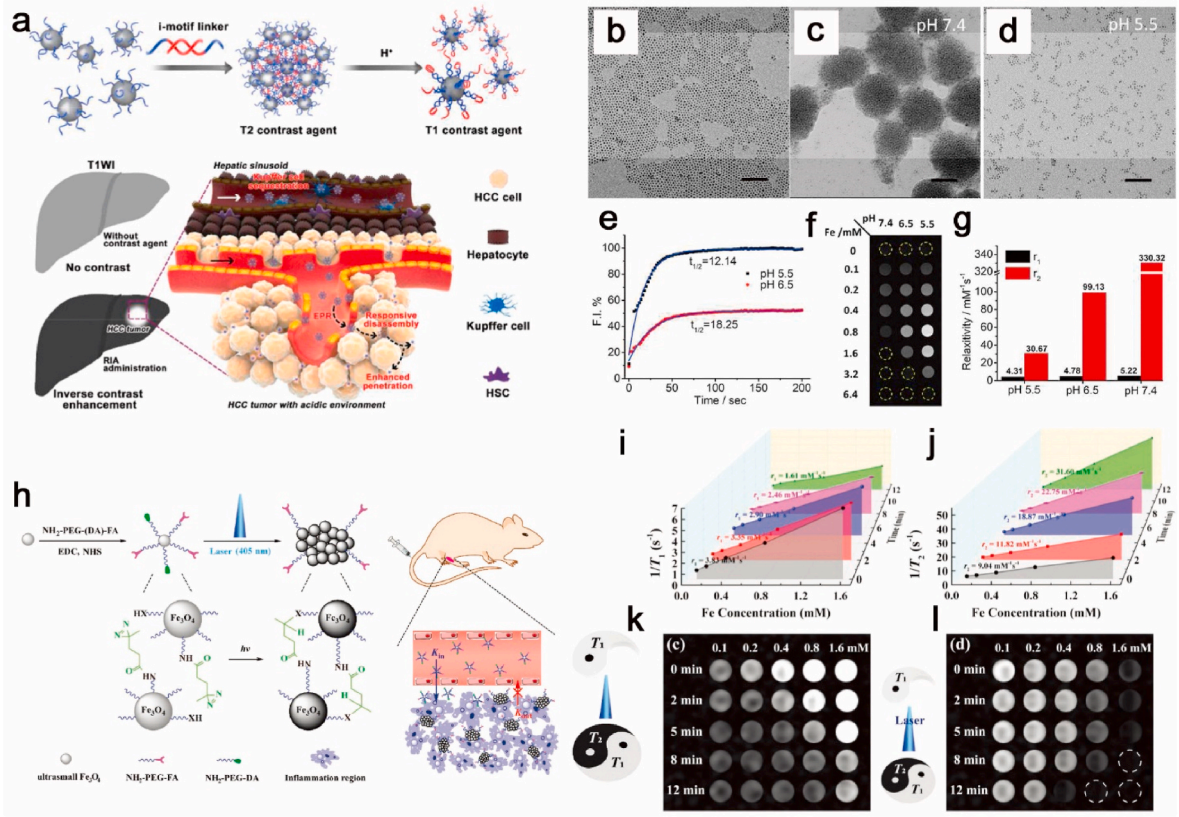

Fig. 21. IONP based modality switchable CA. (a) Schematic illustration of intelligent system based modality switchable diagnosis of HCC. TEM images of (b) small IONP, (c) intelligent system in PBS (pH 7.4), and (d) intelligent system in MES (pH 5.5). (e) Kinetic analysis of intelligent system disassembly upon the pH change from 7.4 to 6.5/5.5. (f) T_1-weighted images and (g) relaxivity of intelligent system in PBS (pH 7.4) and MES (pH 6.5 and 5.5). Reproduced with permission [278]. Copyright 2018, American Chemical Society. (h) Schematic illustration of the synthesis of IONP based intelligent system for enhanced retention and tunable T_1/T_2-weighted MR imaging of inflammatory arthritis. (i) T_1 relaxation rates, (j) T_2 relaxation rate, and (k) T_1-weighted, (l) T_2-weighted MR image of IONP based intelligent system under 405 nm laser irradiation (1.0 W cm^{-2}) for different time. Reproduced with permission [279]. Copyright 2019, John Wiley & Sons, Inc.

surface structure, this IO loaded PLGA-mPEG nanoparticle show higher contrast effect and longer half-life circulation time in comparison with Resovist. Modifying PLGA coated IONP with target motif can further improve contrast efficiency of IONP. Wang and co-workers functionalized PLGA-coated IONP by Arg-Gly-Asp (RGD) peptide [286]. Since RGD peptide has a tendency to bind activated platelets at the thrombus site, this MRI CA shows high affinity with thrombi and serves as a sensitive CA for early thrombi detection. Additionally, PVP attracted much interest in construction IONP based MRI CA because of non-toxicity, low cost, and antiviral properties. Chen and co-workers synthesized PVP coated IONP by a thermal decomposition method [287]. The PVP coated IONP exhibits high solubility and stability in various buffer and serum. They discover that macrophages take up greater amounts of large core PVP coated IONP than Feridex (clinical used MRI CAs), which results in the slightly higher contrast signal caused by PVP coated IONP than Feridex.

6.2. Target ligand

IONP modified with normal small molecular is easily uptake by macrophage and clear by RES, which decreases its contrast efficiency *in vivo*. To increase the accumulation of IONP in lesion, especially tumor, much attempt have been performed by coating IONP with targeted motif. Targeting ligands, including antibodies [109,288,289], peptides [290,291], aptamers [292,293], folic acids [294,295], and hyaluronic acid [296,297] have been used to modify IONP to achieve targeted MR contrast imaging. Jia et al. modified ultra-small IONP by c(RGDyk) molecular (Fig. 22e–j) [298]. Owing to the RGD modified surface could specifically recognize tumor angiogenesis, the RGD modified IONP shows high accumulation in tumor site, which results in remarkable MR signal enhancement at hepatic tumor and low detection limit with the size of 2.2 mm. Despite each targeting ligand enables IONP with targeting ability, the type of ligand can significantly affect its targeting capacities. For example, due to the lack of consistent covalent bonding site antibodies, which is difficult to controllable attach on the surface of IONP [299]. This defect limits the presentation of antibody binding sites and lower, even hinder, its binding activity, resulting the partial loss of target capacity of IONP.

6.3. Zwitterionic molecular

When IONP enters the physiological environment, serum proteins rapidly adsorb to its surface and form protein corona. The protein corona usually consists various proteins, including adhesion mediators, signaling and transport proteins, and apolipoproteins, which could improve the uptake efficiency of IONP by macrophages in MPS [95,97]. Additionally, the protein corona alters the surface interface between each particle and result in aggregation. These defects dramatically decrease the circulation time of IONP and its accumulation in lesion, especially tumor. Previous research indicated that zwitterionic molecular, that contain either zwitterionic group or a mixture of anionic and cationic groups, could effectively reduce the non-specific protein adsorption [105,301–303]. Bawendi and Co-author found that the size of zwitterionic dopamine sulfonate coated IONP (IO@ZDS) are similar when incubated with 1 PBS, 10% FBS, and 20% FBS. These results indicate the low nonspecific affinity of IO@ZDS towards to serum proteins due to its nearly neutral charge (Fig. 22k-m) [300]. Another study investigated the circulation fate of zwitterionic dopamine sulfonate

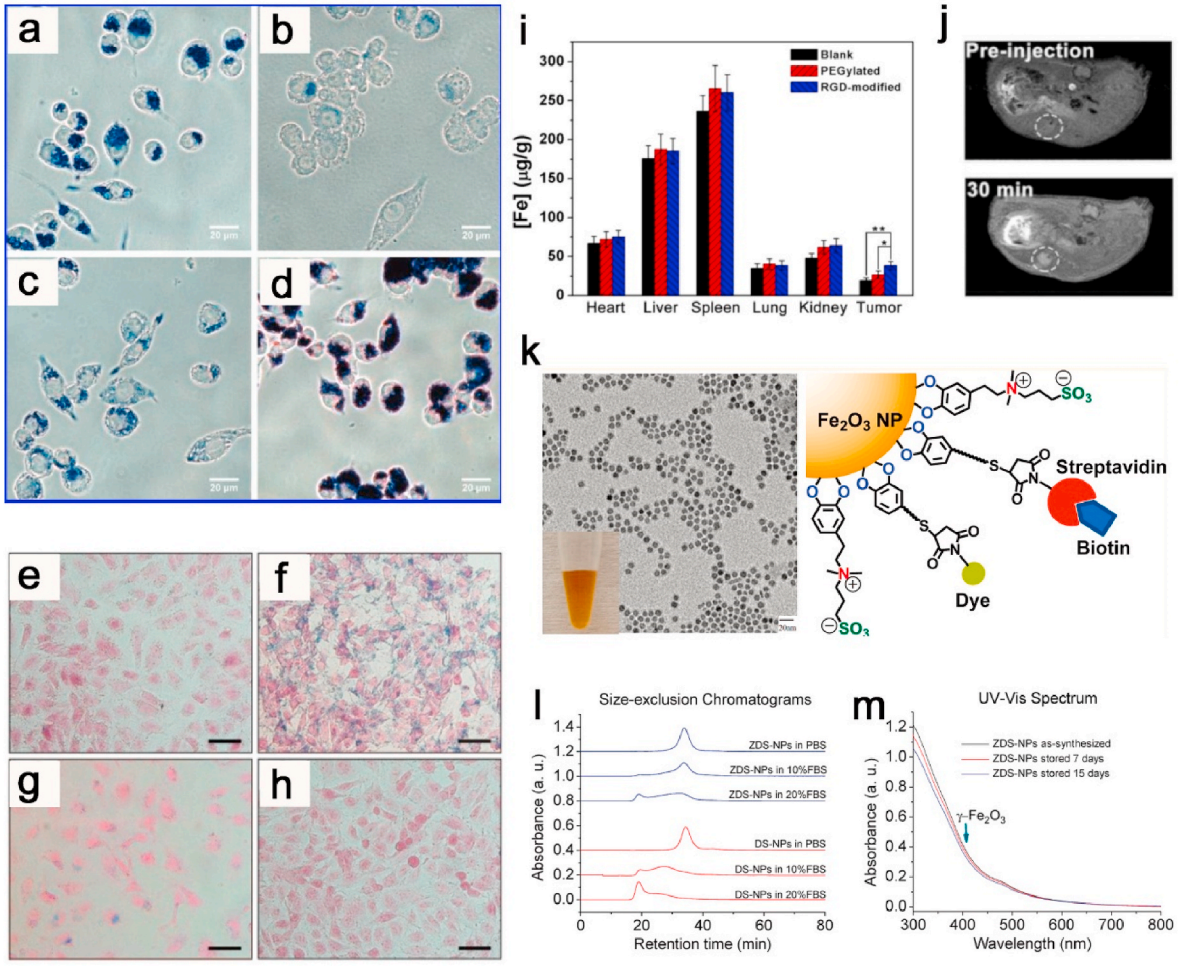

Fig. 22. Effect of surface ligand on *in vivo* contrast efficiency of IONP. Prussian blue staining of J774 macrophages after incubation with IONP coated by PEG with the molecular weight of (a) 350, (b) PEG 1100, (c) PEG 2000, and (d) Resovist. Reproduced with permission [199]. Copyright 2009, American Chemical Society. Prussian blue staining of HUVECs incubated with (e) PEGylated IONP, (f) RGD modified IONP, (g) RGD modified IONP plus free c(RGDyK), and (h) control group for 12 h at Fe concentration of 100 μg/mL. Scale bar: 20 μm for all images. (i) *In vivo* biodistribution of Fe in major organs. (j) T_1-weighted MRI images of mice bearing tumor before and after administration of RGD modified IONP. Reproduced with permission [298]. Copyright 2016, Ivyspring International Publisher. (k) TEM image and schematic cartoon of surface structure of IO@ZDS. (l) Chromatograms of IONP in serum binding test. (m) UV–Vis spectrum of IO@ZDS with the increase of storage time. Reproduced with permission [300]. Copyright 2012, American Chemical Society. (For interpretation of the references to color in this figure legend, the reader is referred to the Web version of this article.)

coated gadolinium doped IONP (GdIO@ZDS) *in vivo* [220]. The T_1-weighted signal change in heart is relative tiny after injection of GdIO@ZDS at 10, 30, and 60 min, indicating the slow elimination of GdIO@ZDS and long circulation time.

7. Improve biocompatibility

Although it is generally considered IONP are biocompatible in comparison to other metal oxide nanoparticles, there still remains concern on this aspect. Bare IONP have been found to generate reactive oxygen species and resulted in the *in vitro* cytotoxicity. Therefore, coating IONP with a more biocompatibility shell can effectively improve its biocompatibility. Since different surface coating layers show different effects on cell and different behavior in the body, various attempts have been performed to construct IONP with high biocompatibility through adjusting coating layer. Normally, the coating layer of IONP could be divided into two types, those are inorganic shell and organic shell.

7.1. Inorganic shell

Coating IONP with a biocompatible inorganic shell provides protection against release of iron ions and reactivity of IONP. After coating with the inorganic shell, the interaction activity to surrounding biological entities change from IONP to the inorganic shell. Consequently, the chemically inert shell prefer to develop IONP with high biocompatibility. Recently, gold and silica coated IONP have been discovered to be nontoxic due to their bio-inert property. Gold nanomaterial with excellent biocompatibility have been widely used in biomedical application. The cytotoxicity of gold nanoparticle have been investigated on retinal pigment epithelial (ARPE-19) cell line [304]. It appears that gold nanoparticle with small sizes shows high biocompatibility even the exposure concentration up to 5 mg/mL. Therefore, coating IONP by gold may increase its biocompatibility. Esparza and co-worker assessed the cytotoxic behavior of gold coated IONP [305]. Cytotoxicity tests indicate that the apoptosis rate of MDCK cells treated by gold coated IONP is about 0.71%, which is significantly lower that cell treated by IONP (40.33%). Gu and co-workers further assessed the *in vivo* biosafety of gold coated IONP using spleen-deficient rats. They found that coating IONP with gold can effectively increase the toxicity grade I concentration from 2.5 mg/mL of naked IONP to 5 mg/mL [306]. Further short-term genetic toxicity assessed by micronuclei and comet assay indicate that gold coated IONP show lower mutation and DNA

damage level compare to naked IONP.

Silica is generally recognized as safe by the US FDA. In recent years, various silica coated IONP with high biocompatibility have been used in biomedical application. However, it has been found that silica coated IONP show significant influence on the survival of mNSCs mouse stem cells, which may be ascribed to the release of free iron ions in cell cytoplasm after lysosomal degradation [307]. Further modification have been discovered to be an effective strategy to improve the biocompatibility of silica coated IONP. Injumpa et al. incubated PEG modified silica coated IONP, silica nanoparticles, and IONP with macrophage cells and investigated their cytotoxicity [308]. Compared to the IONP, PEG modified silica coated IONP produces less cytoxicity. More importantly, PEG modified silica coated IONP show fewer effect on the secretion of pro-inflammatory cytokines (TNF-α and IL-6) than IONP. It should note that the cytotoxicity of silica coated IONP is highly dependent on its size. Lisi and co-workers find that sub 5 nm silica coated IONP do not alter stem cell characteristics and interfere with the commitment potential [309]. *In vivo* study over 7-week period reveal negligible acute and chronic toxicity after systemically administered this silica coated IONP in mice, showing excellent cytocompatibility.

7.2. Organic shell

Biocompatibility polymer coated IONP have been found to be relatively nontoxic and utilized to improve the biocompatibility of IONP. Natural polysaccharide, especially dextran, with superior biocompatibility has been considered as a promising candidate to improve biocompatibility of IONP. Muller et al. found that dextran coated IONP displayed no effect on cell viability and increasing in cytokines or superoxide production. No toxicity was observed after incubation human monocyte-macrophages with dextran coated IONP at concentration up to 1 mg/mL over 72 h [310]. Recently, another polysaccharide, hyaluronic acid (HA), with CD-44 target activity have been developed to confer biocompatibility. Atrei et al. observe a significant increase in cell viability of NIH3T3 cells exposed to the HA modified IONP respect to bare IONP. Moreover, morphometric analyses indicate that HA modified IONP show little effect on the morphology change than bare IONP, revealing an improved biocompatibility [311]. As another natural production, protein, have been used to stabilize IONP and improved biocompatibility. Roig and co-worker developed IONP outfitted with albumin (BSA) corona and assessed their cytotoxicity in adherent and suspension cells and model organism *Caenorhabditis elegans* [312]. In comparison to the IONP without coating, BSA coated IONP are efficiently protected in lysosome and lumen of *C. elegans*. Based on the high stability, BSA coated IONP are more biocompatible than the uncoated ones on cellular level and in *C. elegans*. Apart from natural polymer, some artificial biocompatible polymers are used to improve the biocompatibility of IONP. PVA coated IONP were found to promote BT-474 cell viability at concentrations up to 100 μg/mL. Besides, no significant ROS generation and morphology change was detected in BT-474 cells incubated with PVP coated IONP at the concentration of 50 μg/mL [313]. These results indicate that the artificial synthesized polymeric shell may also induce certain cytotoxicity in cells, although it shows high biocompatibility. In future, the long-term toxicity of IONP coated by various biocompatible shell should be systemic studied to figure out the relationship between the surface coating shell and biocompatibitity and develop IONP with no toxicity in preclinical and clinical study.

8. Conclusion and perspective

IONP with unique magnetic property and high biocompatibility have been widely used as MRI CAs for a long time. To realize early and accurate lesion MRI detection, various attempts have been performed to optimize the structure of IONP. In this review, we summarize the recent progress to construct IONP based high-performance MRI CA through improve their contrast ability and efficiency. This review is started with a comprehensive discussion on the strategies to increase the contrast ability by rising r_2 or r_1 value of IONP. As a typical T_2 CA, we firstly generalized the parameters, which affect T_2 relaxivity of IONP. i) M_s. On the basis of classical theories, T_2 relaxivity of IONP is proportional to its M_s, which is highly dependent on its crystal structure. One can increase M_s of IONP by improving the crystallinity, dopant, and forming unique structure to obtain IONP with high T_2 relaxivity. ii) Effective radius. The effective radius is responsible for the field perturbation area for the outersphere protons and proportional to the T_2 relavixity in MAR. Therefore, T_2 relaxivity of IONP could be promoted by increasing its effective radius through rising crystal size, forming specific morphology, and assembling to nanocluster. It should note that when the particles or cluster size reach to a certain limit, T_2 contrast of IONP reaches to its maximum value and fulfills the SDR. iii) Proton diffusion behavior. Proton diffusion behavior in the magnetic field gradients have been discovered to influence the T_2 relaxivity of IONP. The anisotropic structure and proper coating layer could generate strong inhomogeneous magnetic field and suitable diffusion environment, which can increase proton diffusion efficiency and T_2 relaxivity of IONP. Compared to the systematical study on T_2 relaxivity of IONP, the research on its T_1 relaxivity is at the initial stage. Reduction the size of IONP, which can decrease the M_s value and increase the number of magnetic Fe ions on its surface, have been applied as the few exist methods to fabricate IONP based T_1 CAs decades ago. With the development of synthetic method, more and more novel attempts have been performed to optimize the structure of IONP to improve its T_1 relaxivity in the past ten years. By surveying the literature, we have covered a number of new structural optimization of IONP to ameliorate its T_1 relaxivity. i) Increasing q value of IONP. INOPs with hollow structure and anisotropic morphology obtained by controllable synthesis could provide increased iron ion on the interfere surface between IONP and surrounding aqueous environment, which could rise its q value and result in the T_1 relaxivity elevation. ii) Increasing unpaired electrons and improving τ_s. The existence of ferrous ions with small amount of unpaired electrons and low τ_s in IONP limits its T_1 relaxivity. The unpaired electrons and τ_s of IONP could be increased by introducing other magnetic ions with sufficient unpaired electrons or long τ_s, such as europium, manganese, gadolinium, and copper. iii) Optimizing surface structure. T_1 relaxivity of IONP is dependent on the chemical exchange efficient between IONP and water proton at the interface. Molecular weight, hydrophilic, and efficiency on charge-transfer between electronic and magnetic interactions of surface ligand have been considered as key parameters to optimize water diffusion, retention, and interaction with the magnetic centers. This beneficial effect could further improve chemical exchange efficiency between IONP and water proton and contribute to its r_1 value.

After detailed discussion on contrast ability improvement, this review then summarized the recent attempt to increase the contrast efficiency of IONP i*n vivo* from three different directions. This part starts with the discussion on recent advances of fabricating IONP with dual-modal contrast. By precise controlling the crystal structure and complementary combination of various materials, IONP with dual-modality imaging capability are emerging as versatile platform to provide comprehensive diagnostic information in disease imaging. Then IONP with the capacity to response to specific changes in the surrounding physiological microenvironment have been discussed on three different manners, those are active, recovery, and switchable. Compared to the traditional MRI CA with fixed contrast capacity in both normal and lesion tissue, this microenvironment responsive MRI CA could switch “on” and “off” T_1 or T_2 signal change in response to a specific stimulus of lesion. Ultimately, comprehensive understanding of strategies to increase the accumulation of IONP based CA in the lesion site, especially tumor site are present. In our surveyed publications, modified with PEG, target motif, and zwitterionic molecular are most applied method to increase the positive or active target behavior of IONP. This surface functional motif can optimize the circulation behavior and increase

accumulation amount of IONP in lesion, which elevate the imaging efficiency of IONP.

Nevertheless, in spite of the remarkable progresses, there are still some obstacles ahead toward further clinical translation. Despite a number of studies have proved IONP exhibits low toxicity and high biocompatibility, biocompatibility study of IONP engineered by other cations is necessary. Additionally, all strategies are performed in the laboratory, which could not consider some practical consideration in translation to clinical, such as large-scale synthesis, long-term storage, and cost in time and money. However, we still believe that IONP based high-performance MRI CA hold great promise in further clinical early and accurate diagnosis. We hope that this comprehensive review could shed light on the development of next generation IONP based MRI CA.

Declaration of competing interest

The authors declare that they have no known competing financial interests or personal relationships that could have appeared to influence the work reported in this paper.

Acknowledgements

This work was supported by the National Natural Science Foundation of China (81601607 and 81971609), Chongqing High-level Personnel of Special Support Program (Youth Top-notch Talent CQYC201905077), and Creative Research Group of CQ University (CXQT21017).

References

[1] C. Tassa, S.Y. Shaw, R. Weissleder, Dextran-coated iron oxide nanoparticles: a versatile platform for targeted molecular imaging, molecular diagnostics, and therapy, Accounts Chem. Res. 44 (2011) 842–852.
[2] M. Janowski, J.W.M. Bulte, P. Walczak, Personalized nanomedicine advancements for stem cell tracking, Adv. Drug Deliv. Rev. 64 (2012) 1488–1507.
[3] L.A. Lane, X. Qian, S. Nie, SERS nanoparticles in medicine: from label-free detection to spectroscopic tagging, Chem. Rev. 115 (2015) 10489–10529.
[4] A. Taylor, K.M. Wilson, P. Murray, D.G. Fernig, R. Lévy, Long-term tracking of cells using inorganic nanoparticles as contrast agents: are we there yet? Chem. Soc. Rev. 41 (2012) 2707–2717.
[5] M. Barrow, A. Taylor, P. Murray, M.J. Rosseinsky, D.J. Adams, Design considerations for the synthesis of polymer coated iron oxide nanoparticles for stem cell labelling and tracking using MRI, Chem. Soc. Rev. 44 (2015) 6733–6748.
[6] J.E. Smith, C.D. Medley, Z. Tang, D. Shangguan, C. Lofton, W. Tan, Aptamer-conjugated nanoparticles for the collection and detection of multiple cancer cells, Anal. Chem. 79 (2007) 3075–3082.
[7] K.C.-F. Leung, S. Xuan, X. Zhu, D. Wang, C.-P. Chak, S.-F. Lee, et al., Gold and iron oxide hybrid nanocomposite materials, Chem. Soc. Rev. 41 (2012) 1911–1928.
[8] Y. Pan, X. Du, F. Zhao, B. Xu, Magnetic nanoparticles for the manipulation of proteins and cells, Chem. Soc. Rev. 41 (2012) 2912–2942.
[9] L. Yang, X. Zhang, M. Ye, J. Jiang, R. Yang, T. Fu, et al., Aptamer-conjugated nanomaterials and their applications, Adv. Drug Deliv. Rev. 63 (2011) 1361–1370.
[10] J.N. Anker, W.P. Hall, O. Lyandres, N.C. Shah, J. Zhao, R.P. Van Duyne, Biosensing with plasmonic nanosensors, Nat. Mater. 7 (2008) 442–453.
[11] K. Saha, S.S. Agasti, C. Kim, X. Li, V.M. Rotello, Gold nanoparticles in chemical and biological sensing, Chem. Rev. 112 (2012) 2739–2779.
[12] M.-Q. He, Y.-L. Yu, J.-H. Wang, Biomolecule-tailored assembly and morphology of gold nanoparticles for LSPR applications, Nano Today 35 (2020) 101005.
[13] Y. Song, W. Wei, X. Qu, Colorimetric biosensing using smart materials, Adv. Mater. 23 (2011) 4215–4236.
[14] R.E. Armstrong, M. Horáček, P. Zijlstra, Plasmonic assemblies for real-time single-molecule biosensing, Small 16 (2020) 2003934.
[15] C. Sun, J.S.H. Lee, M. Zhang, Magnetic nanoparticles in MR imaging and Drug delivery, Adv. Drug Deliv. Rev. 60 (2008) 1252–1265.
[16] Z. Zhao, J. Bao, C. Fu, M. Lei, J. Cheng, Controllable synthesis of manganese oxide nanostructures from 0-D to 3-D and mechanistic investigation of internal relation between structure and T1 relaxivity, Chem. Mater. 29 (2017) 10455–10468.
[17] L. Jia, X. Li, H. Liu, J. Xia, X. Shi, M. Shen, Ultrasound-enhanced precision tumor theranostics using cell membrane-coated and pH-responsive nanoclusters assembled from ultrasmall iron oxide nanoparticles, Nano Today 36 (2021) 101022.
[18] D. Li, M. Shen, J. Xia, X. Shi, Recent developments of cancer nanomedicines based on ultrasmall iron oxide nanoparticles and nanoclusters, Nanomedicine 16 (2021) 609–612.
[19] F. Soetaert, P. Korangath, D. Serantes, S. Fiering, R. Ivkov, Cancer therapy with iron oxide nanoparticles: agents of thermal and immune therapies, Adv. Drug Deliv. Rev. 163–164 (2020) 65–83.
[20] S.M. Dadfar, K. Roemhild, N.I. Drude, S. von Stillfried, R. Knüchel, F. Kiessling, et al., Iron oxide nanoparticles: diagnostic, therapeutic and theranostic applications, Adv. Drug Deliv. Rev. 138 (2019) 302–325.
[21] D. Ling, N. Lee, T. Hyeon, Chemical synthesis and assembly of uniformly sized iron oxide nanoparticles for medical applications, Accounts Chem. Res. 48 (2015) 1276–1285.
[22] S. Laurent, D. Forge, M. Port, A. Roch, C. Robic, L. Vander Elst, et al., Magnetic iron oxide nanoparticles: synthesis, stabilization, vectorization, physicochemical characterizations, and biological applications, Chem. Rev. 108 (2008) 2064–2110.
[23] Y. Hu, S. Mignani, J.-P. Majoral, M. Shen, X. Shi, Construction of iron oxide nanoparticle-based hybrid platforms for tumor imaging and therapy, Chem. Soc. Rev. 47 (2018) 1874–1900.
[24] N. Lee, T. Hyeon, Designed synthesis of uniformly sized iron oxide nanoparticles for efficient magnetic resonance imaging contrast agents, Chem. Soc. Rev. 41 (2012) 2575–2589.
[25] E. Terreno, D.D. Castelli, A. Viale, S. Aime, Challenges for molecular magnetic resonance imaging, Chem. Rev. 110 (2010) 3019–3042.
[26] D. Kim, J. Kim, Y.I. Park, N. Lee, T. Hyeon, Recent development of inorganic nanoparticles for biomedical imaging, ACS Cent. Sci. 4 (2018) 324–336.
[27] J.-H. Lee, Y.-M. Huh, Y-w Jun, J-w Seo, J-t Jang, H.-T. Song, et al., Artificially engineered magnetic nanoparticles for ultra-sensitive molecular imaging, Nat. Med. 13 (2007) 95–99.
[28] J. Xie, G. Liu, H.S. Eden, H. Ai, X. Chen, Surface-engineered magnetic nanoparticle platforms for cancer imaging and therapy, Accounts Chem. Res. 44 (2011) 883–892.
[29] Z. Shen, A. Wu, X. Chen, Iron oxide nanoparticle based contrast agents for magnetic resonance imaging, Mol. Pharm. 14 (2017) 1352–1364.
[30] L. Yang, Z. Zhou, J. Song, X. Chen, Anisotropic nanomaterials for shape-dependent physicochemical and biomedical applications, Chem. Soc. Rev. 48 (2019) 5140–5176.
[31] Z. Zhou, L. Yang, J. Gao, X. Chen, Structure–relaxivity relationships of magnetic nanoparticles for magnetic resonance imaging, Adv. Mater. 31 (2019) 1804567.
[32] H. Lee, T.-H. Shin, J. Cheon, R. Weissleder, Recent developments in magnetic diagnostic systems, Chem. Rev. 115 (2015) 10690–10724.
[33] W.S. Seo, J.H. Lee, X. Sun, Y. Suzuki, D. Mann, Z. Liu, et al., FeCo/Graphitic-Shell nanocrystals as advanced magnetic-resonance-imaging and near-infrared agents, Nat. Mater. 5 (2006) 971–976.
[34] J. Yu, C. Yang, J. Li, Y. Ding, L. Zhang, M.Z. Yousaf, et al., Multifunctional Fe_5C_2 nanoparticles: a targeted theranostic platform for magnetic resonance imaging and photoacoustic tomography-guided photothermal therapy, Adv. Mater. 26 (2014) 4114–4120.
[35] C.G. Hadjipanayis, M.J. Bonder, S. Balakrishnan, X. Wang, H. Mao, G. C. Hadjipanayis, Metallic iron nanoparticles for MRI contrast enhancement and local hyperthermia, Small 4 (2008) 1925–1929.
[36] Z. Zhou, X. Zhu, D. Wu, Q. Chen, D. Huang, C. Sun, et al., Anisotropic shaped iron oxide nanostructures: controlled synthesis and proton relaxation shortening effects, Chem. Mater. 27 (2015) 3505–3515.
[37] W. Xie, Z. Guo, F. Gao, Q. Gao, D. Wang, B-s Liaw, et al., Shape-, size- and structure-controlled synthesis and biocompatibility of iron oxide nanoparticles for magnetic theranostics, Theranostics 8 (2018) 3284–3307.
[38] A.G. Roca, L. Gutiérrez, H. Gavilán, M.E. Fortes Brollo, S. Veintemillas-Verdaguer, MdP. Morales, Design strategies for shape-controlled magnetic iron oxide nanoparticles, Adv. Drug Deliv. Rev. 138 (2019) 68–104.
[39] W. Xie, Z. Guo, F. Gao, Q. Gao, D. Wang, B-s Liaw, et al., Shape-, size- and structure-controlled synthesis and biocompatibility of iron oxide nanoparticles for magnetic theranostics, Theranostics 8 (2018) 3284–3307.
[40] W. Zhang, L. Liu, H. Chen, K. Hu, I. Delahunty, S. Gao, et al., Surface impact on nanoparticle-based magnetic resonance imaging contrast agents, Theranostics 8 (2018) 2521–2548.
[41] L.E.W. LaConte, N. Nitin, O. Zurkiya, D. Caruntu, C.J. O'Connor, X. Hu, et al., Coating thickness of magnetic iron oxide nanoparticles affects R_2 relaxivity, J. Magn. Reson. Imag. 26 (2007) 1634–1641.
[42] Y. Peng, Y. Gao, C. Yang, R. Guo, X. Shi, X. Cao, Low-molecular-weight poly (ethylenimine) nanogels loaded with ultrasmall iron oxide nanoparticles for T_1-weighted MR imaging-guided gene therapy of sarcoma, ACS Appl. Mater. Interfaces 13 (2021) 27806–27813.
[43] M. Jeon, M.V. Halbert, Z.R. Stephen, M. Zhang, Iron oxide nanoparticles as T_1 contrast agents for magnetic resonance imaging: fundamentals, challenges, applications, and prospectives, Adv. Mater. 33 (2021) 1906539.
[44] Y. Bao, J.A. Sherwood, Z. Sun, Magnetic iron oxide nanoparticles as T_1 contrast agents for magnetic resonance imaging, J. Mater. Chem. C 6 (2018) 1280–1290.
[45] B.H. Kim, M.J. Hackett, J. Park, T. Hyeon, Synthesis, characterization, and application of ultrasmall nanoparticles, Chem. Mater. 26 (2014) 59–71.
[46] B.H. Kim, N. Lee, H. Kim, K. An, Y.I. Park, Y. Choi, et al., Large-scale synthesis of uniform and extremely small-sized iron oxide nanoparticles for high-resolution T_1 magnetic resonance imaging contrast agents, J. Am. Chem. Soc. 133 (2011) 12624–12631.
[47] L. Sandiford, A. Phinikaridou, A. Protti, L.K. Meszaros, X. Cui, Y. Yan, et al., Bisphosphonate-anchored PEGylation and radiolabeling of superparamagnetic iron oxide: long-circulating nanoparticles for in vivo multimodal (T_1 MRI-SPECT) imaging, ACS Nano 7 (2013) 500–512.

[48] R.G.D. Andrade, S.R.S. Veloso, E.M.S. Castanheira, Shape anisotropic iron oxide-based magnetic nanoparticles: synthesis and biomedical applications, Int. J. Mol. Sci. 21 (2020) 2455.

[49] S. Xu, J. Wang, Y. Wei, H. Zhao, T. Tao, H. Wang, et al., In situ one-pot synthesis of Fe_2O_3@BSA core-shell nanoparticles as enhanced T_1-weighted magnetic resonance imagine contrast agents, ACS Appl. Mater. Interfaces 12 (2020) 56701–56711.

[50] S. Aryal, J. Key, C. Stigliano, J.S. Ananta, M. Zhong, P. Decuzzi, Engineered magnetic hybrid nanoparticles with enhanced relaxivity for tumor imaging, Biomaterials 34 (2013) 7725–7732.

[51] Z. Zhao, C. Sun, J. Bao, L. Yang, R. Wei, J. Cheng, et al., Surface manganese substitution in magnetite nanocrystals enhances T_1 contrast ability by increasing electron spin relaxation, J. Mater. Chem. B 6 (2018) 401–413.

[52] Z. Zhou, R. Bai, J. Munasinghe, Z. Shen, L. Nie, X. Chen, T_1–T_2 dual-modal magnetic resonance imaging: from molecular basis to contrast agents, ACS Nano 11 (2017) 5227–5232.

[53] G. Zhang, R. Du, L. Zhang, D. Cai, X. Sun, Y. Zhou, et al., Gadolinium-doped iron oxide nanoprobe as multifunctional bioimaging agent and Drug delivery system, Adv. Funct. Mater. 25 (2015) 6101–6111.

[54] A. Alipour, Z. Soran-Erdem, M. Utkur, V.K. Sharma, O. Algin, E.U. Saritas, et al., A new cass of cubic SPIONs as a dual-mode T_1 and T_2 contrast agent for MRI, Magn. Reson. Imaging 49 (2018) 16–24.

[55] L. Wang, H. Lin, L. Ma, J. Jin, T. Shen, R. Wei, et al., Albumin-based nanoparticles loaded with hydrophobic gadolinium chelates as T_1–T_2 dual-mode contrast agents for accurate liver tumor imaging, Nanoscale 9 (2017) 4516–4523.

[56] F. Li, D. Zhi, Y. Luo, J. Zhang, X. Nan, Y. Zhang, et al., Core/shell Fe_3O_4/Gd_2O_3 nanocubes as T_1–T_2 dual modal MRI contrast agents, Nanoscale 8 (2016) 12826–12833.

[57] N. Xiao, W. Gu, H. Wang, Y. Deng, X. Shi, L. Ye, T_1–T_2 dual-modal MRI of brain gliomas using PEGylated Gd-doped iron oxide nanoparticles, J. Colloid Interface Sci. 417 (2014) 159–165.

[58] J-s Choi, S. Kim, D. Yoo, T.-H. Shin, H. Kim, M.D. Gomes, et al., Distance-dependent magnetic resonance tuning as a versatile MRI sensing platform for biological targets, Nat. Mater. 16 (2017) 537–542.

[59] D. Ni, W. Bu, E.B. Ehlerding, W. Cai, J. Shi, Engineering of inorganic nanoparticles as magnetic resonance imaging contrast agents, Chem. Soc. Rev. 46 (2017) 7438–7468.

[60] T.-H. Shin, J-s Choi, S. Yun, I.-S. Kim, H.-T. Song, Y. Kim, et al., T_1 and T_2 dual-mode MRI contrast agent for enhancing accuracy by engineered nanomaterials, ACS Nano 8 (2014) 3393–3401.

[61] Y. Miao, Q. Xie, H. Zhang, J. Cai, X. Liu, J. Jiao, et al., Composition-tunable ultrasmall manganese ferrite nanoparticles: insights into their in vivo T1 contrast efficacy, Theranostics 9 (2019) 1764–1776.

[62] H. Wan, P. Rong, X. Liu, L. Yang, Y. Jiang, N. Zhang, et al., Morphological evolution and magnetic property of rare-earth-doped hematite nanoparticles: promising contrast agents for T_1-weighted magnetic resonance imaging, Adv. Funct. Mater. 27 (2017) 1606821.

[63] H. Zhang, L. Li, X.L. Liu, J. Jiao, C.-T. Ng, J.B. Yi, et al., Ultrasmall ferrite nanoparticles synthesized via dynamic simultaneous thermal decomposition for high-performance and multifunctional T_1 magnetic resonance imaging contrast agent, ACS Nano 11 (2017) 3614–3631.

[64] Z. Gao, Y. Hou, J. Zeng, L. Chen, C. Liu, W. Yang, et al., Tumor microenvironment-triggered aggregation of antiphagocytosis ^{99m}Tc-labeled Fe_3O_4 nanoprobes for enhanced tumor imaging in vivo, Adv. Mater. 29 (2017) 1701095.

[65] C.-T. Yang, K.K. Ghosh, P. Padmanabhan, O. Langer, J. Liu, D.N.C. Eng, et al., PET-MR and SPECT-MR multimodality probes: development and challenges, Theranostics 8 (2018) 6210–6232.

[66] R. Torres Martin de Rosales, R. Tavaré, A. Glaria, G. Varma, A. Protti, P.J. Blower, ^{99m}Tc-Bisphosphonate-Iron oxide nanoparticle conjugates for dual-modality biomedical imaging, Bioconjugate Chem. 22 (2011) 455–465.

[67] F. Chen, P.A. Ellison, C.M. Lewis, H. Hong, Y. Zhang, S. Shi, et al., Chelator-free synthesis of a dual-modality PET/MRI agent, Angew. Chem. Int. Ed. 52 (2013) 13319–13323.

[68] F. Ai, C.A. Ferreira, F. Chen, W. Cai, Engineering of radiolabeled iron oxide nanoparticles for dual-modality imaging, Wiley Interdiscip Rev-Nanomed Nanobiotechnol 8 (2016) 619–630.

[69] J. Reguera, D. Jiménez de Aberasturi, M. Henriksen-Lacey, J. Langer, A. Espinosa, B. Szczupak, et al., Janus plasmonic–magnetic gold–iron oxide nanoparticles as contrast agents for multimodal imaging, Nanoscale 9 (2017) 9467–9480.

[70] P.C. Naha, A. Al Zaki, E. Hecht, M. Chorny, P. Chhour, E. Blankemeyer, et al., Dextran coated bismuth–iron oxide nanohybrid contrast agents for computed tomography and magnetic resonance imaging, J. Mater. Chem. B 2 (2014) 8239–8248.

[71] X. Chen, G. Li, Q. Han, X. Li, L. Li, T. Wang, et al., Rational design of branched Au–Fe3O4 Janus nanoparticles for simultaneous trimodal imaging and photothermal therapy of cancer cells, Chem. Eur J. 23 (2017) 17204–17208.

[72] X. Liu, H. Jiang, J. Ye, C. Zhao, S. Gao, C. Wu, et al., Nitrogen-doped carbon quantum dot stabilized magnetic iron oxide nanoprobe for fluorescence, magnetic resonance, and computed tomography triple-modal in vivo bioimaging, Adv. Funct. Mater. 26 (2016) 8694–8706.

[73] J.-H. Lee, Y-w Jun, S.-I. Yeon, J.-S. Shin, J. Cheon, Dual-mode nanoparticle probes for high-performance magnetic resonance and fluorescence imaging of neuroblastoma, Angew. Chem. Int. Ed. 45 (2006) 8160–8162.

[74] L. Jing, K. Ding, S.V. Kershaw, I.M. Kempson, A.L. Rogach, M. Gao, Magnetically engineered semiconductor quantum dots as multimodal imaging probes, Adv. Mater. 26 (2014) 6367–6386.

[75] J.E. Lemaster, F. Chen, T. Kim, A. Hariri, J.V. Jokerst, Development of a trimodal contrast agent for acoustic and magnetic particle imaging of stem cells, ACS Appl Nano Mater 1 (2018) 1321–1331.

[76] W. Guo, D. Li, J-a Zhu, X. Wei, W. Men, D. Yin, et al., A magnetic nanoparticle stabilized gas containing emulsion for multimodal imaging and triggered Drug release, Pharm. Res. (N. Y.) 31 (2014) 1477–1484.

[77] B.-Q. Lu, Y.-J. Zhu, H.-Y. Ao, C. Qi, F. Chen, Synthesis and characterization of magnetic iron oxide/calcium silicate mesoporous nanocomposites as a promising vehicle for Drug delivery, ACS Appl. Mater. Interfaces 4 (2012) 6969–6974.

[78] J.P. Thawani, A. Amirshaghaghi, L. Yan, J.M. Stein, J. Liu, A. Tsourkas, Photoacoustic-guided surgery with indocyanine green-coated superparamagnetic iron oxide nanoparticle clusters, Small 13 (2017) 1701300.

[79] Y. Duan, Y. Xu, D. Mao, W.H. Liew, B. Guo, S. Wang, et al., Photoacoustic and magnetic resonance imaging bimodal contrast agent displaying amplified photoacoustic signal, Small 14 (2018) 1800652.

[80] X. Song, H. Gong, S. Yin, L. Cheng, C. Wang, Z. Li, et al., Ultra-small iron oxide doped polypyrrole nanoparticles for in vivo multimodal imaging guided photothermal therapy, Adv. Funct. Mater. 24 (2014) 1194–1201.

[81] Y. Jin, C. Jia, S.-W. Huang, M. O'Donnell, X. Gao, Multifunctional nanoparticles as coupled contrast agents, Nat. Commun. 1 (2010) 41.

[82] Z. Ma, X. Jia, J. Bai, Y. Ruan, C. Wang, J. Li, et al., MnO2 gatekeeper: an intelligent and O2-evolving shell for preventing premature release of high cargo payload core, overcoming tumor hypoxia, and acidic H_2O_2-sensitive MRI, Adv. Funct. Mater. 27 (2017) 1604258.

[83] L.-S. Lin, J. Song, L. Song, K. Ke, Y. Liu, Z. Zhou, et al., Simultaneous fenton-like ion delivery and glutathione depletion by MnO2-based nanoagent to enhance chemodynamic therapy, Angew. Chem. Int. Ed. 57 (2018) 4902–4906.

[84] Y. Chen, D. Ye, M. Wu, H. Chen, L. Zhang, J. Shi, et al., Break-up of two-dimensional MnO2 nanosheets promotes ultrasensitive pH-triggered theranostics of cancer, Adv. Mater. 26 (2014) 7019–7026.

[85] Fu S, Cai Z, Ai H. Stimulus-responsive nanoparticle magnetic resonance imaging contrast agents: design considerations and applications. Adv Healthc Mater.n/a: 2001091.

[86] M. Carril, Activatable probes for diagnosis and biomarker detection by MRI, J. Mater. Chem. B 5 (2017) 4332–4347.

[87] Q. Wu, G. Chen, K. Gong, J. Wang, X. Ge, X. Liu, et al., MnO_2-Laden black phosphorus for MRI-guided synergistic PDT, PTT, and chemotherapy, Matter 1 (2019) 496–512.

[88] D. Ma, M. Shi, X. Li, J. Zhang, Y. Fan, K. Sun, et al., Redox-sensitive clustered ultrasmall iron oxide nanoparticles for switchable T2/T1-weighted magnetic resonance imaging applications, Bioconjugate Chem. 31 (2020) 352–359.

[89] J. Yu, F. Zhao, W. Gao, X. Yang, Y. Ju, L. Zhao, et al., Magnetic reactive oxygen species nanoreactor for switchable magnetic resonance imaging guided cancer therapy based on pH-sensitive Fe_5C_2@Fe_3O_4 nanoparticles, ACS Nano 13 (2019) 10002–10014.

[90] L. Wang, J. Huang, H. Chen, H. Wu, Y. Xu, Y. Li, et al., Exerting enhanced permeability and retention effect driven delivery by ultrafine iron oxide nanoparticles with T_1–T_2 switchable magnetic resonance imaging contrast, ACS Nano 11 (2017) 4582–4592.

[91] Y. Cao, Z. Mao, Y. He, Y. Kuang, M. Liu, Y. Zhou, et al., Extremely small iron oxide nanoparticle-encapsulated nanogels as a glutathione-responsive T_1 contrast agent for tumor-targeted magnetic resonance imaging, ACS Appl. Mater. Interfaces 12 (2020) 26973–26981.

[92] Y. Cao, Y. He, Z. Mao, Y. Kuang, M. Liu, Y. Zhang, et al., Synergistic regulation of longitudinal and transverse relaxivity of extremely small iron oxide nanoparticles (ESIONPs) using pH-responsive nanoassemblies, Nanoscale 12 (2020) 17502–17516.

[93] C. Bai, Z. Jia, L. Song, W. Zhang, Y. Chen, F. Zang, et al., Time-dependent T_1–T_2 switchable magnetic resonance imaging realized by c(RGDyK) modified ultrasmall Fe_3O_4 nanoprobes, Adv. Funct. Mater. 28 (2018) 1802281.

[94] B. Wu, K. Deng, S.-T. Lu, C.-J. Zhang, Y.-W. Ao, H. Wang, et al., Reduction-active Fe_3O_4-loaded micelles with aggregation- enhanced MRI contrast for differential diagnosis of neroglioma, Biomaterials 268 (2021) 120531.

[95] M.P. Monopoli, C. Åberg, A. Salvati, K.A. Dawson, Biomolecular coronas provide the biological identity of nanosized materials, Nat. Nanotechnol. 7 (2012) 779–786.

[96] A. Verma, F. Stellacci, Effect of surface properties on nanoparticle–cell interactions, Small 6 (2010) 12–21.

[97] C.D. Walkey, J.B. Olsen, H. Guo, A. Emili, W.C.W. Chan, Nanoparticle size and surface Chemistry determine serum protein adsorption and macrophage uptake, J. Am. Chem. Soc. 134 (2012) 2139–2147.

[98] E.C. Cho, J. Xie, P.A. Wurm, Y. Xia, Understanding the role of surface charges in cellular adsorption versus internalization by selectively removing gold nanoparticles on the cell surface with a I2/KI etchant, Nano Lett. 9 (2009) 1080–1084.

[99] J. Xie, C. Xu, N. Kohler, Y. Hou, S. Sun, Controlled PEGylation of monodisperse Fe_3O_4 nanoparticles for reduced non-specific uptake by macrophage cells, Adv. Mater. 19 (2007) 3163–3166.

[100] S. Ray, Z. Li, C.-H. Hsu, L.-P. Hwang, Y.-C. Lin, P.-T. Chou, et al., Dendrimer- and copolymer-based nanoparticles for magnetic resonance cancer theranostics, Theranostics 8 (2018) 6322–6349.

[101] A.S. Karakoti, S. Das, S. Thevuthasan, S. Seal, PEGylated inorganic nanoparticles, Angew. Chem. Int. Ed. 50 (2011) 1980–1994.

[102] M. Lei, C. Fu, X. Cheng, B. Fu, N. Wu, Q. Zhang, et al., Activated surface charge-reversal manganese oxide nanocubes with high surface-to-volume ratio for accurate magnetic resonance tumor imaging, Adv. Funct. Mater. 27 (2017) 1700978.
[103] J.V. Jokerst, T. Lobovkina, R.N. Zare, S.S. Gambhir, Nanoparticle PEGylation for imaging and therapy, Nanomedicine 6 (2011) 715–728.
[104] D. Ling, M.J. Hackett, T. Hyeon, Surface ligands in synthesis, modification, assembly and biomedical applications of nanoparticles, Nano Today 9 (2014) 457–477.
[105] Y.-Y. Yuan, C.-Q. Mao, X.-J. Du, J.-Z. Du, F. Wang, J. Wang, Surface charge switchable nanoparticles based on zwitterionic polymer for enhanced Drug delivery to tumor, Adv. Mater. 24 (2012) 5476–5480.
[106] K.P. García, K. Zarschler, L. Barbaro, J.A. Barreto, W. O'Malley, L. Spiccia, et al., Zwitterionic-coated "stealth" nanoparticles for biomedical applications: recent advances in countering biomolecular corona formation and uptake by the mononuclear phagocyte system, Small 10 (2014) 2516–2529.
[107] Y. Luo, J. Yang, Y. Yan, J. Li, M. Shen, G. Zhang, et al., RGD-functionalized ultrasmall iron oxide nanoparticles for targeted T_1-weighted MR imaging of gliomas, Nanoscale 7 (2015) 14538–14546.
[108] T. Sun, Y.S. Zhang, B. Pang, D.C. Hyun, M. Yang, Y. Xia, Engineered nanoparticles for Drug delivery in cancer therapy, Angew. Chem. Int. Ed. 53 (2014) 12320–12364.
[109] A.V. Ivanova, A.A. Nikitin, A.N. Gabashvily, D.A. Vishnevskiy, M.A. Abakumov, Synthesis and intensive analysis of antibody labeled single core magnetic nanoparticles for targeted delivery to the cell membrane, J. Magn. Magn Mater. 521 (2021) 167487.
[110] M.V. Yigit, D. Mazumdar, Y. Lu, MRI detection of thrombin with aptamer functionalized superparamagnetic iron oxide nanoparticles, Bioconjugate Chem. 19 (2008) 412–417.
[111] S. Bamrungsap, M.I. Shukoor, T. Chen, K. Sefah, W. Tan, Detection of lysozyme magnetic relaxation switches based on aptamer-functionalized superparamagnetic nanoparticles, Anal. Chem. 83 (2011) 7795–7799.
[112] I. Solomon, Relaxation processes in a system of 2 spins, Phys. Rev. 99 (1955) 559–565.
[113] M. Gueron, Nuclear-relaxation in macromolecules by paramagnetic-ions-novel mechanism, J. Magn. Reson. 19 (1975) 58–66.
[114] A. Rubinstein Mb, Z. Luz, Electonic and nuclear relaxation in solution of transition metal ions with spin S=3/2 and S=5/2, Mol. Phys. 20 (1971) 67. -+.
[115] B. Baishya, T.F. Segawa, G. Bodenhausen, Apparent transverse relaxation rates in systems with scalar-coupled protons, J. Am. Chem. Soc. 131 (2009) 17538–17539.
[116] I. Kuprov, D.M. Hodgson, J. Kloesges, C.I. Pearson, B. Odell, T.D.W. Claridge, Anomalous nuclear overhauser effects in carbon-substituted aziridines: scalar cross-relaxation of the first kind, Angew. Chem. Int. Ed. 54 (2015) 3697–3701.
[117] R.A. Brooks, F. Moiny, P. Gillis, On T_2-shortening by weakly magnetized particles: the chemical exchange model, Magn. Reson. Med. 45 (2001) 1014–1020.
[118] H.W. de Haan, Mechanisms of proton spin dephasing in a system of magnetic particles, Magn. Reson. Med. 66 (2011) 1748–1758.
[119] A. Bjørnerud, L. Johansson, The utility of superparamagnetic contrast agents in MRI: theoretical consideration and applications in the cardiovascular system, NMR Biomed. 17 (2004) 465–477.
[120] Q.L. Vuong, Y. Gossuin, P. Gillis, S. Delangre, New simulation approach using classical formalism to water nuclear magnetic relaxation dispersions in presence of superparamagnetic particles used as MRI contrast agents, J. Chem. Phys. 137 (2012) 114505.
[121] A. Roch, R.N. Muller, P. Gillis, Theory of proton relaxation induced by superparamagnetic particles, J. Chem. Phys. 110 (1999) 5403–5411.
[122] S.H. Koenig, K.E. Kellar, Theory of $1/T_1$ and $1/T_2$ NMRD profiles of solutions of magnetic nanoparticles, Magn. Reson. Med. 34 (1995) 227–233.
[123] P. Gillis, F. Moiny, R.A. Brooks, On T_2-shortening by strongly magnetized spheres: a partial refocusing model, Magn. Reson. Med. 47 (2002) 257–263.
[124] R.A. Brooks, T_2-Shortening by strongly magnetized spheres: a chemical exchange model, Magn. Reson. Med. 47 (2002) 388–391.
[125] D.A. Yablonskiy, E.M. Haacke, Theory of NMR signal behavior in magnetically inhomogeneous tissues: the static dephasing regime, Magn. Reson. Med. 32 (1994) 749–763.
[126] A. Roch, Y. Gossuin, R.N. Muller, P. Gillis, Superparamagnetic colloid suspensions: water magnetic relaxation and clustering, J. Magn. Magn Mater. 293 (2005) 532–539.
[127] C. Yang, J. Wu, Y. Hou, Fe_3O_4 nanostructures: synthesis, growth mechanism, properties and applications, Chem. Commun. 47 (2011) 5130–5141.
[128] T. Hyeon, Chemical synthesis of magnetic nanoparticles, Chem. Commun. (2003) 927–934.
[129] W. Wu, C.Z. Jiang, V.A.L. Roy, Designed synthesis and surface engineering strategies of magnetic iron oxide nanoparticles for biomedical applications, Nanoscale 8 (2016) 19421–19474.
[130] R. Hachani, M. Lowdell, M. Birchall, A. Hervault, D. Mertz, S. Begin-Colin, et al., Polyol synthesis, functionalisation, and biocompatibility studies of superparamagnetic iron oxide nanoparticles as potential MRI contrast agents, Nanoscale 8 (2016) 3278–3287.
[131] A.G. Kolhatkar, A.C. Jamison, D. Litvinov, R.C. Willson, T.R. Lee, Tuning the magnetic properties of nanoparticles, Int. J. Mol. Sci. 14 (2013) 15977–16009.
[132] C. Pereira, A.M. Pereira, C. Fernandes, M. Rocha, R. Mendes, M.P. Fernández-García, et al., Superparamagnetic MFe_2O_4 (M = Fe, Co, Mn) nanoparticles: tuning the particle size and magnetic properties through a novel one-step coprecipitation route, Chem. Mater. 24 (2012) 1496–1504.
[133] H. Deng, X. Li, Q. Peng, X. Wang, J. Chen, Y. Li, Monodisperse magnetic single-crystal ferrite microspheres, Angew. Chem. Int. Ed. 44 (2005) 2782–2785.
[134] L. Yang, L. Ma, J. Xin, A. Li, C. Sun, R. Wei, et al., Composition tunable manganese ferrite nanoparticles for optimized T_2 contrast ability, Chem. Mater. 29 (2017) 3038–3047.
[135] J-t Jang, H. Nah, J.-H. Lee, S.H. Moon, M.G. Kim, J. Cheon, Critical enhancements of MRI contrast and hyperthermic effects by dopant-controlled magnetic nanoparticles, Angew. Chem. Int. Ed. 48 (2009) 1234–1238.
[136] H. Khurshid, C.G. Hadjipanayis, H. Chen, W. Li, H. Mao, R. Machaidze, et al., Core/shell structured iron/iron-oxide nanoparticles as excellent MRI contrast enhancement agents, J. Magn. Magn Mater. 331 (2013) 17–20.
[137] Z. Zhou, Y. Sun, J. Shen, J. Wei, C. Yu, B. Kong, et al., Iron/iron oxide core/shell nanoparticles for magnetic targeting MRI and near-infrared photothermal therapy, Biomaterials 35 (2014) 7470–7478.
[138] A.I. Martínez-Banderas, A. Aires, M. Quintanilla, J.A. Holguín-Lerma, C. Lozano-Pedraza, F.J. Teran, et al., Iron-based core–shell nanowires for combinatorial Drug delivery and photothermal and magnetic therapy, ACS Appl. Mater. Interfaces 11 (2019) 43976–43988.
[139] S. Cheong, P. Ferguson, K.W. Feindel, I.F. Hermans, P.T. Callaghan, C. Meyer, et al., Simple synthesis and functionalization of iron nanoparticles for magnetic resonance imaging, Angew. Chem. Int. Ed. 50 (2011) 4206–4209.
[140] L.-M. Lacroix, N. Frey Huls, D. Ho, X. Sun, K. Cheng, S. Sun, Stable single-crystalline body centered cubic Fe nanoparticles, Nano Lett. 11 (2011) 1641–1645.
[141] T.-J. Yoon, H. Lee, H. Shao, R. Weissleder, Highly magnetic core–shell nanoparticles with a unique magnetization mechanism, Angew. Chem. Int. Ed. 50 (2011) 4663–4666.
[142] R. Frison, G. Cernuto, A. Cervellino, O. Zaharko, G.M. Colonna, A. Guagliardi, et al., Magnetite–maghemite nanoparticles in the 5–15 nm range: correlating the core–shell composition and the surface structure to the magnetic properties. A total scattering study, Chem. Mater. 25 (2013) 4820–4827.
[143] M.P. Morales, C.J. Serna, F. Bødker, S. Mørup, Spin canting due to structural disorder in maghemite, J Phys-Condes Matter. 9 (1997) 5461–5467.
[144] E.L. Jr, A.L. Brandl, A.D. Arelaro, G.F. Goya, Spin disorder and magnetic anisotropy in Fe_3O_4 nanoparticles, J. Appl. Phys. 99 (2006), 083908.
[145] Ö. Helgason, H.K. Rasmussen, S. Mørup, Spin-canting and transverse relaxation in maghemite nanoparticles and in tin-doped maghemite, J. Magn. Magn Mater. 302 (2006) 413–420.
[146] M.P. Morales, S. Veintemillas-Verdaguer, M.I. Montero, C.J. Serna, A. Roig, L. Casas, et al., Surface and internal spin canting in γ-Fe_2O_3 nanoparticles, Chem. Mater. 11 (1999) 3058–3064.
[147] S. Mørup, Spin-canting and transverse relaxation at surfaces and in the interior of ferrimagnetic particles, J. Magn. Magn Mater. 266 (2003) 110–118.
[148] M. Unni, A.M. Uhl, S. Savliwala, B.H. Savitzky, R. Dhavalikar, N. Garraud, et al., Thermal decomposition synthesis of iron oxide nanoparticles with diminished magnetic dead layer by controlled addition of oxygen, ACS Nano 11 (2017) 2284–2303.
[149] S-h Noh, W. Na, J-t Jang, J.-H. Lee, E.J. Lee, S.H. Moon, et al., Nanoscale magnetism control via surface and exchange anisotropy for optimized ferrimagnetic hysteresis, Nano Lett. 12 (2012) 3716–3721.
[150] Y-w Jun, Y.-M. Huh, J-s Choi, J.-H. Lee, H.-T. Song, S. Kim, et al., Nanoscale size effect of magnetic nanocrystals and their utilization for cancer diagnosis via magnetic resonance imaging, J. Am. Chem. Soc. 127 (2005) 5732–5733.
[151] U.I. Tromsdorf, N.C. Bigall, M.G. Kaul, O.T. Bruns, M.S. Nikolic, B. Mollwitz, et al., Size and surface effects on the MRI relaxivity of manganese ferrite nanoparticle contrast agents, Nano Lett. 7 (2007) 2422–2427.
[152] H.M. Joshi, Y.P. Lin, M. Aslam, P.V. Prasad, E.A. Schultz-Sikma, R. Edelman, et al., Effects of shape and size of cobalt ferrite nanostructures on their MRI contrast and thermal activation, J. Phys. Chem. C 113 (2009) 17761–17767.
[153] G. Huang, H. Li, J. Chen, Z. Zhao, L. Yang, X. Chi, et al., Tunable T_1 and T_2 contrast abilities of manganese-engineered iron oxide nanoparticles through size control, Nanoscale 6 (2014) 10404–10412.
[154] Z. Zhao, Z. Zhou, J. Bao, Z. Wang, J. Hu, X. Chi, et al., Octapod iron oxide nanoparticles as high-performance T_2 contrast agents for magnetic resonance imaging, Nat. Commun. 4 (2013) 2266.
[155] Z. Zhou, Z. Zhao, H. Zhang, Z. Wang, X. Chen, R. Wang, et al., Interplay between longitudinal and transverse contrasts in Fe3O4 nanoplates with (111) exposed surfaces, ACS Nano 8 (2014) 7976–7985.
[156] R. Wei, T. Zhou, C. Sun, H. Lin, L. Yang, B.W. Ren, et al., Iron-oxide-based twin nanoplates with strong T_2 relaxation shortening for contrast-enhanced magnetic resonance imaging, Nanoscale 10 (2018) 18398–18406.
[157] S.F. Situ-Loewenstein, S. Wickramasinghe, E.C. Abenojar, B.O. Erokwu, C. A. Flask, Z. Lee, et al., A novel synthetic route for high-index faceted iron oxide concave nanocubes with high T_2 relaxivity for in vivo MRI applications, J. Mater. Sci. Mater. Med. 29 (2018) 58.
[158] N. Lee, Y. Choi, Y. Lee, M. Park, W.K. Moon, S.H. Choi, et al., Water-dispersible ferrimagnetic iron oxide nanocubes with extremely high r2 relaxivity for highly sensitive in vivo MRI of tumors, Nano Lett. 12 (2012) 3127–3131.
[159] P.P. Wyss, S. Lamichhane, M. Rauber, R. Thomann, K.W. Krämer, V.P. Shastri, Tripod USPIONs with high aspect ratio show enhanced T_2 relaxation and cytocompatibility, Nanomedicine 11 (2016) 1017–1030.
[160] L. Yang, Z. Wang, L. Ma, A. Li, J. Xin, R. Wei, et al., The roles of morphology on the relaxation rates of magnetic nanoparticles, ACS Nano 12 (2018) 4605–4614.
[161] Q.L. Vuong, P. Gillis, Y. Gossuin, Monte Carlo simulation and theory of proton NMR transverse relaxation induced by aggregation of magnetic particles used as MRI contrast agents, J. Magn. Reson. 212 (2011) 139–148.

[162] T.-J. Yoon, H. Lee, H. Shao, S.A. Hilderbrand, R. Weissleder, Multicore assemblies potentiate magnetic properties of biomagnetic nanoparticles, Adv. Mater. 23 (2011) 4793–4797.
[163] E. Pöselt, H. Kloust, U. Tromsdorf, M. Janschel, C. Hahn, C. Maßlo, et al., Relaxivity optimization of a PEGylated iron-oxide-based negative magnetic resonance contrast agent for T_2-weighted spin–echo imaging, ACS Nano 6 (2012) 1619–1624.
[164] H. Ai, C. Flask, B. Weinberg, X.-T. Shuai, M.D. Pagel, D. Farrell, et al., Magnetite-loaded polymeric micelles as ultrasensitive magnetic-resonance probes, Adv. Mater. 17 (2005) 1949–1952.
[165] J.E. Lee, N. Lee, H. Kim, J. Kim, S.H. Choi, J.H. Kim, et al., Uniform mesoporous dye-doped silica nanoparticles decorated with multiple magnetite nanocrystals for simultaneous enhanced magnetic resonance imaging, fluorescence imaging, and Drug delivery, J. Am. Chem. Soc. 132 (2010) 552–557.
[166] S. Song, H. Guo, Z. Jiang, Y. Jin, Z. Zhang, K. Sun, et al., Self-assembled Fe3O4/polymer hybrid microbubble with MRI/ultrasound dual-imaging enhancement, Langmuir 30 (2014) 10557–10561.
[167] J.-J. Lin, J.-S. Chen, S.-J. Huang, J.-H. Ko, Y.-M. Wang, T.-L. Chen, et al., Folic acid–pluronic F127 magnetic nanoparticle clusters for combined targeting, diagnosis, and therapy applications, Biomaterials 30 (2009) 5114–5124.
[168] K.C. Barick, M. Aslam, Y.-P. Lin, D. Bahadur, P.V. Prasad, V.P. Dravid, Novel and efficient MR active aqueous colloidal Fe_3O_4 nanoassemblies, J. Mater. Chem. 19 (2009) 7023–7029.
[169] Z. Zhao, X. Chi, L. Yang, R. Yang, B.W. Ren, X. Zhu, et al., Cation exchange of anisotropic-shaped magnetite nanoparticles generates high-relaxivity contrast agents for liver tumor imaging, Chem. Mater. 28 (2016) 3497–3506.
[170] L. Yang, C. Sun, H. Lin, X. Gong, T. Zhou, W.-T. Deng, et al., Sensitive contrast-enhanced magnetic resonance imaging of orthotopic and metastatic hepatic tumors by ultralow doses of zinc ferrite octapods, Chem. Mater. 31 (2019) 1381–1390.
[171] P.C. Liang Zpl, Principles of Magnetic Resonance Imaging: a Signal Processing Perspective, Wiley-IEEE Press, 1999.
[172] M.R.J. Carroll, R.C. Woodward, M.J. House, W.Y. Teoh, R. Amal, T.L. Hanley, et al., Experimental validation of proton transverse relaxivity models for superparamagnetic nanoparticle MRI contrast agents, Nanotechnology 21 (2009), 035103.
[173] Z. Zhou, R. Tian, Z. Wang, Z. Yang, Y. Liu, G. Liu, et al., Artificial local magnetic field inhomogeneity enhances T_2 relaxivity, Nat. Commun. 8 (2017) 15468.
[174] J. Zeng, L. Jing, Y. Hou, M. Jiao, R. Qiao, Q. Jia, et al., Anchoring group effects of surface ligands on magnetic properties of Fe_3O_4 nanoparticles: towards high performance MRI contrast agents, Adv. Mater. 26 (2014) 2694–2698.
[175] H.W. de Haan, C. Paquet, Enhancement and degradation of the R relaxation rate resulting from the encapsulation of magnetic particles with hydrophilic coatings, Magn. Reson. Med. 66 (2011) 1759–1766.
[176] J. Liu, Z. Sun, Y. Deng, Y. Zou, C. Li, X. Guo, et al., Highly water-dispersible biocompatible magnetite particles with low cytotoxicity stabilized by citrate groups, Angew. Chem. Int. Ed. 48 (2009) 5875–5879.
[177] K.B. Vargo, A.A. Zaki, R. Warden-Rothman, A. Tsourkas, D.A. Hammer, Superparamagnetic iron oxide nanoparticle micelles stabilized by recombinant oleosin for targeted magnetic resonance imaging, Small 11 (2015) 1409–1413.
[178] E. Schellenberger, J. Schnorr, C. Reutelingsperger, L. Ungethüm, W. Meyer, M. Taupitz, et al., Linking proteins with anionic nanoparticles via protamine: ultrasmall protein-coupled probes for magnetic resonance imaging of apoptosis, Small 4 (2008) 225–230.
[179] A.G. Roca, J.F. Marco, MdP. Morales, C.J. Serna, Effect of nature and particle size on properties of uniform magnetite and maghemite nanoparticles, J. Phys. Chem. C 111 (2007) 18577–18584.
[180] H.M. Joshi, M. De, F. Richter, J. He, P.V. Prasad, V.P. Dravid, Effect of silica shell thickness of Fe_3O_4–SiO_x core–shell nanostructures on MRI contrast, J. Nanoparticle Res. 15 (2013) 1448.
[181] S. Tong, S. Hou, Z. Zheng, J. Zhou, G. Bao, Coating optimization of superparamagnetic iron oxide nanoparticles for high T_2 relaxivity, Nano Lett. 10 (2010) 4607–4613.
[182] J. Huang, L. Wang, R. Lin, A.Y. Wang, L. Yang, M. Kuang, et al., Casein-coated iron oxide nanoparticles for high MRI contrast enhancement and efficient cell targeting, ACS Appl. Mater. Interfaces 5 (2013) 4632–4639.
[183] F. Reynolds, T. O'Loughlin, R. Weissleder, L. Josephson, Method of determining nanoparticle core weight, Anal. Chem. 77 (2005) 814–817.
[184] I. Solomon, Relaxation processes in a system of two spins, Phys. Rev. 99 (1955) 559–565.
[185] N. Bloembergen, L.O. Morgan, Proton relaxation times in paramagnetic solutions. Effects of electron spin relaxation, J. Chem. Phys. 34 (1961) 842–850.
[186] A. Bleuzen, F. Foglia, E. Furet, L. Helm, A.E. Merbach, J. Weber, Second coordination shell water exchange rate and mechanism:experiments and modeling on hexaaquachromium (III), J. Am. Chem. Soc. 118 (1996) 12777–12787.
[187] C.S. Bonnet, P.H. Fries, S. Crouzy, P. Delangle, Outer-sphere investigation of MRI relaxation contrast agents. Example of a cyclodecapeptide gadolinium complex with second-sphere water, J. Phys. Chem. B 114 (2010) 8770–8781.
[188] E.J. Werner, A. Datta, C.J. Jocher, K.N. Raymond, High-relaxivity MRI contrast agents: where coordination Chemistry meets medical imaging, Angew. Chem. Int. Ed. 47 (2008) 8568–8580.
[189] Chapter 3 Relaxation, Coord. Chem. Rev. 150 (1996) 77–110.
[190] A. Millan, A. Urtizberea, N.J.O. Silva, F. Palacio, V.S. Amaral, E. Snoeck, et al., Surface effects in maghemite nanoparticles, J. Magn. Magn Mater. 312 (2007) L5–L9.
[191] Y. Liu, T. Cui, Y. Li, Y. Zhao, Y. Ye, W. Wu, et al., Effects of crystal size and sphere diameter on static magnetic and electromagnetic properties of monodisperse Fe_3O_4 microspheres, Mater. Chem. Phys. 173 (2016) 152–160.
[192] W. Baaziz, B.P. Pichon, S. Fleutot, Y. Liu, C. Lefevre, J.-M. Greneche, et al., Magnetic iron oxide nanoparticles: reproducible tuning of the size and nanosized-dependent composition, defects, and spin canting, J. Phys. Chem. C 118 (2014) 3795–3810.
[193] Z. Shen, T. Chen, X. Ma, W. Ren, Z. Zhou, G. Zhu, et al., Multifunctional theranostic nanoparticles based on exceedingly small magnetic iron oxide nanoparticles for T_1-weighted magnetic resonance imaging and chemotherapy, ACS Nano 11 (2017) 10992–11004.
[194] T. Hyeon, S.S. Lee, J. Park, Y. Chung, H.B. Na, Synthesis of highly crystalline and monodisperse maghemite nanocrystallites without a size-selection process, J. Am. Chem. Soc. 123 (2001) 12798–12801.
[195] R. Hao, R. Xing, Z. Xu, Y. Hou, S. Gao, S. Sun, Synthesis, functionalization, and biomedical applications of multifunctional magnetic nanoparticles, Adv. Mater. 22 (2010) 2729–2742.
[196] H. Wei, O.T. Bruns, M.G. Kaul, E.C. Hansen, M. Barch, A. Wiśniowska, et al., Exceedingly small iron oxide nanoparticles as positive MRI contrast agents, Proc. Natl. Acad. Sci. U. S. A. 114 (2017) 2325–2330.
[197] Jeon M, Halbert MV, Stephen ZR, Zhang M. Iron oxide nanoparticles as T_1 contrast agents for magnetic resonance imaging: fundamentals, challenges, applications, and prospectives. Adv. Mater..n/a:1906539.
[198] H. Lin, K. Liu, J. Gao, Surface engineering to boost the performance of nanoparticle-based T_1 contrast agents, Eur J Inorg Chem. 2019 (2019) 3801–3809.
[199] U.I. Tromsdorf, O.T. Bruns, S.C. Salmen, U. Beisiegel, H. Weller, A highly effective, nontoxic T1 MR contrast agent based on ultrasmall PEGylated iron oxide nanoparticles, Nano Lett. 9 (2009) 4434–4440.
[200] S. Zhao, X. Yu, Y. Qian, W. Chen, J. Shen, Multifunctional magnetic iron oxide nanoparticles: an advanced platform for cancer theranostics, Theranostics 10 (2020) 6278–6309.
[201] T. Macher, J. Totenhagen, J. Sherwood, Y. Qin, D. Gurler, M.S. Bolding, et al., Ultrathin iron oxide nanowhiskers as positive contrast agents for magnetic resonance imaging, Adv. Funct. Mater. 25 (2015) 490–494.
[202] M. Wu, Q. Meng, Y. Chen, P. Xu, S. Zhang, Y. Li, et al., Ultrasmall confined iron oxide nanoparticle MSNs as a pH-responsive theranostic platform, Adv. Funct. Mater. 24 (2014) 4273–4283.
[203] M. Zhang, Y. Cao, L. Wang, Y. Ma, X. Tu, Z. Zhang, Manganese doped iron oxide theranostic nanoparticles for combined T_1 magnetic resonance imaging and photothermal therapy, ACS Appl. Mater. Interfaces 7 (2015) 4650–4658.
[204] A.G. Akopdzhanov, N.L. Shimanovskii, A.I. Borisova, V.A. Parshin, G.A. Frolov, Magnetic ferrite nanoparticles as a possible platform for magnetic-resonance contrast agents, Pharm. Chem. J. 53 (2020) 1164–1167.
[205] Z. Shen, J. Song, Z. Zhou, B.C. Yung, M.A. Aronova, Y. Li, et al., Dotted core–shell nanoparticles for T_1-weighted MRI of tumors, Adv. Mater. 30 (2018) 1803163.
[206] Y. Si, G. Zhang, D. Wang, C. Zhang, C. Yang, G. Bai, et al., Nanostructure-enhanced water interaction to increase the dual-mode MR contrast performance of gadolinium-doped iron oxide nanoclusters, Chem. Eng. J. 360 (2019) 289–298.
[207] M. Yu, Y. Niu, D. Zhou, R. Jiang, L. Zhang, H. Ju, et al., Hyaluronic acid-functionalized gadolinium doped iron oxide nanoparticles for atherosclerosis-targeted mr imaging, J. Biomed. Nanotechnol. 15 (2019) 127–137.
[208] R. Wei, Y. Xu, M. Xue, Hollow iron oxide nanomaterials: synthesis, functionalization, and biomedical applications, J. Mater. Chem. B 9 (2021) 1965–1979.
[209] W. Liu, G. Deng, D. Wang, M. Chen, Z. Zhou, H. Yang, et al., Renal-clearable zwitterionic conjugated hollow ultrasmall Fe_3O_4 nanoparticles for T_1-weighted MR imaging in vivo, J. Mater. Chem. B 8 (2020) 3087–3091.
[210] R. Wei, Z. Cai, B.W. Ren, A. Li, H. Lin, K. Zhang, et al., Biodegradable and renal-clearable hollow porous iron oxide nanoboxes for in vivo imaging, Chem. Mater. 30 (2018) 7950–7961.
[211] R. Xing, A.A. Bhirde, S. Wang, X. Sun, G. Liu, Y. Hou, et al., Hollow iron oxide nanoparticles as multidrug resistant Drug delivery and imaging vehicles, Nano Res 6 (2013) 1–9.
[212] V.K. Sharma, A. Alipour, Z. Soran-Erdem, Z.G. Aykut, H.V. Demir, Highly monodisperse low-magnetization magnetite nanocubes as simultaneous T_1–T_2 MRI contrast agents, Nanoscale 7 (2015) 10519–10526.
[213] L. Yang, Z. Zhou, H. Liu, C. Wu, H. Zhang, G. Huang, et al., Europium-engineered iron oxide nanocubes with high T_1 and T_2 contrast abilities for MRI in living subjects, Nanoscale 7 (2015) 6843–6850.
[214] I. Bertini, F. Capozzi, C. Luchinat, Z. Xia, Nuclear and electron relaxation of hexaaquairon(3+), J. Phys. Chem. 97 (1993) 1134–1137.
[215] G.N. La Mar, F.A. Walker, Proton nuclear magnetic resonance and electron spin resonance investigation of the electronic structure and magnetic properties of synthetic low-spin ferric porphyrins, J. Am. Chem. Soc. 95 (1973) 1782–1790.
[216] Y. Ducommun, K.E. Newman, A.E. Merbach, High-pressure oxygen-17 NMR evidence for A gradual mechanistic changeover from Ia to Id for water exchange on divalent octahedral metal ions going from manganese(II) to nickel(II), Inorg. Chem. 19 (1980) 3696–3703.
[217] A. Skjold, B.H. Amundsen, R. Wiseth, A. Støylen, O. Haraldseth, H.B.W. Larsson, et al., Manganese dipyridoxyl-diphosphate (MnDPDP) as a viability marker in patients with myocardial infarction, J. Magn. Reson. Imag. 26 (2007) 720–727.
[218] J.P. Hunt, M. Grant, H.W. Dodgen, Water exchange between solvent and aquomanganese(II) and aquophenanthrolinemanganese(II) complexes, Inorg. Chem. 10 (1971) 71–73.

[219] N.D. Thorat, R.A. Bohara, S.A.M. Tofail, Z.A. Alothman, M.J.A. Shiddiky, M.S. A Hossain, et al., Superparamagnetic gadolinium ferrite nanoparticles with controllable curie temperature – cancer theranostics for MR-imaging-guided magneto-chemotherapy, Eur J Inorg Chem. 2016 (2016) 4586–4597.

[220] Z. Zhou, L. Wang, X. Chi, J. Bao, L. Yang, W. Zhao, et al., Engineered iron-oxide-based nanoparticles as enhanced T_1 contrast agents for efficient tumor imaging, ACS Nano 7 (2013) 3287–3296.

[221] Z. Zhou, C. Wu, H. Liu, X. Zhu, Z. Zhao, L. Wang, et al., Surface and interfacial engineering of iron oxide nanoplates for highly efficient magnetic resonance angiography, ACS Nano 9 (2015) 3012–3022.

[222] I. Fernández-Barahona, L. Gutiérrez, S. Veintemillas-Verdaguer, J. Pellico, MdP. Morales, M. Catala, et al., Cu-doped extremely small iron oxide nanoparticles with large longitudinal relaxivity: one-pot synthesis and in vivo targeted molecular imaging, ACS Omega 4 (2019) 2719–2727.

[223] O. Perlman, I.S. Weitz, H. Azhari, Copper oxide nanoparticles as contrast agents for MRI and ultrasound dual-modality imaging, Phys. Med. Biol. 60 (2015) 5767–5783.

[224] M. Zhou, M. Tian, C. Li, Copper-based nanomaterials for cancer imaging and therapy, Bioconjugate Chem. 27 (2016) 1188–1199.

[225] J. Mou, C. Liu, P. Li, Y. Chen, H. Xu, C. Wei, et al., A facile synthesis of versatile $Cu_{2-x}S$ nanoprobe for enhanced MRI and infrared thermal/photoacoustic multimodal imaging, Biomaterials 57 (2015) 12–21.

[226] O. Perlman, A. Borodetsky, Y. Kauffmann, Y. Shamay, H. Azhari, I.S. Weitz, Gold/Copper@Polydopamine nanocomposite for contrast-enhanced dual modal computed tomography–magnetic resonance imaging, ACS Appl Nano Mater 2 (2019) 6124–6134.

[227] J. Sherwood, M. Rich, K. Lovas, J. Warram, M.S. Bolding, Y. Bao, T_1-Enhanced MRI-visible nanoclusters for imaging-guided Drug delivery, Nanoscale 9 (2017) 11785–11792.

[228] J.C. Park, G.T. Lee, H.-K. Kim, B. Sung, Y. Lee, M. Kim, et al., Surface design of Eu-doped iron oxide nanoparticles for tuning the magnetic relaxivity, ACS Appl. Mater. Interfaces 10 (2018) 25080–25089.

[229] B. Das, B. Choudhury, A. Gomathi, A.K. Manna, S.K. Pati, C.N.R. Rao, Interaction of inorganic nanoparticles with graphene, ChemPhysChem 12 (2011) 937–943.

[230] I.S. Lyubutin, A.O. Baskakov, S.S. Starchikov, K.-Y. Shih, C.-R. Lin, Y.-T. Tseng, et al., Synthesis and characterization of graphene modified by iron oxide nanoparticles, Mater. Chem. Phys. 219 (2018) 411–420.

[231] X. Xu, H. Li, Q. Zhang, H. Hu, Z. Zhao, J. Li, et al., Self-sensing, ultralight, and conductive 3D graphene/iron oxide aerogel elastomer deformable in a magnetic field, ACS Nano 9 (2015) 3969–3977.

[232] Y. Luo, Y. Tang, T. Liu, Q. Chen, X. Zhou, N. Wang, et al., Engineering graphene oxide with ultrasmall SPIONs and smart Drug release for cancer theranostics, Chem. Commun. 55 (2019) 1963–1966.

[233] J. Li, X. Li, S. Gong, C. Zhang, C. Qian, H. Qiao, et al., Dual-mode avocado-like all-iron nanoplatform for enhanced T_1/T_2 MRI-guided cancer theranostic therapy, Nano Lett. 20 (2020) 4842–4849.

[234] C. Lu, P. Dong, L. Pi, Z. Wang, H. Yuan, H. Liang, et al., Hydroxyl–PEG–phosphonic acid-stabilized superparamagnetic manganese oxide-doped iron oxide nanoparticles with synergistic effects for dual-mode MR imaging, Langmuir 35 (2019) 9474–9482.

[235] F. Hu, Q. Jia, Y. Li, M. Gao, Facile synthesis of ultrasmall PEGylated iron oxide nanoparticles for dual-contrast T_1- andT_2-weighted magnetic resonance imaging, Nanotechnology 22 (2011) 245604.

[236] K. Cheng, M. Yang, R. Zhang, C. Qin, X. Su, Z. Cheng, Hybrid nanotrimers for dual T_1 and T_2-weighted magnetic resonance imaging, ACS Nano 8 (2014) 9884–9896.

[237] Y.-K. Peng, C.N.P. Lui, Y.-W. Chen, S.-W. Chou, E. Raine, P.-T. Chou, et al., Engineering of single magnetic particle carrier for living brain cell imaging: a tunable T_1-/T_2-/dual-modal contrast agent for magnetic resonance imaging application, Chem. Mater. 29 (2017) 4411–4417.

[238] Z. Wang, J. Liu, T. Li, J. Liu, B. Wang, Controlled synthesis of $MnFe_2O_4$ nanoparticles and Gd complex-based nanocomposites as tunable and enhanced T_1/T_2-weighted MRI contrast agents, J. Mater. Chem. B 2 (2014) 4748–4753.

[239] L. Feng, D. Yang, F. He, S. Gai, C. Li, Y. Dai, et al., A core–shell-satellite structured Fe_3O_4@g-C_3N_4–UCNPs–PEG for T_1/T_2-weighted dual-modal MRI-guided photodynamic therapy, Adv Healthc Mater 6 (2017) 1700502.

[240] S.L.C. Pinho, J. Sereno, A.J. Abrunhosa, M.-H. Delville, J. Rocha, L.D. Carlos, et al., Gd- and Eu-loaded iron Oxide@Silica core–shell nanocomposites as trimodal contrast agents for magnetic resonance imaging and optical imaging, Inorg. Chem. 58 (2019) 16618–16628.

[241] S. Biju, J. Gallo, M. Bañobre-López, B.B. Manshian, S.J. Soenen, U. Himmelreich, et al., A magnetic chameleon: biocompatible lanthanide fluoride nanoparticles with magnetic field dependent tunable contrast properties as a versatile contrast agent for low to ultrahigh field MRI and optical imaging in biological window, Chem. Eur J. 24 (2018) 7388–7397.

[242] G.H. Im, S.M. Kim, D.-G. Lee, W.J. Lee, J.H. Lee, I.S. Lee, Fe_3O_4/MnO hybrid nanocrystals as a dual contrast agent for both T_1- and T_2-weighted liver MRI, Biomaterials 34 (2013) 2069–2076.

[243] X. Sun, R. Du, L. Zhang, G. Zhang, X. Zheng, J. Qian, et al., A pH-responsive yolk-like nanoplatform for tumor targeted dual-mode magnetic resonance imaging and chemotherapy, ACS Nano 11 (2017) 7049–7059.

[244] M. Yang, L. Gao, K. Liu, C. Luo, Y. Wang, L. Yu, et al., Characterization of Fe_3O_4/SiO_2/$Gd_2O(CO_3)_2$ core/shell/shell nanoparticles as T_1 and T_2 dual mode MRI contrast agent, Talanta 131 (2015) 661–665.

[245] J-s Choi, J.-H. Lee, T.-H. Shin, H.-T. Song, E.Y. Kim, J. Cheon, Self-confirming "AND" logic nanoparticles for fault-free MRI, J. Am. Chem. Soc. 132 (2010) 11015–11017.

[246] Z. Zhou, D. Huang, J. Bao, Q. Chen, G. Liu, Z. Chen, et al., A synergistically enhanced T_1–T_2 dual-modal contrast agent, Adv. Mater. 24 (2012) 6223–6228.

[247] S.Y.X. Xiao, L. Zhang, Y. Zhang, W. Fan, T. Sun, C. Zhou, Y. Liu, Y. Liu, M. Gong, D. Zhang, Synthesis of PEG-coated, ultrasmall, manganese-doped iron oxide nanoparticles with high relaxivity for T_1/T_2 dual-contrast magnetic resonance imaging, Int. J. Nanomed. 14 (2019) 8499–8507.

[248] J. Shen, Y. Li, Y. Zhu, X. Yang, X. Yao, J. Li, et al., Multifunctional gadolinium-labeled silica-coated Fe_3O_4 and $CuInS_2$ nanoparticles as a platform for in vivo tri-modality magnetic resonance and fluorescence imaging, J. Mater. Chem. B 3 (2015) 2873–2882.

[249] X. Zhu, J. Zhou, M. Chen, M. Shi, W. Feng, F. Li, Core–shell Fe_3O_4@$NaLuF_4$:Yb, Er/Tm nanostructure for MRI, CT and upconversion luminescence tri-modality imaging, Biomaterials 33 (2012) 4618–4627.

[250] M. Nafiujjaman, V. Revuri, M. Nurunnabi, K. Jae Cho, Y-k Lee, Photosensitizer conjugated iron oxide nanoparticles for simultaneous in vitro magneto-fluorescent imaging guided photodynamic therapy, Chem. Commun. 51 (2015) 5687–5690.

[251] J. Gao, W. Zhang, P. Huang, B. Zhang, X. Zhang, B. Xu, Intracellular spatial control of fluorescent magnetic nanoparticles, J. Am. Chem. Soc. 130 (2008) 3710–3711.

[252] A.A. Bogdanov, A.J. Dixon, S. Gupta, L. Zhang, S. Zheng, M.S. Shazeeb, et al., Synthesis and testing of modular dual-modality nanoparticles for magnetic resonance and multispectral photoacoustic imaging, Bioconjugate Chem. 27 (2016) 383–390.

[253] N. Kang, D. Xu, Y. Han, X. Lv, Z. Chen, T. Zhou, et al., Magnetic targeting core/shell Fe_3O_4/Au nanoparticles for magnetic resonance/photoacoustic dual-modal imaging, Mater. Sci. Eng. C 98 (2019) 545–549.

[254] N. Kostevsek, E. Locatelli, C. Garrovo, F. Arena, I. Monaco, I.P. Nikolov, et al., The one-step synthesis and surface functionalization of dumbbell-like gold–iron oxide nanoparticles: a chitosan-based nanotheranostic system, Chem. Commun. 52 (2016) 378–381.

[255] D. Hu, C. Liu, L. Song, H. Cui, G. Gao, P. Liu, et al., Indocyanine green–loaded polydopamine–iron ions coordination nanoparticles for photoacoustic/magnetic resonance dual-modal imaging-guided cancer photothermal therapy, Nanoscale 8 (2016) 17150–17158.

[256] R. Madru, P. Kjellman, F. Olsson, K. Wingårdh, C. Ingvar, F. Ståhlberg, et al., ^{99m}Tc-Labeled superparamagnetic iron oxide nanoparticles for multimodality SPECT/MRI of sentinel lymph nodes, J. Nucl. Med. 53 (2012) 459–463.

[257] J.T.-W. Wang, L. Cabana, M. Bourgognon, H. Kafa, A. Protti, K. Venner, et al., Magnetically decorated multiwalled carbon nanotubes as dual MRI and SPECT contrast agents, Adv. Funct. Mater. 24 (2014) 1880–1894.

[258] P. Wang, Y. Shi, S. Zhang, X. Huang, J. Zhang, Y. Zhang, et al., Hydrogen peroxide responsive iron–based nanoplatform for multimodal imaging–guided cancer therapy, Small 15 (2019) 1803791.

[259] J-s Choi, J.C. Park, H. Nah, S. Woo, J. Oh, K.M. Kim, et al., A hybrid nanoparticle probe for dual-modality positron emission tomography and magnetic resonance imaging, Angew. Chem. Int. Ed. 47 (2008) 6259–6262.

[260] Y. Peng, X. Wang, Y. Wang, Y. Gao, R. Guo, X. Shi, et al., Macrophage-laden gold nanoflowers embedded with ultrasmall iron oxide nanoparticles for enhanced dual-mode CT/MR imaging of tumors, Pharmaceutics 13 (2021) 995.

[261] H. Cai, K. Li, J. Li, S. Wen, Q. Chen, M. Shen, et al., Dendrimer-assisted formation of Fe_3O_4/Au nanocomposite particles for targeted dual mode CT/MR imaging of tumors, Small 11 (2015) 4584–4593.

[262] A. Sood, V. Arora, J. Shah, R.K. Kotnala, T.K. Jain, Multifunctional gold coated iron oxide core-shell nanoparticles stabilized using thiolated sodium alginate for biomedical applications, Mater. Sci. Eng. C 80 (2017) 274–281.

[263] S. Veintemillas-Verdaguer, Y. Luengo, C.J. Serna, M. Andrés-Vergés, M. Varela, M. Calero, et al., Bismuth labeling for the CT assessment of local administration of magnetic nanoparticles, Nanotechnology 26 (2015) 135101.

[264] H.Y. Zhao, S. Liu, J. He, C.C. Pan, H. Li, Z.Y. Zhou, et al., Synthesis and application of strawberry-like Fe_3O_4-Au nanoparticles as CT-MR dual-modality contrast agents in accurate detection of the progressive liver disease, Biomaterials 51 (2015) 194–207.

[265] N. Lee, H.R. Cho, M.H. Oh, S.H. Lee, K. Kim, B.H. Kim, et al., Multifunctional Fe_3O_4/TaO_x core/shell nanoparticles for simultaneous magnetic resonance imaging and X-ray computed tomography, J. Am. Chem. Soc. 134 (2012) 10309–10312.

[266] M. Ma, H. Zhu, J. Ling, S. Gong, Y. Zhang, Y. Xia, et al., Quasi-amorphous and hierarchical Fe2O3 supraparticles: active T_1-weighted magnetic resonance imaging in vivo and renal clearance, ACS Nano 14 (2020) 4036–4044.

[267] X. Xu, X. Zhou, B. Xiao, H. Xu, D. Hu, Y. Qian, et al., Glutathione-responsive magnetic nanoparticles for highly sensitive diagnosis of liver metastases, Nano Lett. 21 (2021) 2199–2206.

[268] Y. Liu, Z. Yang, X. Huang, G. Yu, S. Wang, Z. Zhou, et al., Glutathione-responsive self-assembled magnetic gold nanowreath for enhanced tumor imaging and imaging-guided photothermal therapy, ACS Nano 12 (2018) 8129–8137.

[269] S. Fu, Z. Cai, H. Ai, Stimulus-responsive nanoparticle magnetic resonance imaging contrast agents: design considerations and applications, Adv Healthc Mater 10 (2021) 2001091.

[270] D. Ling, W. Park, S-j Park, Y. Lu, K.S. Kim, M.J. Hackett, et al., Multifunctional tumor pH-sensitive self-assembled nanoparticles for bimodal imaging and treatment of resistant heterogeneous tumors, J. Am. Chem. Soc. 136 (2014) 5647–5655.

[271] H. Zhou, M. Guo, J. Li, F. Qin, Y. Wang, T. Liu, et al., Hypoxia-triggered self-assembly of ultrasmall iron oxide nanoparticles to amplify the imaging signal of a tumor, J. Am. Chem. Soc. 143 (2021) 1846–1853.

[272] S. Okada, B.B. Bartelle, N. Li, V. Breton-Provencher, J.J. Lee, E. Rodriguez, et al., Calcium-dependent molecular fMRI using a magnetic nanosensor, Nat. Nanotechnol. 13 (2018) 473–477.

[273] J. Gallo, N. Kamaly, I. Lavdas, E. Stevens, Q.-D. Nguyen, M. Wylezinska-Arridge, et al., CXCR4-Targeted and MMP-responsive iron oxide nanoparticles for enhanced magnetic resonance imaging, Angew. Chem. Int. Ed. 53 (2014) 9550–9554.

[274] Zhang P, Zeng J, Li Y, Yang C, Meng J, Hou Y, et al. Quantitative mapping of glutathione within intracranial tumors through interlocked MRI signals of a responsive nanoprobe. Angew Chem-Int Edit.n/a.

[275] S. Santra, S.D. Jativa, C. Kaittanis, G. Normand, J. Grimm, J.M. Perez, Gadolinium-encapsulating iron oxide nanoprobe as activatable NMR/MRI contrast agent, ACS Nano 6 (2012) 7281–7294.

[276] X. Zhu, H. Lin, L. Wang, X. Tang, L. Ma, Z. Chen, et al., Activatable T_1 relaxivity recovery nanoconjugates for kinetic and sensitive analysis of matrix metalloprotease 2, ACS Appl. Mater. Interfaces 9 (2017) 21688–21696.

[277] M.-H. Kim, H.-Y. Son, G.-Y. Kim, K. Park, Y.-M. Huh, S. Haam, Redoxable heteronanocrystals functioning magnetic relaxation switch for activatable T_1 and T_2 dual-mode magnetic resonance imaging, Biomaterials 101 (2016) 121–130.

[278] J. Lu, J. Sun, F. Li, J. Wang, J. Liu, D. Kim, et al., Highly sensitive diagnosis of small hepatocellular carcinoma using pH-responsive iron oxide nanocluster Assemblies, J. Am. Chem. Soc. 140 (2018) 10071–10074.

[279] X. Li, S. Lu, Z. Xiong, Y. Hu, D. Ma, W. Lou, et al., Light-addressable nanoclusters of ultrasmall iron oxide nanoparticles for enhanced and dynamic magnetic resonance imaging of arthritis, Adv. Sci. 6 (2019) 1901800.

[280] M. Muthiah, I.-K. Park, C.-S. Cho, Surface modification of iron oxide nanoparticles by biocompatible polymers for tissue imaging and targeting, Biotechnol. Adv. 31 (2013) 1224–1236.

[281] K.M. Kamruzzaman Selim, Y.-S. Ha, S.-J. Kim, Y. Chang, T.-J. Kim, G. Ho Lee, et al., Surface modification of magnetite nanoparticles using lactobionic acid and their interaction with hepatocytes, Biomaterials 28 (2007) 710–716.

[282] Q. Quan, J. Xie, H. Gao, M. Yang, F. Zhang, G. Liu, et al., HSA coated iron oxide nanoparticles as Drug delivery vehicles for cancer therapy, Mol. Pharm. 8 (2011) 1669–1676.

[283] M.A. Abakumov, N.V. Nukolova, M. Sokolsky-Papkov, S.A. Shein, T.O. Sandalova, H.M. Vishwasrao, et al., VEGF-targeted magnetic nanoparticles for MRI visualization of brain tumor, Nanomed. Nanotechnol. Biol. Med. 11 (2015) 825–833.

[284] X. Duan, Y. Li, Physicochemical characteristics of nanoparticles affect circulation, biodistribution, cellular internalization, and trafficking, Small 9 (2013) 1521–1532.

[285] Y. Wang, Y.W. Ng, Y. Chen, B. Shuter, J. Yi, J. Ding, et al., Formulation of superparamagnetic iron oxides by nanoparticles of biodegradable polymers for magnetic resonance imaging, Adv. Funct. Mater. 18 (2008) 308–318.

[286] j Xj Liu, j Zhou, Y. Zhang, D.J. Guo, Z.G. Wang, Fe_3O_4-based PLGA nanoparticles as MR contrast agents for the detection of thrombosis, Int. J. Nanomed. 12 (2017) 1113–1126.

[287] J. Huang, L. Bu, J. Xie, K. Chen, Z. Cheng, X. Li, et al., Effects of nanoparticle size on cellular uptake and liver MRI with polyvinylpyrrolidone-coated iron oxide nanoparticles, ACS Nano 4 (2010) 7151–7160.

[288] H.-M. Yang, C.W. Park, M.-A. Woo, M.I. Kim, Y.M. Jo, H.G. Park, et al., HER2/neu antibody conjugated poly(amino acid)-coated iron oxide nanoparticles for breast cancer MR imaging, Biomacromolecules 11 (2010) 2866–2872.

[289] Y. Xu, D.C. Baiu, J.A. Sherwood, M.R. McElreath, Y. Qin, K.H. Lackey, et al., Linker-free conjugation and specific cell targeting of antibody functionalized iron-oxide nanoparticles, J. Mater. Chem. B 2 (2014) 6198–6206.

[290] J.-H. Park, G. von Maltzahn, L. Zhang, M.P. Schwartz, E. Ruoslahti, S.N. Bhatia, et al., Magnetic iron oxide nanoworms for tumor targeting and imaging, Adv. Mater. 20 (2008) 1630–1635.

[291] A.K. Hauser, M.I. Mitov, E.F. Daley, R.C. McGarry, K.W. Anderson, J.Z. Hilt, Targeted iron oxide nanoparticles for the enhancement of radiation therapy, Biomaterials 105 (2016) 127–135.

[292] K. Min, H. Jo, K. Song, M. Cho, Y.-S. Chun, S. Jon, et al., Dual-aptamer-based delivery vehicle of doxorubicin to both PSMA (+) and PSMA (−) prostate cancers, Biomaterials 32 (2011) 2124–2132.

[293] C. Li, T. Chen, I. Ocsoy, G. Zhu, E. Yasun, M. You, et al., Gold-coated Fe3O4 nanoroses with five unique functions for cancer cell targeting, imaging, and therapy, Adv. Funct. Mater. 24 (2014) 1772–1780.

[294] Y. Zhang, N. Kohler, M. Zhang, Surface modification of superparamagnetic magnetite nanoparticles and their intracellular uptake, Biomaterials 23 (2002) 1553–1561.

[295] K.J. Landmark, S. DiMaggio, J. Ward, C. Kelly, S. Vogt, S. Hong, et al., Synthesis, characterization, and in vitro testing of superparamagnetic iron oxide nanoparticles targeted using folic acid-conjugated dendrimers, ACS Nano 2 (2008) 773–783.

[296] A. Kumar, B. Sahoo, A. Montpetit, S. Behera, R.F. Lockey, S.S. Mohapatra, Development of hyaluronic acid–Fe_2O_3 hybrid magnetic nanoparticles for targeted delivery of peptides, Nanomed. Nanotechnol. Biol. Med. 3 (2007) 132–137.

[297] T. Gong, Z. Dong, Y. Fu, T. Gong, L. Deng, Z. Zhang, Hyaluronic acid modified doxorubicin loaded Fe_3O_4 nanoparticles effectively inhibit breast cancer metastasis, J. Mater. Chem. B 7 (2019) 5861–5872.

[298] Z. Jia, L. Song, F. Zang, J. Song, W. Zhang, C. Yan, et al., Active-target T_1-weighted MR imaging of tiny hepatic tumor via RGD modified ultra-small Fe_3O_4 nanoprobes, Theranostics 6 (2016) 1780–1791.

[299] O. Veiseh, J.W. Gunn, M. Zhang, Design and fabrication of magnetic nanoparticles for targeted Drug delivery and imaging, Adv. Drug Deliv. Rev. 62 (2010) 284–304.

[300] H. Wei, N. Insin, J. Lee, H.-S. Han, J.M. Cordero, W. Liu, et al., Compact zwitterion-coated iron oxide nanoparticles for biological applications, Nano Lett. 12 (2012) 22–25.

[301] S. Chen, L. Rong, Q. Lei, P.-X. Cao, S.-Y. Qin, D.-W. Zheng, et al., A surface charge-switchable and folate modified system for Co-delivery of proapoptosis peptide and p53 plasmid in cancer therapy, Biomaterials 77 (2016) 149–163.

[302] Z.G. Estephan, P.S. Schlenoff, J.B. Schlenoff, Zwitteration as an alternative to PEGylation, Langmuir 27 (2011) 6794–6800.

[303] Z. Cao, Q. Yu, H. Xue, G. Cheng, S. Jiang, Nanoparticles for Drug delivery prepared from amphiphilic PLGA zwitterionic block copolymers with sharp contrast in polarity between two blocks, Angew. Chem. Int. Ed. 49 (2010) 3771–3776.

[304] B.B. Karakoçak, R. Raliya, J.T. Davis, S. Chavalmane, W.-N. Wang, N. Ravi, et al., Biocompatibility of gold nanoparticles in retinal pigment epithelial cell line, Toxicol. Vitro 37 (2016) 61–69.

[305] A. Ángeles-Pascual, J.R. Piñón-Hernández, M. Estevez-González, U. Pal, S. Velumani, R. Pérez, et al., Structure, magnetic and cytotoxic behaviour of solvothermally grown Fe_3O_4@Au core-shell nanoparticles, Mater. Char. 142 (2018) 237–244.

[306] D.-L. Xia, Y.-P. Chen, C. Chen, Y.-F. Wang, X-d Li, H. He, et al., Comparative study of biosafety, DNA, and chromosome damage of different-materials-modified Fe_3O_4 in rats, Appl. Biochem. Biotechnol. 177 (2015) 1069–1082.

[307] U. Kostiv, V. Patsula, M. Šlouf, I.M. Pongrac, S. Škokić, M.D. Radmilović, et al., Physico-chemical characteristics, biocompatibility, and MRI applicability of novel monodisperse PEG-modified magnetic Fe_3O_4&SiO_2 core–shell nanoparticles, RSC Adv. 7 (2017) 8786–8797.

[308] W. Injumpa, P. Ritprajak, N. Insin, Size-dependent cytotoxicity and inflammatory responses of PEGylated silica-iron oxide nanocomposite size series, J. Magn. Magn Mater. 427 (2017) 60–66.

[309] M. Ledda, D. Fioretti, M.G. Lolli, M. Papi, C. Di Gioia, R. Carletti, et al., Biocompatibility assessment of sub-5 nm silica-coated superparamagnetic iron oxide nanoparticles in human stem cells and in mice for potential application in nanomedicine, Nanoscale 12 (2020) 1759–1778.

[310] K. Müller, J.N. Skepper, T.Y. Tang, M.J. Graves, A.J. Patterson, C. Corot, et al., Atorvastatin and uptake of ultrasmall superparamagnetic iron oxide nanoparticles (Ferumoxtran-10) in human monocyte–macrophages: implications for magnetic resonance imaging, Biomaterials 29 (2008) 2656–2662.

[311] A. Atrei, C. Innocenti, S. Lamponi, S. Paesano, G. Leone, A. Reale, et al., Covalent hyaluronic-based coating of magnetite nanoparticles: preparation, physicochemical and biological characterization, Mater Sci Eng C-Mater Biol Appl. 107 (2020) 110271.

[312] S.-M. Yu, L. Gonzalez-Moragas, M. Milla, A. Kolovou, R. Santarella-Mellwig, Y. Schwab, et al., Bio-identity and fate of albumin-coated SPIONs evaluated in cells and by the C. elegans model, Acta Biomater. 43 (2016) 348–357.

[313] M. Aliakbari, E. Mohammadian, A. Esmaeili, Z. Pahlevanneshan, Differential effect of polyvinylpyrrolidone-coated superparamagnetic iron oxide nanoparticles on BT-474 human breast cancer cell viability, Toxicol. Vitro 54 (2019) 114–122.